

学位論文

Numerical Study of Solar Prominence
Formation

(太陽プロミネンス形成の数値的研究)

平成 28 年 12 月 博士 (理学) 申請

東京大学大学院理学系研究科

地球惑星科学専攻

金子 岳史

Doctor Thesis

**Numerical Study of Solar
Prominence Formation**

Takafumi Kaneko

Department of Earth and Planetary Science
Graduate School of Science, The University of Tokyo

Contents

1	General Introduction	1
1.1	Solar prominence	1
1.2	The solar corona	2
1.3	Magnetic field of prominence	5
1.4	Differential emission measure of prominence	8
1.5	Prominence formation: Observations	10
1.5.1	Reconnection at PIL	10
1.5.2	In-situ condensation	11
1.5.3	Levitation by emerging flux	13
1.5.4	Injection by jet	16
1.6	Prominence formation: Theoretical approach	16
1.6.1	Thermal instability	16
1.6.2	Radiative condensation model	19
1.7	Interior dynamics of prominence	20
1.7.1	Fine structures	21
1.7.2	Vertical flows	21
1.7.3	Turbulence	22
1.8	Motivation	23

2	Reconnection-Condensation Model	25
2.1	Introduction	25
2.2	Basic idea of reconnection-condensation model	26
2.3	Two-dimensional simulations	26
2.3.1	Numerical Settings	27
2.3.2	Results	33
2.3.3	Effect of footpoint motion	41
2.3.4	Effect of heating model	47
2.4	Three-dimensional simulations	48
2.4.1	Introduction	48
2.4.2	Numerical Settings	51
2.4.3	Results	52
2.4.4	Critical condition	53
2.4.5	Comparison with observation	56
2.4.6	Discussion on three-dimensional simulations	63
2.5	Summary and Discussion	66
3	Modeling of Prominence Interior Dynamics	69
3.1	Introduction	69
3.2	Numerical settings	71
3.3	Results	72
3.4	Summary and Discussion	85
4	General Discussion	88
4.1	Summary of the results	88
4.2	Discussion	90

4.3	Future prospect	93
5	Concluding remarks	96
A	Numerical implementation for footpoint motion	98

Abstract

Solar prominences are cool dense plasma clouds in the hot tenuous corona. Since prominences suddenly erupt and evolve into coronal mass ejections, they have potential to give an impact on the plasma environment in the interplanetary space. The origin of cool dense plasma and mass maintenance mechanism of prominences are still unclear. In this thesis, we investigate the formation mechanism of a prominence by using magnetohydrodynamic simulations.

In Chapter 2, we propose a new prominence formation model, *reconnection-condensation model*, and demonstrate it by using multi-dimensional magnetohydrodynamic simulations including optically thin radiative cooling and nonlinear anisotropic thermal conduction. In our model, magnetic reconnection changes a topology of coronal magnetic fields, leading to the formation of a flux rope. The flux rope traps dense plasmas inside it. Radiative cooling inside the flux rope is enhanced by the trapped dense plasmas, leading to a cooling-dominant thermal nonequilibrium state. Once the length of magnetic field exceeds the Field length, the thermal nonequilibrium can not be compensated by thermal conduction, leading to radiative condensation for prominence formation. From the parameter survey on footpoint motions, we find that anti-shearing motion, which reduces magnetic shear of an coronal arcade field, causes radiative condensation, whereas shearing motion, which increases magnetic shear, causes eruption of a hot flux rope. The coronal heating model does not affect the triggering process of radiative condensation, whereas it can affect the

properties of prominence. Multi-wavelength EUV emissions synthesized from our three-dimensional simulation results reproduced observational temporal and spatial intensity shift from coronal temperatures to prominence temperatures.

In Chapter 3, we reproduce a dynamic interior of a prominence in a framework of our proposed model. As mass of prominence increases by radiative condensation, magnetic tension force can not sustain prominence mass, leading to the Rayleigh-Taylor instability. Downward speed of spikes are much smaller than free-fall speed, because upward magnetic tension cancels gravity as spikes extend. Spikes are reflected at the bottom boundary, and create upflows or vortex motions. By the interaction of downflows and reflected flows, the spikes are squeezed, resulting in the formation of thin vertical threads. We also found that the Rayleigh-Taylor instability enhances mass growth rate of radiative condensation. Our results suggest the presence of self mass maintenance mechanism of a prominence due to a coupling of radiative condensation and the Rayleigh-Taylor instability.

Through the studies in this thesis, we succeeded to propose a self-consistent model for a long-standing issue of solar prominence formation. Our model resolves several issues in the previous models: a previous theoretical model requires a strong steady footpoint heating and subsequent chromospheric evaporation to trigger radiative condensation, while such a footpoint heating and evaporated flows have not been detected in observations. In observations, it was found that magnetic reconnection at a polarity inversion lines (PIL) caused prominence formations, while the mechanism to trigger radiative condensation by reconnection was unclear. In addition to these, we revealed that a flux rope formation by reconnection drives radiative condensation when the length of reconnected loops exceeds the Field length. We found that anti-shearing motion is necessary to create cooling-dominant thermal imbalance in a flux rope. This suggests that relative position of supergranules along a PIL is an important factor for prominence formation. We also

found that radiative condensation rate is enhanced by coupling with the Rayleigh-Taylor instability and becomes comparable to the mass drainage rate of downflows. This result indicates the presence of self mass-maintenance mechanism of a prominence.

Acknowledgement

I would like to express my deepest gratitude to my supervisor, Takaaki Yokoyama, for his continuous guidance, great encouragement, and endless patience during my PhD work.

I would like to thank Rony Keppens, Marcel Goossense, Tom Van Doorselaere, Chun Xia and researchers in Centre for mathematical Plasma Astrophysics, KU Leuven, Belgium, for their help and insightful discussions during my stay.

Many thanks to my colleagues in Yokoyama lab, Yusuke Iida, Naomasa Kitagawa, Shin Toriumi, Hideyuki Hotta, Yuki Matsui, Haruhisa Iijima, Shuoyang Wang, Shunya Kono, Tetsuya Nasuda, Munehito Shoda, Chiaki Ichimura, Yoshiaki Oi, Yikang Wang, Yuto Bekki, and other members in the Solar-Terrestrial Physics Colloquium for the helpful discussions and making my years in graduate school more than academic. I would like to acknowledge the reserchers in ISAS/JAXA, NAOJ, Kyoto University, Nagoya University, and many other institutes for the valuable discussions.

I have been supported by JSPS, JHPCN, HPCI, and the Program for Leading Graduate Schools, FMSP, MEXT, in Japan. Numerical computations were carried out on Cray XC30 supercomputer at CfCA/NAOJ.

Finally, a special thanks is extended to my family for their long-standing support and encouragement.

Chapter 1

General Introduction

1.1 Solar prominence

Solar prominences are cool dense plasma clouds in the hot tenuous corona. They are observed as bright structures on the solar limb, locating inside an arch-like closed magnetic field called helmet streamer (Fig. 1.1). They suddenly erupt to the interplanetary space and evolve into bright cores of coronal mass ejections (CMEs, Gopalswamy et al., 2003). Not only the driving mechanism of eruptions but also the origin of cool dense plasmas of prominences is still unclear. Revealing the mechanisms of prominence formation and eruption is an important issue on solar physics, solar-terrestrial physics and space weather. In this thesis, we investigate the formation mechanism of prominence by using numerical simulations.

Typical temperature of prominences is lower than 10^4 K against million kelvin temperature of the corona, and typical density is $10^9 - 10^{11} \text{ cm}^{-3}$ which is 10 - 100 times larger than that of the surrounding corona (Labrosse et al., 2010). Prominences are bright structures on the limb (Fig. 1.2), whereas when observed on the disk, they are called as dark filaments because of dark filamentary morphology (Fig. 1.3). Prominences and fil-

aments are essentially the same objects. The quiescent prominences are long (order of 100 Mm), long lived (days to months) and locating as high as 100 Mm, while active region prominences are shorter (of order 10 Mm), short lived (minutes to hours) and locating at lower altitudes (< 10 Mm) (Mackay et al., 2010).

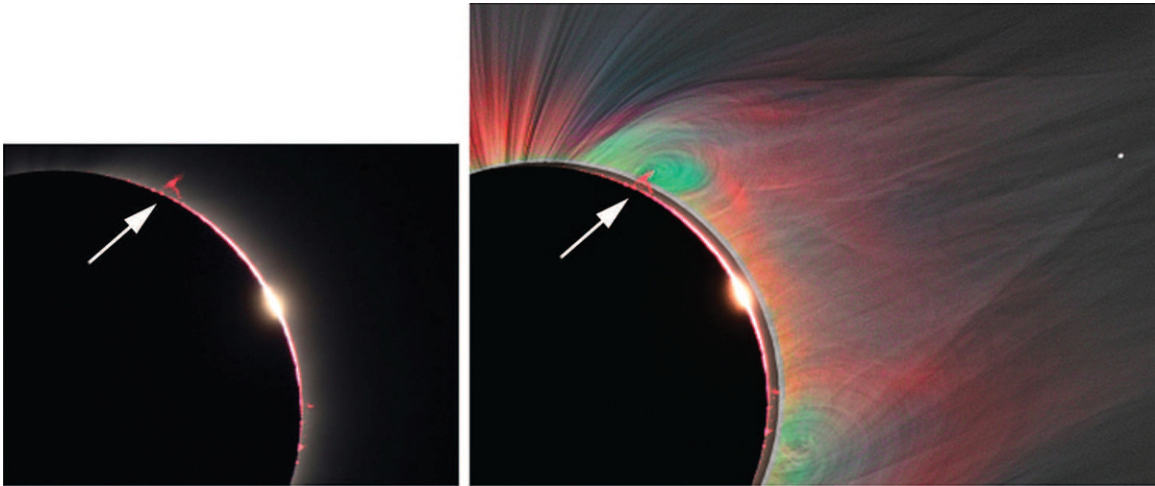


Figure 1.1: Prominence observed during a total solar eclipse of 2008 August 1. White arrows point the prominence. Left panel: H α image. Right panel: composition of H α (inner part) with white light (gray), Fe XI (red), and Fe XIV (green). Images extracted from Habbal et al. (2014).

1.2 The solar corona

The solar corona extends in the outermost region of the solar atmosphere, where the temperature exceeds 10^6 K. The corona is composed of magnetized plasmas, where various kinds of magnetically driven phenomena such as flares, prominence eruptions, and CMEs occur. These explosive phenomena eject huge amount of coronal plasmas and magnetic fields into interplanetary space, and sometimes give a strong impact on the plasma

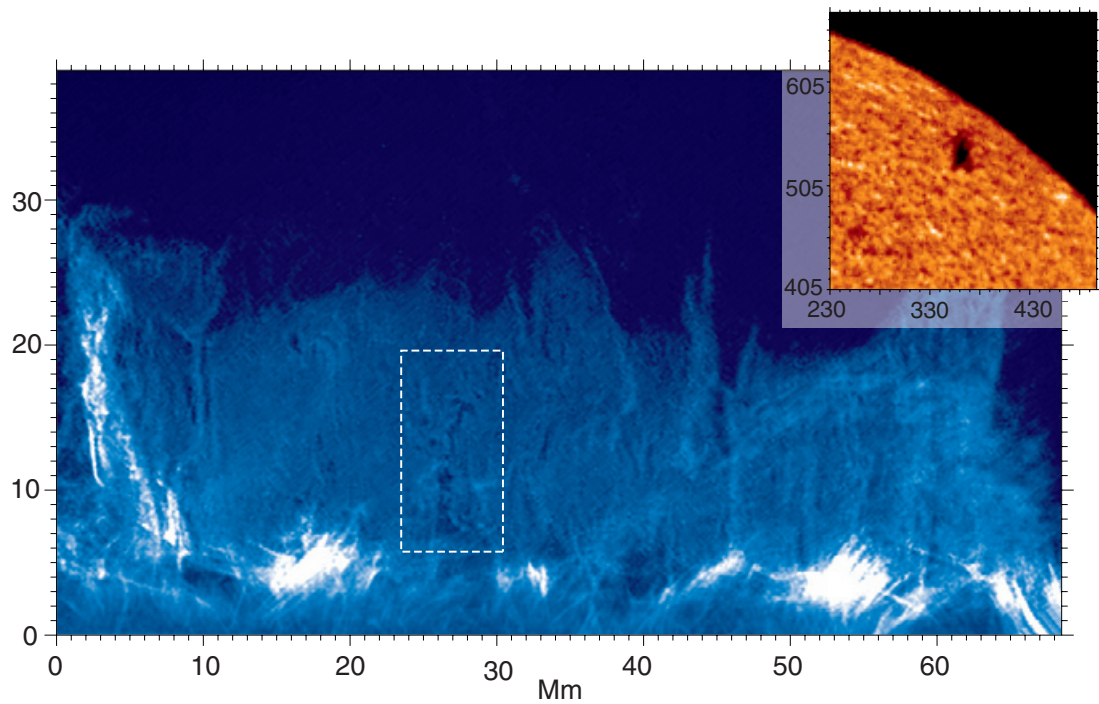


Figure 1.2: Solar prominence on solar limb on 2006 November 30 UT observed by Hinode/SOT Ca II h line. The inset shows the corresponding filament on 2006 November 27 imaged by the MLSO PICS instrument $H\alpha$ (images taken from Berger et al., 2010).

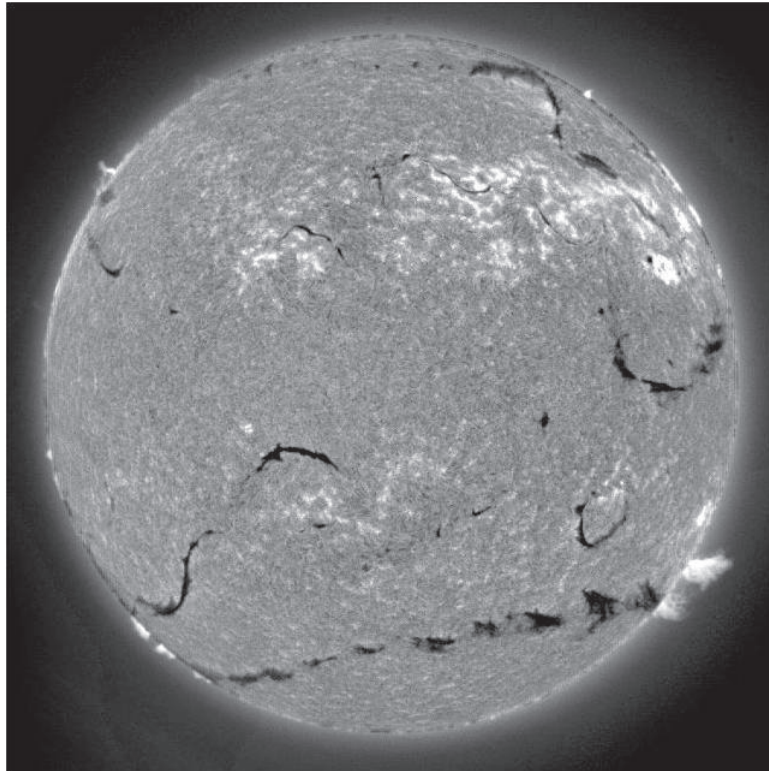


Figure 1.3: Contrast enhanced $H\alpha$ full disk image observed by 20 cm full disk telescope of *Big Bear Solar Observatory* on 30 January 1999.

environments around planets, e.g., a magnetic storm in the magnetosphere.

The coronal magnetic structures consist of open magnetic fields and closed magnetic loops. Coronal loops are one of the most fundamental structures in the solar atmosphere and ubiquitously observed by X-ray and extreme ultraviolet (EUV) wavelengths (Fig. 1.4). Magnetic loops contain 0.1 – 2 MK plasmas along themselves, and compose both quiet and active region corona. The coronal hole is mainly composed of open magnetic fields.

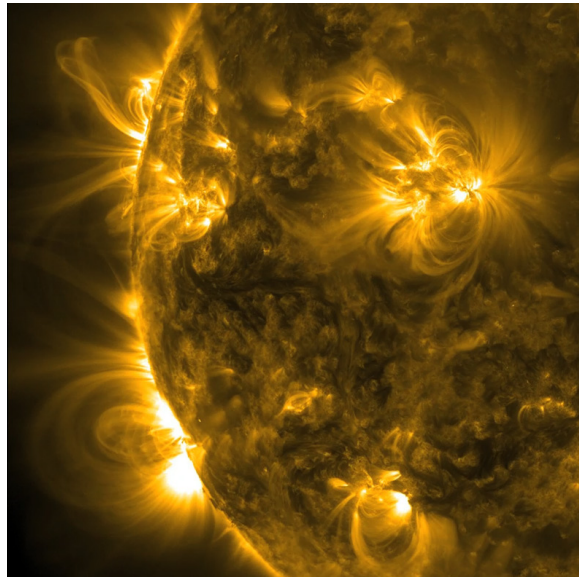


Figure 1.4: Coronal loops observed by SDO/AIA 171Å on 2012 October 14.

1.3 Magnetic field of prominence

Dense prominence materials are sustained by the coronal magnetic fields. The magnetic field strength measured by interpreting polarization signals by the Hanle effect in quiescent prominences is typically 3 – 15 G (Leroy et al., 1983, 1984; Bommier et al., 1994;

Casini et al., 2003; López Ariste & Aulanier, 2007; Schmieder et al., 2013; Orozco Suárez et al., 2014), while that in active region prominences is 30 – 700 G associated with a strong magnetic field of an active region (Paletou et al., 2001; Kuckein et al., 2009). Filaments, i.e., counterparts of prominences observed on the solar disk, always locate along polarity inversion lines (PILs) across which the magnetic polarity at the photosphere is reversed (Martin, 1998a; Mackay et al., 2008). Figure 1.5 shows two types of the classical two-dimensional models of the magnetic fields sustaining a prominence. Figure 1.5 (a) depicts the normal polarity model (Kippenhahn & Schlüter, 1957) in which the direction of magnetic field inside a prominence matches that of the overlying coronal magnetic field. The prominence is sustained at the concave-up dip area in the arcade field by upward magnetic tension force. Figure 1.5 (b) depicts the inverse polarity model (Kuperus & Raadu, 1974) in which the direction of magnetic field inside a prominence opposes to that of the overlying coronal magnetic field. The prominence is sustained at the dip in the lower half of a flux rope where magnetic tension force directs upward (e.g. Aulanier et al., 1998a). Figure. 1.6 shows possible three-dimensional magnetic fields. Normal polarity configuration corresponds to a sheared arcade field with a dip (panel (a)). Inverse polarity configuration corresponds to a helical flux rope (panel (b)).

Figure 1.7 shows an example of observation of photospheric magnetic fields associated with a filament and modeling of coronal magnetic fields (Bobra et al., 2008). The position of the filament is between positive and negative polarities at the photosphere (panels (a) and (b)). Panels (b) and (d) show coronal magnetic fields inferred by the flux rope insertion methods based on nonlinear force-free field extrapolation using the photospheric magnetic fields (van Ballegoijen, 2004). The dip regions of the inferred flux rope match the position of the filament (panel (c)). The method was also applied to a modeling for magnetic fields of a polar crown prominence, and the inferred flux rope well explained

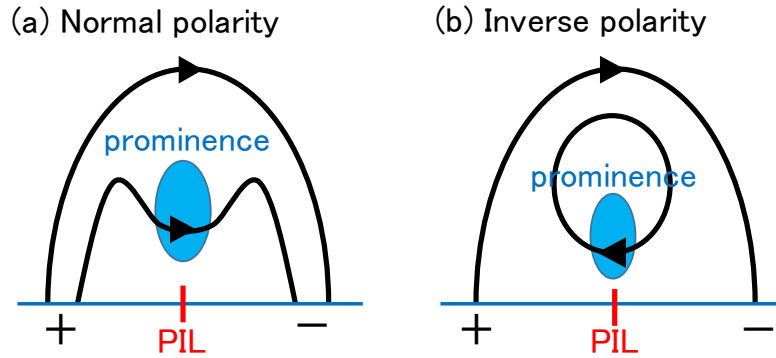


Figure 1.5: Schematic pictures of classical models of magnetic fields sustaining prominence. Panel (a) and (b) shows normal polarity model and inverse polarity model, respectively. Black lines and arrows denote magnetic fields and their orientations. Signs of + and - denote photospheric magnetic polarity.

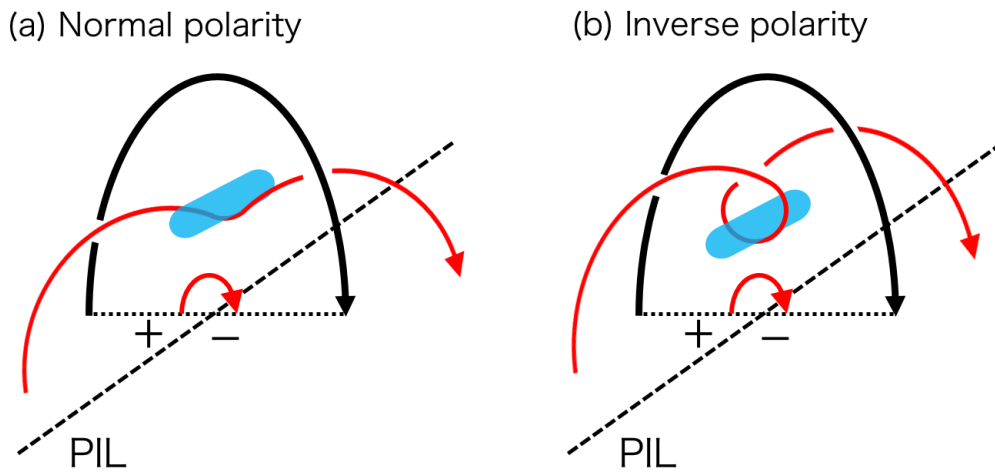


Figure 1.6: Three-dimensional magnetic structures corresponding to Fig. 1.5. Magnetic fields with a dip are shown by red lines.

height and location of the prominence (Su & van Ballegooijen, 2012).

The magnetic fields of 120 polar crown prominences were measured by Leroy et al. (1983). They concluded that all of the polar crown prominence had inverse polarities. The magnetic fields of 256 quiescent prominences at medium and low latitude were also measured by Leroy et al. (1984). They found both normal and inverse polarity prominences in their data set. They also reported that most of the normal polarity prominences exist in the lower altitudes, and the inverse polarity prominences are likely to locate in the higher altitudes.

1.4 Differential emission measure of prominence

Differential emission measure (DEM) is defined as

$$\text{DEM}(T) = n_e^2 \frac{dl}{dT}, \quad (1.1)$$

where n_e is electron number density, T is temperature, and l is distance along a line of site. DEM gives an information on mass distribution against temperature and constraints on a thermal structures in theoretical or numerical models. Intensity of a spectrum line and DEM are related as

$$I = \int n_e^2 G(n, T) dl = \int G(n, T) \text{DEM}(T) dT, \quad (1.2)$$

where I is intensity and $G(n, T)$ is a contribution function of a spectral line under optically thin and local thermodynamic equilibrium assumptions. In observations, DEM is obtained by inversion of intensities of EUV or UV lines with Eq. (1.2). DEM of prominences are obtained in previous studies as Fig. 1.8 (Wiik et al., 1993; Cirigliano et al., 2004; Parenti & Vial, 2007; Gunár et al., 2011; Parenti et al., 2012). Numerical studies of prominence formation by radiative condensation confirmed a good agreement with an observational DEM (Karpen & Antiochos, 2008; Luna et al., 2012).

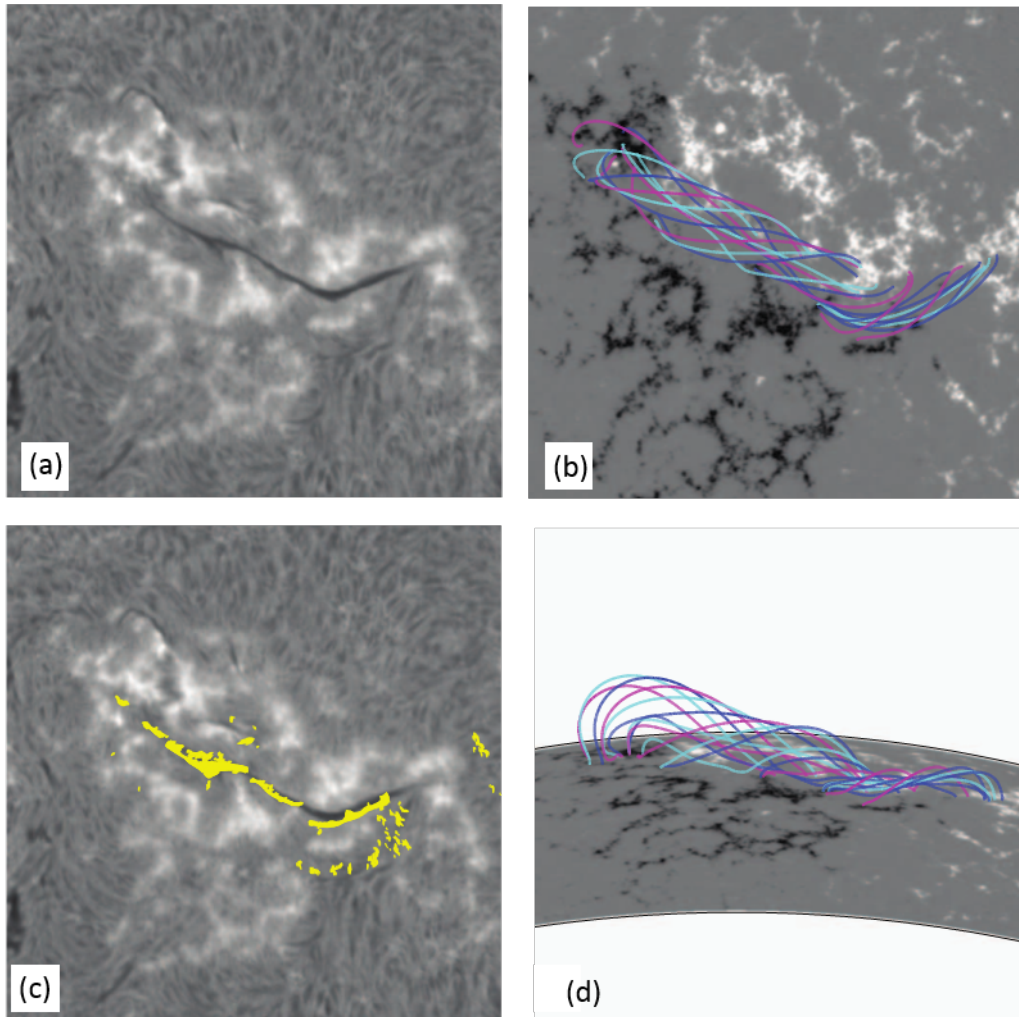


Figure 1.7: (a) H α filament (b) Gray scale represents photospheric magnetic field in the same field of view as panel (a). Lines represents inferred magnetic lines. (c) Yellow area represents dip regions of inferred flux rope structure (d) Side view of magnetic field. Images extracted from Bobra et al. (2008).

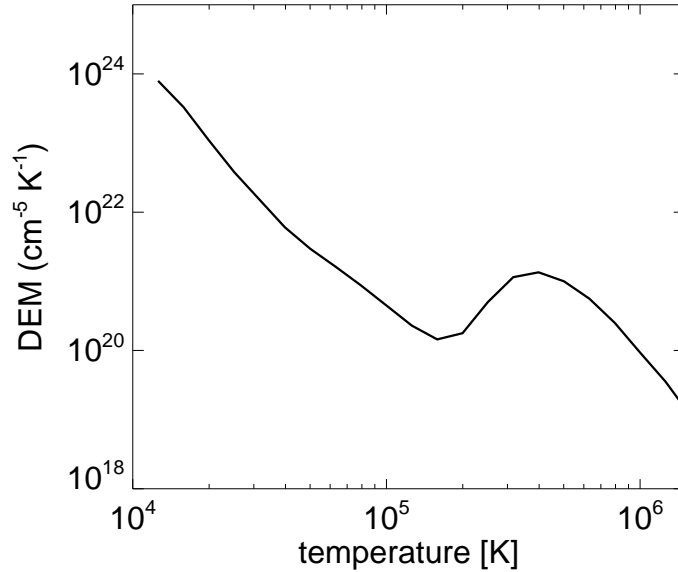


Figure 1.8: Example of observational DEM in a prominence (Wiik et al., 1993)

1.5 Prominence formation: Observations

1.5.1 Reconnection at PIL

Observational studies have reported some events that prominences formed after a collision of a pair of positive and negative photospheric polarities with each other (Gaizauskas et al., 1997; Wang & Muglach, 2007; Yang et al., 2016). Figure 1.9 is an example in Yang et al. (2016). In this event, positive and negative polarities interacted with each other (inset in panel (a) in Fig. 1.9) with EUV brightening (panels (a) and (b)). These two opposite-signed magnetic polarities were footpoints of two different coronal loops, and are interacted by a photospheric converging motion. Dark filamentary structures appear in the brightening (panels (b) and (c)), and grow to a multi-thread prominence (panels (d)-(f)). The process until a brightening is interpreted by a reconnection scenario (van Ballegoijen & Martens, 1989; Martens & Zwaan, 2001). In this scenario, magnetic

reconnection between coronal loops is driven by converging motion toward the PIL, leading to the formation of a helical flux rope (Fig. 1.10). The prominence is assumed to be sustained at the dip of the flux rope, corresponding to an inverse-polarity prominence. In the observation by Yang et al. (2016), the dark prominence suddenly appeared. Because reconnection is basically a heating mechanism, the origin of cool dense plasmas is not explained in the reconnection scenario alone.

Converging motions toward a PIL is detectable by a correlation tracking in magnetogram. In the observation of Yang et al. (2016), the flows toward the PIL with the maximum speed of 0.5 km/s at the edge of the active region were detected before formation of the prominence. The diverging flows of supergranules with the maximum speed of 1.2 km/s (mean: 0.3 km/s) were detected around a PIL of a quiescent prominence by Rondi et al. (2007). They found a magnetic polarity crossing the PIL to the opposite side. The diverging flows of supergranules with the same speeds as in Rondi et al. (2007) were also detected by Schmieder et al. (2014). They found that multiple converging points were created along the PIL by coupling of multiple supergranular flows.

1.5.2 In-situ condensation

In-situ prominence formations, in which coronal plasmas are directly cooled down to prominence temperature, were found in recent observations by SDO/AIA (Berger et al., 2012; Liu et al., 2012). They observed a temporal and spatial shift of peak intensities among multiwavelength EUV emissions. Figure 1.11 (b)-(e) shows the intensity shift detected in Berger et al. (2012). The shift is from higher temperatures to lower temperatures, meaning that coronal plasmas gradually cooled down to the prominence temperature. The darkening of cavity was also observed, which indicated mass supply from the corona to the prominence. They claimed that this event was in-situ condensation because no direct

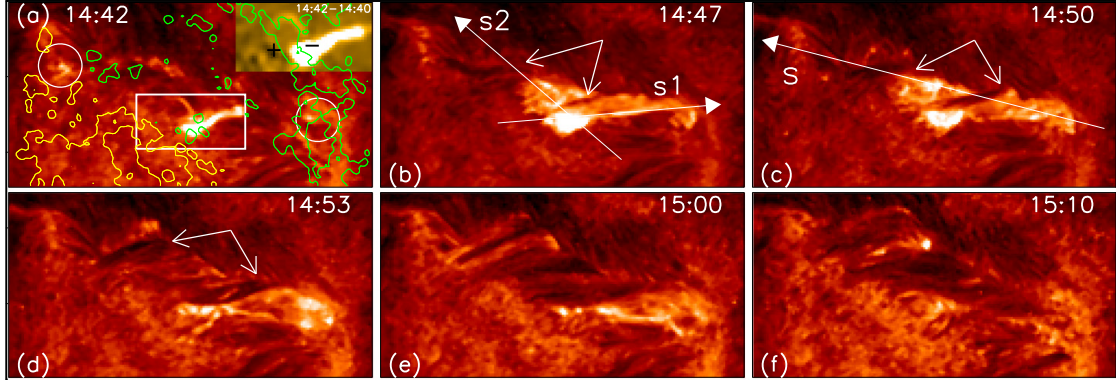


Figure 1.9: Observation of prominence formation by AIA 304 Å. Yellow and green contours represents positive and negative photospheric polarity in HMI magnetogram. The contour levels are ± 100 G. Images extracted from Yang et al. (2016).

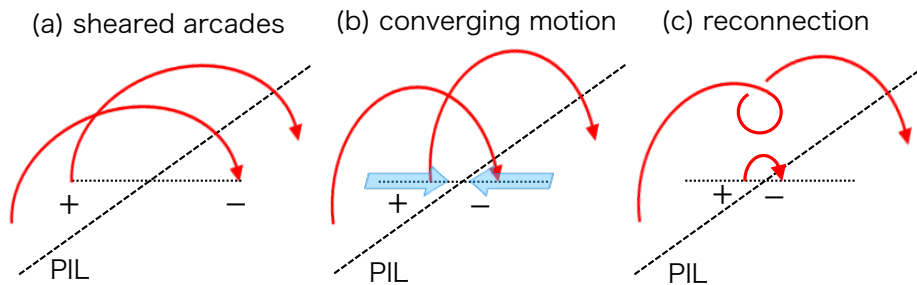


Figure 1.10: Schematic pictures of reconnection scenario. Red lines represent coronal magnetic fields. Signs of + and - denote magnetic polarity at the photosphere. Blue arrows represent converging motion. Panel (a): initial sheared arcade field, Panel (b): approaching footpoints by converging motion, Panel (c): flux rope formation by reconnection.

plasma injection from the chromosphere was observed. In-situ condensation is one of the supporting evidence of radiative condensation (see Section 1.6.2).

The coronal cavities are often observed as a dark region surrounding prominences in EUV emissions (Fig. 1.12). An elliptic shape of cavities is believed to be a manifestation of a flux rope structure. The lower intensity of cavities than that in the surrounding corona results from mass depletion (Fuller et al., 2008; Fuller & Gibson, 2009; Gibson et al., 2010; Schmit & Gibson, 2013). Hence the presence of cavity is considered as an evidence of mass supply from the corona to prominences due to condensation in a flux rope (Schmit et al., 2013; Xia et al., 2014a). Excess number of electrons in prominences is typically 1 – 40 times larger than depleted number of electrons in cavities (Saito & Hyder, 1968; Saito & Tandberg-Hanssen, 1973). Hence it is believed that mass source of huge prominences must be not only the corona but also the chromosphere.

1.5.3 Levitation by emerging flux

Some observational studies proposed that the chromospheric cool dense plasmas are lifted up to the corona by rising helical flux ropes (Okamoto et al., 2008; Lites et al., 2010). They detected directional change of the horizontal magnetic fields from normal polarity to opposite polarity beneath the filaments. These observational results can be interpreted that a rising helical flux tube is supplying mass to the filaments. On the other hand, numerical studies of flux emergence have not succeeded to demonstrate this model, because an axis of the flux tube can not break through the photosphere, namely the lower half of the flux rope remains below the photosphere (Fan, 2001; Magara, 2006). Magnetohydrodynamic (MHD) simulation by Manchester et al. (2004) shows that reconnection above the PIL of the emerging flux creates a secondary flux rope which conveys cool plasmas to the coronal height. Since they did not include radiative cooling, radiative condensation

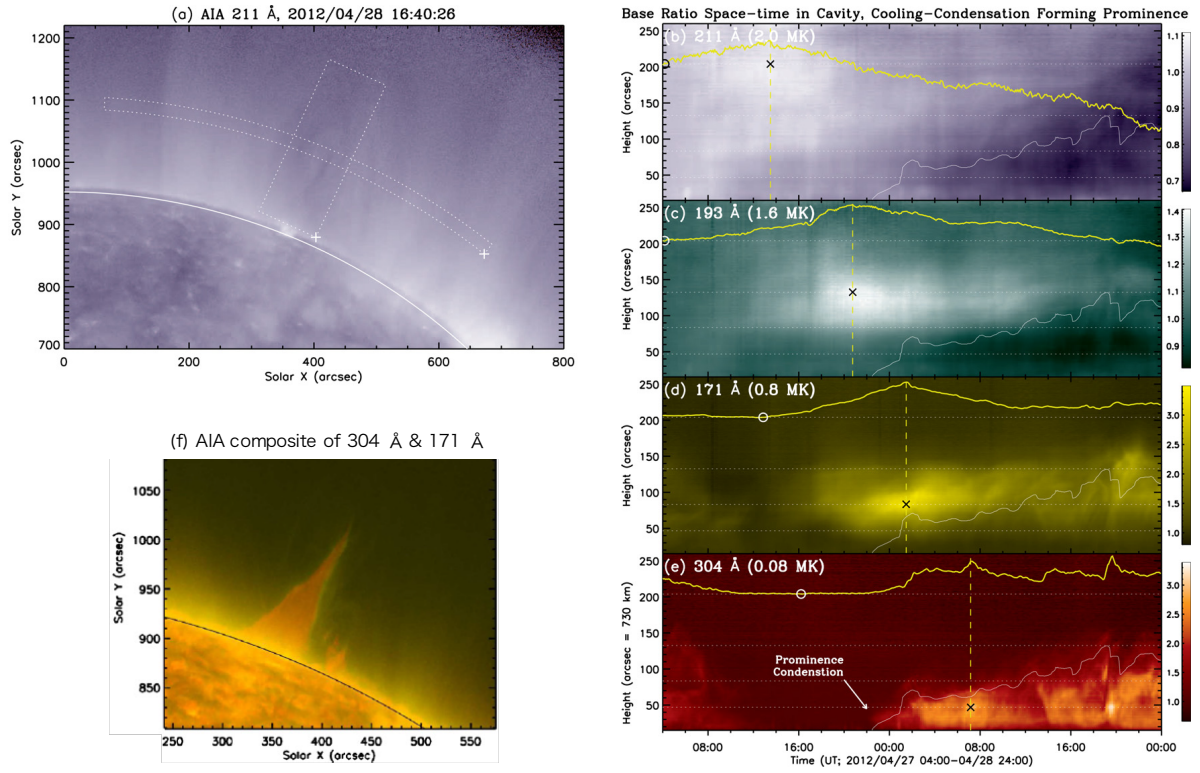


Figure 1.11: Multi-wavelength EUV emissions during prominence formation observed by SDO/AIA. Panel (a) : 211 Å image of SDO/AIA after prominence is formed, Panel (f) : prominence in the composite image of SDO/AIA 304 Å and 171 Å, Panels (b)-(e) : time - height plot of intensity ratios. Intensities in the vertical dotted box in Panel (a) are averaged. The reference image for calculating intensity ratio is indicated by a circle in each panel. Image extracted from Berger et al. (2012).

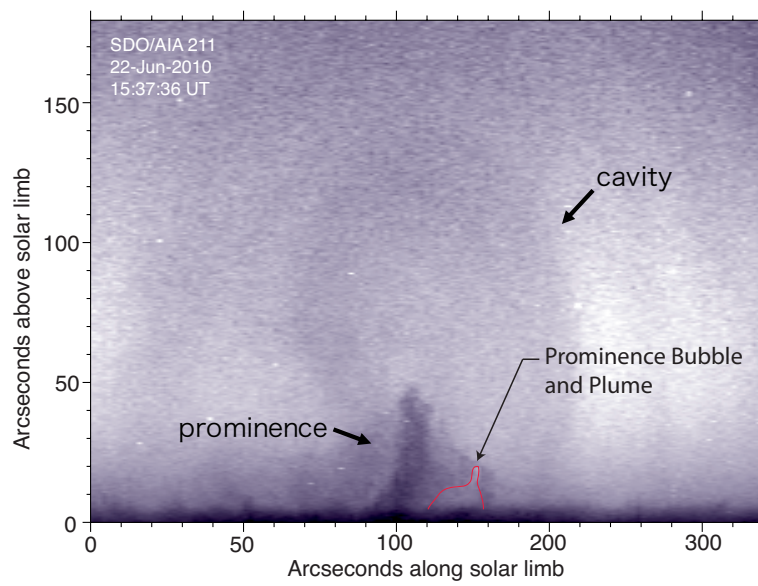


Figure 1.12: Observation of coronal cavity by SDO/AIA 211Å (image taken from Berger, 2012).

is not taken into account.

1.5.4 Injection by jet

Direct injection of chromospheric plasma by jets is also considered as a mass supply mechanism to a prominence. Mass injection rate by jets has been studied and found to be sufficient to explain prominence mass (e.g. Chae, 2003). It is, however, unclear if magnetic reconnection, which is potentially required in this model, can drive cool dense plasmas to high up to the coronal level without heating them.

1.6 Prominence formation: Theoretical approach

1.6.1 Thermal instability

One candidate to generate cool dense plasma in the corona is the thermal instability (Parker, 1953; Field, 1965). The thermal instability is triggered in a system where net cooling rate increases as entropy decreases. Field (1965) performed linear analysis for hydrodynamic equations with thermal conduction and net cooling terms, and derived critical conditions of the instability. Let me start from a description on the criteria without thermal conduction. The isochoric criterion for instability is,

$$\left(\frac{\partial \mathbf{L}}{\partial T}\right)_\rho < 0, \quad (1.3)$$

where T is temperature, ρ is density, $\mathbf{L}(\rho, T)$ is heat-loss function defined as energy losses minus energy gains per mass. The subscript ρ represents differentiation at a constant density. The criterion Eq. (1.3) represents a positive-feedback system that net cooling increases as temperature decreases. Once temperature starts to decrease, enhanced cooling decreases temperature more, resulting in catastrophic cooling. The isochoric situation is

actually difficult to be achieved in general, because the local pressure decrease by cooling drives mass motions and changes the density distribution. The isobaric criterion for instability, on the other hand, is,

$$\left(\frac{\partial \mathbf{L}}{\partial T}\right)_p = \left(\frac{\partial \mathbf{L}}{\partial T}\right)_\rho - \frac{\rho}{T} \left(\frac{\partial \mathbf{L}}{\partial \rho}\right)_T < 0. \quad (1.4)$$

This criterion considers the increase of net cooling rate with density increase, and is a weaker condition compared to Eq. (1.3). Coronal optically thin radiative cooling rate per volume is represented by $n^2 \Lambda(T)$ where n is number density and $\Lambda(T)$ is the radiative loss function shown in Fig. 1.13. Assuming that the radiative loss function is expressed by

$$\Lambda = \chi T^\alpha, \quad (1.5)$$

where χ and α are constants, and assuming that heating terms do not depend on local density and temperature, the isobaric criterion for instability Eq. (1.4) is rewritten as

$$\alpha < 1. \quad (1.6)$$

As shown in Fig. 1.13 the exponent of radiative loss function above 10^5 K is smaller than unity. Thus the corona is thermal unstable without thermal conduction.

In case that thermal conduction is not negligible, the isobaric criterion for instability is given as

$$\left(\frac{\partial \mathbf{L}}{\partial T}\right)_\rho - \frac{\rho}{T} \left(\frac{\partial \mathbf{L}}{\partial \rho}\right)_T < -\frac{K}{\rho} k^2, \quad (1.7)$$

where K is conduction coefficient and k is wave number. Thermal conduction can compensate the thermal imbalance of a perturbation, hence, the critical condition to trigger the instability becomes severe. By assuming the radiative loss function in the form of Eq. (1.5), the criterion for instability is given

$$\lambda > \lambda_F, \quad (1.8)$$

where $\lambda = 2\pi/k$ is the wave length of a perturbation and λ_F is the Field length given as

$$\lambda_F = \frac{2\pi}{\sqrt{1-\alpha}} \sqrt{\frac{KT}{n^2\Lambda}} \sim \sqrt{\frac{KT}{n^2\Lambda}}. \quad (1.9)$$

In quiet regions ($n = 10^8 \text{ cm}^{-3}, T = 10^6 \text{ K}$), the Field length is around 150 Mm, and that in active regions ($n = 10^9 \text{ cm}^{-3}, T = 2 \times 10^6 \text{ K}$) is around 60 Mm. Length of coronal loop ranges in 10 – 100 Mm, which is comparable to the Field length. If perturbations are generated inside a coronal loop, the wavelength of perturbations is likely to be shorter than the loop length and the Field length. Thus, it is difficult to cause the thermal instability in coronal loops due to strong relaxation by thermal conduction.

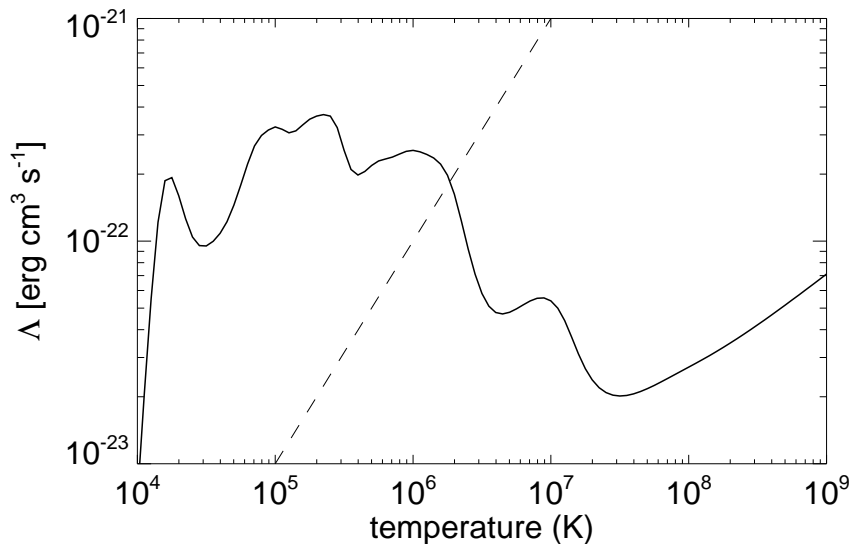


Figure 1.13: Radiative loss function calculated by CHIANTI (Schmelz et al., 2012). Dashed line is proportional to temperature, shown for visual comparison with the exponents of radiative loss function.

1.6.2 Radiative condensation model

As explained in the previous section, the coronal loops are thermally stable for a linear perturbation. For overcoming this stability, several models including nonlinear triggers of radiative condensation have been proposed. One is evaporation-condensation model (Mok et al., 1990; Antiochos & Klimchuk, 1991; Antiochos et al., 1999; Karpen et al., 2001, 2003, 2005, 2006; Karpen & Antiochos, 2008; Xia et al., 2011; Luna et al., 2012; Xia et al., 2012; Keppens & Xia, 2014; Xia & Keppens, 2016a). In this model, radiative condensation is triggered by an enhancement of the plasma density through the evaporation process, which is driven by the strong steady heating artificially imposed at a footpoint of a coronal loop. The critical condition for a condensation in this model has been investigated in detail by one-dimensional hydrodynamic simulations. Recently this model has been demonstrated by multi-dimensional simulations (Xia et al., 2012; Keppens & Xia, 2014; Xia & Keppens, 2016a). The crucial factor in this model is the ratio of the spatial scale of footpoint heating against the loop length. If the ratio is less than 10 – 20 %, radiative condensation is triggered. The problem of this model is the lack of clear observational evidence nor theoretical support for the artificial strong footpoint heating. The estimation from X-ray data suggested a spatially uniform heating (Priest et al., 2000), while that from EUV data suggested nonuniform heating localized at footpoint with spatial scale 10 – 20 Mm (Aschwanden et al., 2000). Further study is required to conclude the spatial distribution of coronal heating. The other crucial factor of evaporation-condensation model is duration of footpoint heating. The steady footpoint heating is necessary until radiative cooling overwhelms the background heating by mass input. How such a strong heating is maintained for a long duration is not clear. Another limitation in evaporation-condensation model is a height of prominence. Since evaporation can inject plasma at most to the height of coronal scale height (~ 60 Mm), low-lying prominences can be

explained, while prominences at high altitude can not be explained.

Choe & Lee (1992) proposed a model in which a shearing motion along a PIL leads to radiative condensation, and demonstrated it by 2.5-dimensional MHD simulations. A coronal arcade field expands by the magnetic pressure enhancement near the surface driven by the imposed shearing motion. If the expansion occurs faster than cooling time scale, pressure and temperature inside the arcade field decreases by the adiabatic expansion. The mass comes from the chromosphere due to the pressure decrease, leading to density increase (by siphon-like mechanism). Because of the density increase and the temperature decrease, radiative cooling is enhanced enough to cause radiative condensation, resulting in the formation of normal polarity prominence. This model does not explain the formation of inverse polarity prominences with flux ropes. Linker et al. (2001) modeled formation of an inverse polarity prominence in their two-dimensional MHD simulation. In their model, reconnection is driven at a PIL and a flux rope is formed. Chromospheric plasmas are lifted up with the rising flux rope to the coronal height, and condensed by radiative cooling. In this model, the chromospheric cool dense plasmas are directly lifted up, which is not consistent with some recent observational findings (Berger et al., 2012; Liu et al., 2012). This model is rather similar to the levitation model introduced in Section 1.5.3.

1.7 Interior dynamics of prominence

Fine structures and internal flows are observed in interiors of prominences (Engvold, 1976, 1981; Zirker et al., 1994, 1998; Chae et al., 2008; Chae, 2010; Hillier et al., 2012b; Berger et al., 2008, 2010).

1.7.1 Fine structures

In observations on the solar disk, prominences are composed of a number of horizontal threads (Martin, 1998a; Lin et al., 2005). Width of threads is typically 200 km (Mackay et al., 2010). They are thought to be a manifestation of local magnetic fields. In observations at the limb, active region prominences are composed with horizontal threads (e.g. Okamoto et al., 2007), while quiescent prominences are composed of vertical threads (e.g. Berger et al., 2010, see Fig. 1.2). It is unclear why prominences show such a different orientation of fine structures in the limb observations. The measurement of magnetic fields by the Hanle effect indicated that horizontal magnetic fields are dominant in quiescent prominences (Leroy et al., 1983, 1984; Casini et al., 2003; Orozco Suárez et al., 2014), which conflicts with the vertically oriented fine structures. Explaining the existence of vertical threads with horizontal magnetic field is one issue on interior dynamics of prominence.

1.7.2 Vertical flows

In the interior of quiescent prominences, dark plumes rising from the base of a prominence are observed (Berger et al., 2008, 2010, 2011). The width of plumes is 200 – 700 km and the upward speeds are typically 20 km/s. Descending knots along vertical threads with a speed of 15 km/s are also observed (Berger et al., 2008, 2010; Chae, 2010). The descending speed is smaller than free-fall speed, indicating that magnetic tension force support the plasma against gravity (Chae, 2010).

Since the dense plasmas of prominence locate above the low density coronal plasmas, the Rayleigh-Taylor instability was proposed as a driving mechanism of upflows and downflows. Three-dimensional ideal MHD simulations succeeded in modeling the rising plumes by the Rayleigh-Taylor instability (Hillier et al., 2011, 2012a; Keppens et al., 2015). The

problem of this model is the omission of horizontal magnetic field seen in observations (e.g. Leroy et al., 1984). In case that horizontal magnetic field is dominant in quiescent prominences, perturbations can not evolve due to suppression by magnetic tension force. Considering ambipolar diffusion of weakly ionized plasma is one idea to overcome this effect (Khomenko et al., 2014; Díaz et al., 2014). Since the motion of neutrals is not restricted by magnetic field, the Rayleigh-Taylor instability is not suppressed against any wavelength.

Vertical flows affect mass budget of prominence. Prominence mass is drained by downflows and may be supplied by upflows. Mass drainage rate by downflows is estimated as order of 10^{10} g s^{-1} (Zirker et al., 1994; Liu et al., 2012). Assuming prominence mass as $10^{13} - 10^{14} \text{ g}$, prominence would disappear in several tens of minutes to several hours without any mass input. Typical lifetime of quiescent prominences is a few days to months. Therefore, there should be a simultaneous mass supply to maintain a prominence mass. In an in-situ prominence formation event observed by Liu et al. (2012), no mass upflows were detected and radiative condensation rate was comparable to mass drainage rate.

1.7.3 Turbulence

Recent studies investigated the properties of turbulence in a quiescent prominence by analyzing data of intensity (Leonardis et al., 2012) or velocities (Freed et al., 2016; Hillier et al., 2016). They all found a break of scaling exponent in power spectrum or structure functions at around 2000 km in the spatial scale. Hillier et al. (2016) found strong turbulence in the larger scale and weak turbulence in the smaller scale, which is opposite that expected by the theory of MHD turbulence. Further studies are necessary to understand the turbulent nature in prominence.

1.8 Motivation

Prominences are one of the basic structures in the corona, and important subjects of studies in solar physics and solar-terrestrial physics. Despite their importance, the formation mechanism of prominences, i.e., the origin of their magnetic fields and cool dense plasmas, has not been well established.

Thermal stability of the corona is a key point to overcome for a prominence formation. The question is how the corona can be locally unstable for thermal perturbations in spite of the strong relaxation by thermal conduction. The radiative condensation (thermal instability) model is one promising idea to explain the origin of cool dense plasmas. Since prominences always appear along PILs, it is possible that reconnection is a trigger of radiative condensation. Since thermal conduction works only along the field lines in the corona, reconnection may switch the thermal stability of the local corona by changing the configuration of magnetic fields. In the previous studies, reconnection and radiative condensation has been regarded as an independent process from each other, and these two processes have been simulated separately (Xia et al., 2014a,b; Xia & Keppens, 2016a). So far, the physical link between reconnection and radiative condensation has not been studied well.

Observations suggest that internal vertical flows affect mass budget of prominence: mass supply by radiative condensation and mass drainage by downflows are comparable and correlated (Liu et al., 2012). A theory including both condensation and internal downflows is necessary to discuss a dynamic equilibrium of prominences. So far, few numerical modeling has achieved to include these two processes (only Xia & Keppens (2016a) to our knowledge).

Revealing formation mechanism and mass maintenance mechanism of prominences are both important issues in solar physics. In this thesis, we propose a new prominence

formation model, *reconnection-condensation model*, in which radiative condensation is triggered by reconnection, and demonstrate it by multi-dimensional MHD simulations including radiative cooling and nonlinear anisotropic thermal conduction. To validate our formation model, we synthesize EUV emissions and DEM, and investigate EUV emission shift in multi-wavelength (see Fig. 1.11), dark cavity formation around prominence (see Fig. 1.12), and DEM curve against temperature (see Fig. 1.8). We also attempt to reproduce the interior dynamics of prominence using our newly developed three-dimensional prominence formation model, and investigate a coupling effect of radiative condensation and internal flows on mass budget of prominences.

Chapter 2

Reconnection-Condensation Model

2.1 Introduction

The purpose of this study in this chapter is to propose a new prominence formation model, reconnection-condensation model. We point out that magnetic reconnection can cause radiative condensation for prominence formation. To achieve the purpose, we perform multi-dimensional MHD simulations including thermal conduction and radiative cooling in the corona, and demonstrated the proposed model. In addition, we perform a parameter survey to obtain the conditions for radiative condensation of the proposed model.

The chapter is organized as follows: We introduce the basic idea of reconnection-condensation model in Section 2.2. In Section 2.3, the model is demonstrated by two-dimensional MHD simulations including nonlinear anisotropic thermal conduction. The parameter survey on the footpoint motions, coronal heating models, and coronal densities is performed, and the condition for radiative condensation is investigated. In Section 2.4, the model is demonstrated by three-dimensional simulations and the condition for radiative condensation is extended from that in two-dimensional simulations. Section 2.5 is discussion and summary of this chapter.

2.2 Basic idea of reconnection-condensation model

The basic concept of reconnection-condensation model is as follows. Initially, a coronal arcade exists in thermal equilibrium state (Fig. 2.1 (a)). The arcade field is transformed into a flux rope structure by converging motion at footpoints. The relatively dense plasmas in the lower corona due to stratification are trapped inside the closed loops of the flux rope, where they are elevated into the upper corona (Fig. 2.1 (b)). The dense plasmas increase the radiative cooling inside the flux rope, leading to cooling-dominant thermal imbalance. The thermal imbalance is not compensated because the closed geometry of magnetic field inhibits the heat flux from the exterior of the flux rope. Eventually, the interior of the flux rope suffers from radiative condensation (Fig. 2.1 (c)).

This model does not require artificial strong steady footpoint heating which is not confirmed by observation. Instead, we adopt reconnection by footpoint motion suggested by observation (Gaizauskas et al., 1997; Wang & Muglach, 2007; Yang et al., 2016). In evaporation-condensation model, prominence formation in high altitudes can not be explained, because evaporation flows can reach at most the altitude comparable to the coronal scale height. In our model, the height of flux rope is not restricted by scale height. Our model can explain prominence formation at high altitudes in principle.

2.3 Two-dimensional simulations

In this section, to demonstrate the proposed model, we perform 2.5-dimensional MHD simulations, including thermal conduction along the magnetic field lines, radiative cooling, and gravity. To investigate the necessary condition for triggering radiative condensation, we test different types of the footpoint motions and coronal heating models. The footpoint motion determines the overall evolution of coronal magnetic field and subsequent density

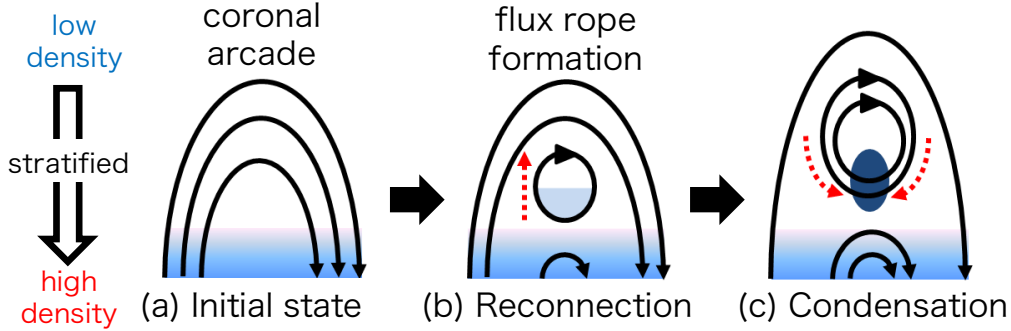


Figure 2.1: Schematic overview of reconnection-condensation model.

distribution inside a flux rope (Amari et al., 2000; Xia et al., 2014b). It may affect radiative cooling rate in a flux rope.

2.3.1 Numerical Settings

Initial condition

The simulation domain is a rectangular box in Cartesian coordinate (x, y) extending in $-12 \text{ Mm} < x < 12 \text{ Mm}$ and $0 < y < 40 \text{ Mm}$, where the x - and y -axes are horizontal and vertical, respectively, and the z -axis is orthogonal to the x - y plane. The initial corona is stratified under uniform temperature ($T_{\text{cor}} = 1\text{MK}$) and gravity ($g_{\text{cor}} = 2.7 \times 10^4 \text{ cm s}^{-2}$),

$$n(y) = n_{\text{cor}} \exp\left[-\frac{mg_{\text{cor}}}{k_B T_{\text{cor}}} y\right], \quad (2.1)$$

$$p(y) = \frac{k_B}{m} \rho(y) T_{\text{cor}}, \quad (2.2)$$

where n_{cor} is number density at the bottom boundary, k_B is Boltzmann's constant, and m is the mean molecular mass. We test cases of $n_{\text{cor}} = 1.0 \times 10^9 \text{ cm}^{-3}$ and $n_{\text{cor}} = 5.0 \times 10^8 \text{ cm}^{-3}$. We set $m = m_p$ with m_p being the proton mass. Note that the mean molecular mass of the fully ionized corona is given as $m = 0.5m_p$, whereas that in prominence

consisting of partially ionized plasma is $m = 1.12m_p$ with an ionization degree of hydrogen 0.2 and a 10:1 abundance of hydrogen and helium. More accurate treatment of mean molecular mass is, for instance, calculating ionization degree by the Saha equation under the assumption of local thermodynamic equilibrium. For simplicity we omit calculating ionization degree, and adopt proton mass as a mean molecular mass. The force-free arcade field is described as

$$B_x = -\left(\frac{2L_a}{\pi a}\right) B_a \cos\left(\frac{\pi}{2L_a}x\right) \exp\left[-\frac{y}{a}\right], \quad (2.3)$$

$$B_y = B_a \sin\left(\frac{\pi}{2L_a}x\right) \exp\left[-\frac{y}{a}\right], \quad (2.4)$$

$$B_z = -\sqrt{1 - \left(\frac{2L_a}{\pi a}\right)^2} B_a \cos\left(\frac{\pi}{2L_a}x\right) \exp\left[-\frac{y}{a}\right], \quad (2.5)$$

where $B_a = 3$ G is the field strength at the footpoint, $L_a = 12$ Mm is the width, and $a = 30$ Mm is the magnetic scale height of the arcade field. Initially, the system exists in mechanical equilibrium.

Boundary conditions

The left and right boundaries are subjected to symmetric (for ρ, p, v_y, B_y) and anti-symmetric (for v_x, v_z, B_x, B_z) boundary conditions. A free boundary condition is applied to the top. In the region below $y = 0$, the converging and shearing motions are introduced. We test three types of the footpoint motions. One is the converging motion without shearing; the others are converging motion with shearing that increases the magnetic shear of the arcade field or with anti-shearing that decreases the shear of the arcade field. In all the cases, the velocity components v_x and v_y within this region are set as follows,

$$v_x = -v_0(t) \sin\left(\frac{\pi x}{2L_a}\right), \quad (2.6)$$

$$v_y = 0, \quad (2.7)$$

$$v_0(t) = \begin{cases} v_{00}, & (0 < t < t_1) \\ v_{00} \frac{t_2 - t}{t_2 - t_1}, & (t_1 \leq t < t_2) \\ 0, & (t \geq t_2) \end{cases} \quad (2.8)$$

$$v_0(t) = \begin{cases} v_{00} \frac{t_2 - t}{t_2 - t_1}, & (t_1 \leq t < t_2) \end{cases} \quad (2.9)$$

$$v_0(t) = \begin{cases} 0, & (t \geq t_2) \end{cases} \quad (2.10)$$

where t is time. We test the case of $v_{00} = 12$ km/s, $t_1 = 1200$ s, and $t_2 = 1440$ s, or $v_{00} = 6$ km/s, $t_1 = 2400$ s, and $t_2 = 2640$ s. In the case of no shearing motion, $v_z = 0$. The shearing and the anti-shearing motions are set as follows,

$$v_z = \pm v_0(t) \sin\left(\frac{\pi x}{2L_a}\right) \quad (2.11)$$

where the plus and minus signs represent the shearing and anti-shearing motions, respectively. The converging motion is added to create a flux rope by reconnection. Reconnection by converging motion was proposed to explain prominence formation associated with interaction of opposite polarities at a PIL in observations (Gaizauskas et al., 1997; Wang & Muglach, 2007; Yang et al., 2016). The shearing motion was proposed as a mechanism to create highly sheared arcade field (van Ballegooijen & Martens, 1989). It is numerically demonstrated that shearing motion drives eruption (e.g. Amari et al., 2000). To create a mechanically stable flux rope, we test anti-shearing motion which suppresses eruption by increasing downward magnetic tension force. As discussed later in Section 2.5, both shearing and anti-shearing motion can be created by coupling of supergranular flows.

The magnetic fields are computed with the induction equation by coupling with the given converging and shearing motions. Free boundary condition is applied to the magnetic fields at the bottom boundary. The gas pressure and density are assumed to be in hydrostatic equilibrium at a constant temperature of $T_{\text{cor}} = 10^6$ K. Detailed description is in Appendix A.

Basic equations

The basic equations are MHD equations including gravity, Spitzer type thermal conductivity (Spitzer, 1962), and optically thin radiative cooling given as

$$\frac{\partial \rho}{\partial t} + \nabla \cdot (\rho \mathbf{v}) = 0, \quad (2.12)$$

$$\frac{\partial (\rho \mathbf{v})}{\partial t} + \nabla \cdot \left(\rho \mathbf{v} \mathbf{v} + p \mathbf{I} - \frac{\mathbf{B} \mathbf{B}}{4\pi} + \frac{B^2}{8\pi} \mathbf{I} \right) - \rho \mathbf{g} = 0, \quad (2.13)$$

$$\begin{aligned} \frac{\partial}{\partial t} \left(e_{\text{th}} + \frac{1}{2} \rho \mathbf{v}^2 + \frac{B^2}{8\pi} \right) + \nabla \cdot \left[\left(e_{\text{th}} + p + \frac{1}{2} \rho \mathbf{v}^2 \right) \mathbf{v} + \frac{c}{4\pi} \mathbf{E} \times \mathbf{B} \right] \\ = \rho \mathbf{g} \cdot \mathbf{v} + \nabla \cdot (\kappa T^{5/2} \mathbf{b} \mathbf{b} \cdot \nabla T) - n^2 \Lambda(T) + H, \end{aligned} \quad (2.14)$$

$$e_{\text{th}} = \frac{p}{\gamma - 1}, \quad (2.15)$$

$$\frac{\partial \mathbf{B}}{\partial t} = -c \nabla \times \mathbf{E}, \quad (2.16)$$

$$\mathbf{E} = -\frac{1}{c} \mathbf{v} \times \mathbf{B} + \frac{4\pi\eta}{c^2} \mathbf{J}, \quad (2.17)$$

$$\mathbf{J} = \frac{c}{4\pi} \nabla \times \mathbf{B}, \quad (2.18)$$

where and $\kappa = 2 \times 10^{-6} \text{ erg cm}^{-1} \text{ s}^{-1} \text{ K}^{-7/2}$ is the coefficient of thermal conduction, \mathbf{b} is a unit vector along the magnetic field, n is number density, $\Lambda(T)$ is the radiative loss function of optically thin plasma, H is the background heating rate, $\mathbf{g} = (0, -g_{\text{cor}}, 0)$ is the gravitational acceleration and η is the magnetic diffusion rate. The temperature is computed by the following equation of state,

$$T = \frac{m p}{k_B \rho}. \quad (2.19)$$

For fast reconnection, we adopt the following form of the anomalous resistivity (e.g. Yokoyama & Shibata, 1994),

$$\eta = \begin{cases} 0, & (J < J_c) \\ \eta_0 (J/J_c - 1)^2, & (J \geq J_c) \end{cases} \quad (2.20)$$

$$\eta = \eta_0 (J/J_c - 1)^2, \quad (J \geq J_c) \quad (2.21)$$

where $\eta_0 = 3.6 \times 10^{13} \text{ cm}^2 \text{ s}^{-1}$ and $J_c = 25 \text{ erg}^{1/2} \text{ cm}^{-3/2} \text{ s}^{-1}$. We restrict η to $\eta_{\max} = 18.0 \times 10^{13} \text{ cm}^2 \text{ s}^{-1}$. We adopt a simplified radiative loss function in Fig. 2.2 (Hildner, 1974) and simulate two different coronal heating models. In one model, the heating rate H depends on the local magnetic energy density (magnetic pressure) T_c and is balanced out by the cooling rate when it falls below T_c ,

$$H = \alpha_M P_m, \quad (T \geq T_c) \quad (2.22)$$

Initial thermal equilibrium required that

$$\alpha_M = \frac{n_{\text{cor}}^2 \Lambda(T_{\text{cor}})}{B_a^2 / 8\pi} \exp \left[-2 \left(\frac{mg_{\text{cor}}}{k_B T_{\text{cor}}} - \frac{1}{a} \right) y \right]. \quad (2.23)$$

Selecting $a = k_B T_{\text{cor}} / (mg_{\text{cor}}) = 30 \text{ Mm}$, we obtain a constant $\alpha_M = 1.5 \times 10^{-4} \text{ cm}^3 \text{ s}^{-1}$ when $n_{\text{cor}} = 1.0 \times 10^9 \text{ cm}^{-3}$ and $\alpha_M = 3.8 \times 10^{-5} \text{ cm}^3 \text{ s}^{-1}$ when $n_{\text{cor}} = 5.0 \times 10^8 \text{ cm}^{-3}$. In the other model, the heating rate H depends on the local density and magnetic field strength as

$$H = \alpha_N n B. \quad (2.24)$$

For the initial thermal equilibrium, we have $\alpha_N = 1.9 \times 10^{-14} \text{ erg}^{-1/2} \text{ cm}^{-3/2} \text{ s}^{-1}$.

Numerical scheme

The numerical scheme is 4-stage Runge-Kutta method (Vögler et al., 2005) and 4th-order central finite difference method with artificial viscosity (Rempel, 2014). Thermal conduction is explicitly solved by super-time-stepping method with second-order temporal and spatial accuracy (Meyer et al., 2012; Meyer et al., 2014). The grid spacing size is 120 km everywhere.

case	heating	v_{00}	shearing	n_{cor}	Condensation
M1	$H \propto P_m$	12 km/s	–	$1 \times 10^9 \text{ cm}^{-3}$	Yes
M2	$H \propto P_m$	12 km/s	0	$1 \times 10^9 \text{ cm}^{-3}$	No
M3	$H \propto P_m$	12 km/s	+	$1 \times 10^9 \text{ cm}^{-3}$	No
N1	$H \propto nB$	12 km/s	–	$1 \times 10^9 \text{ cm}^{-3}$	Yes
N2	$H \propto nB$	12 km/s	0	$1 \times 10^9 \text{ cm}^{-3}$	No
N3	$H \propto nB$	12 km/s	+	$1 \times 10^9 \text{ cm}^{-3}$	No
L	$H \propto P_m$	12 km/s	–	$5 \times 10^8 \text{ cm}^{-3}$	Yes
S	$H \propto P_m$	6 km/s	–	$1 \times 10^9 \text{ cm}^{-3}$	Yes

Table 2.1: The presence of radiative condensation in each case. The second column shows the heating model. The third column shows the speed of footpoint motion. The fourth column shows the shearing model: plus sign (+), minus sign (–), and 0 represent the shearing, anti-shearing, and no shearing cases, respectively. The fifth column shows initial coronal density at the bottom boundary. The sixth column shows the presence of condensation.

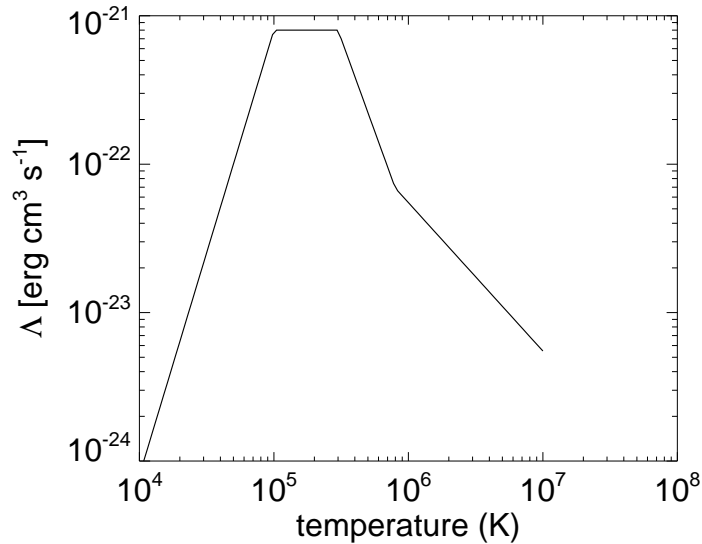


Figure 2.2: Simplified radiative cooling function.

2.3.2 Results

The investigated cases and their results are summarized in Table 2.1. The right-most column of Table 2.1 shows our results in the presence of the radiative condensation. We find that the necessary condition for the radiative condensation is anti-shearing motion. Panels (a)-(d) of Figs. 2.3 and 2.4 are snapshots of the time evolution of case M1, which is the typical case for the radiative condensation. In this case, not only converging motion toward the PIL but also the anti-shearing motion parallel to the PIL which reduces magnetic shear of the arcade field are imposed at the footpoint region. The initial state exists in mechanical and thermal equilibrium (Fig. 2.3 (a) and (b)). Converging motion triggers reconnection above the PIL at $x = 0$, and a flux rope is formed (Fig. 2.3 (c) and (d)). As the reconnection proceeds, the relatively dense plasmas in the lower corona are trapped inside the flux rope and lifted to the upper corona (Fig. 2.3 (d)). The solid lines

in Fig. 2.5 (a) and (b) show cooling rate and heating rate along y -axis at $t = 24$ min. The radiative cooling inside the flux rope is enhanced by the dense plasmas, and overwhelms the background heating. Because thermal conduction works only along closed magnetic field lines of the flux rope, it can not compensate the cooling-dominant thermal imbalance. Consequently, radiative condensation is triggered, and the cool dense plasmas accumulate in the lower part of the flux rope (Fig. 2.4 (a) and (b)). The low density region appears around prominence by mass depletion. It is consistent with the observation of cavities. The prominence mass descends with the flux rope to the bottom boundary (Fig. 2.4 (c) and (d)).

Figures 2.6 and 2.7 show snapshots of the time evolution of cases M2 and M3. In case M2, only converging motion toward the PIL is imposed at the footpoint region. In case M3, footpoint motion parallel to the PIL which increases magnetic shear of the arcade field is added. These cases results in no condensation and finally erupt. The dashed lines and dash-dotted lines in Fig. 2.5 show cooling rate and heating rate along y -axis of cases M2 and M3. In contrast to case M1, the radiative cooling in these cases does not overwhelm the background heating. Figure 2.8 shows maximum temperature versus time. Temperature in a flux rope continues to increase in these cases because radiative cooling decreases as temperature increases. In addition, the heating-dominant state is not relaxed by thermal conduction due to the closed geometry of magnetic fields. This is the thermal instability proceeding to heating. Detailed mechanisms on how a system switches cooling-dominant or heating-dominant state is discussed in next section.

Figures 2.9 shows snapshots of the time evolution of case N1. The process to trigger radiative condensation is the same as in case M1. Until $t = 24$ min (Fig. 2.9 (a) and (b)), there is no significant difference in time evolution between case N1 and M1. A difference exists in properties of the prominences. Figure 2.10 shows density and temperature along

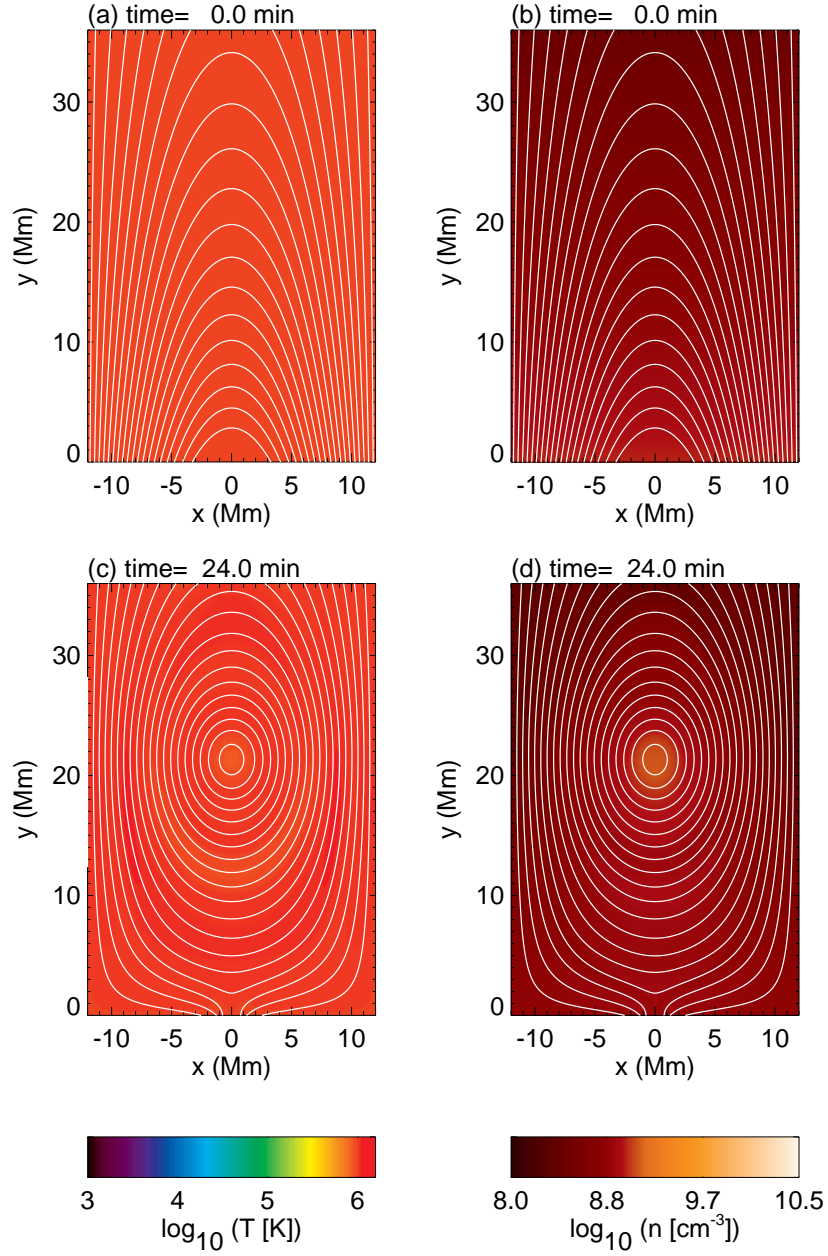


Figure 2.3: Snapshots of time evolution in case M1. Colors represent temperature and density, white lines represents magnetic field lines.

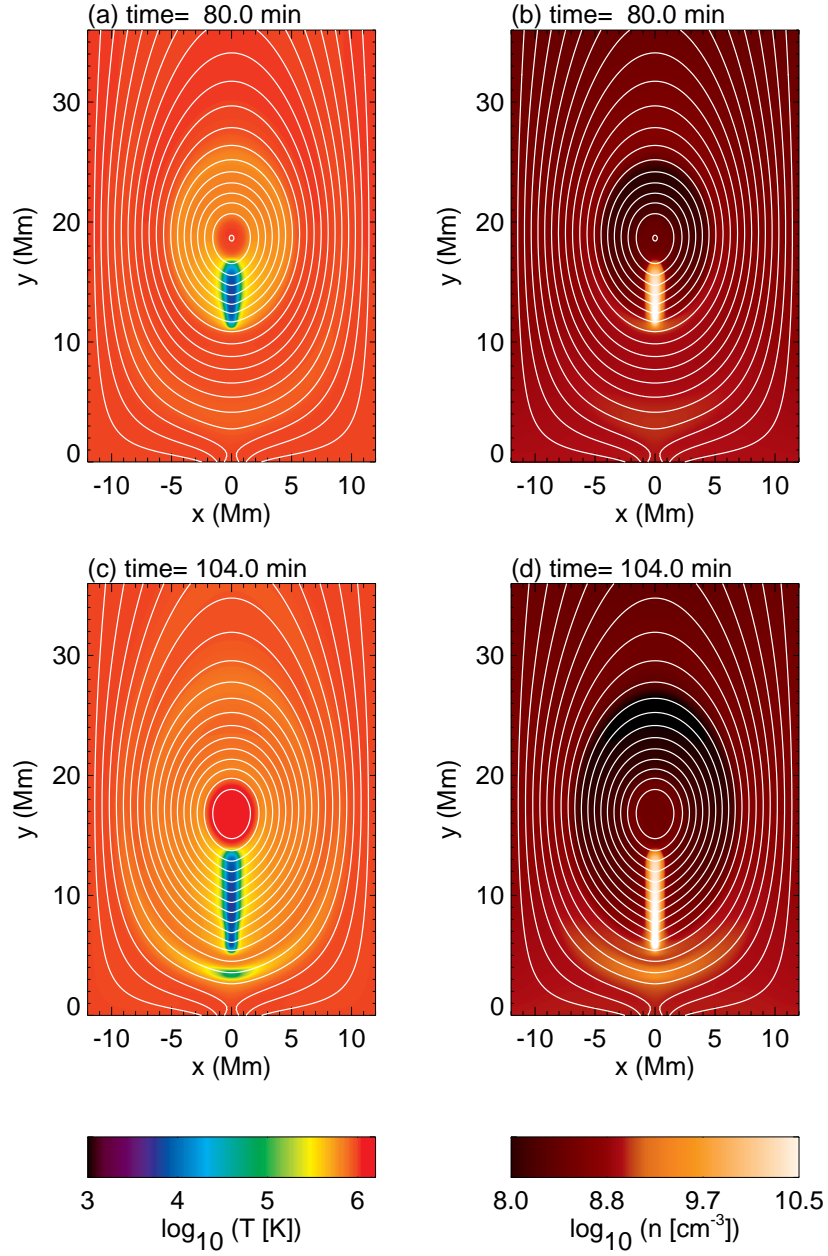


Figure 2.4: Snapshots of time evolution in case M1. Colors and white lines are the same quantities as in Fig. 2.3.

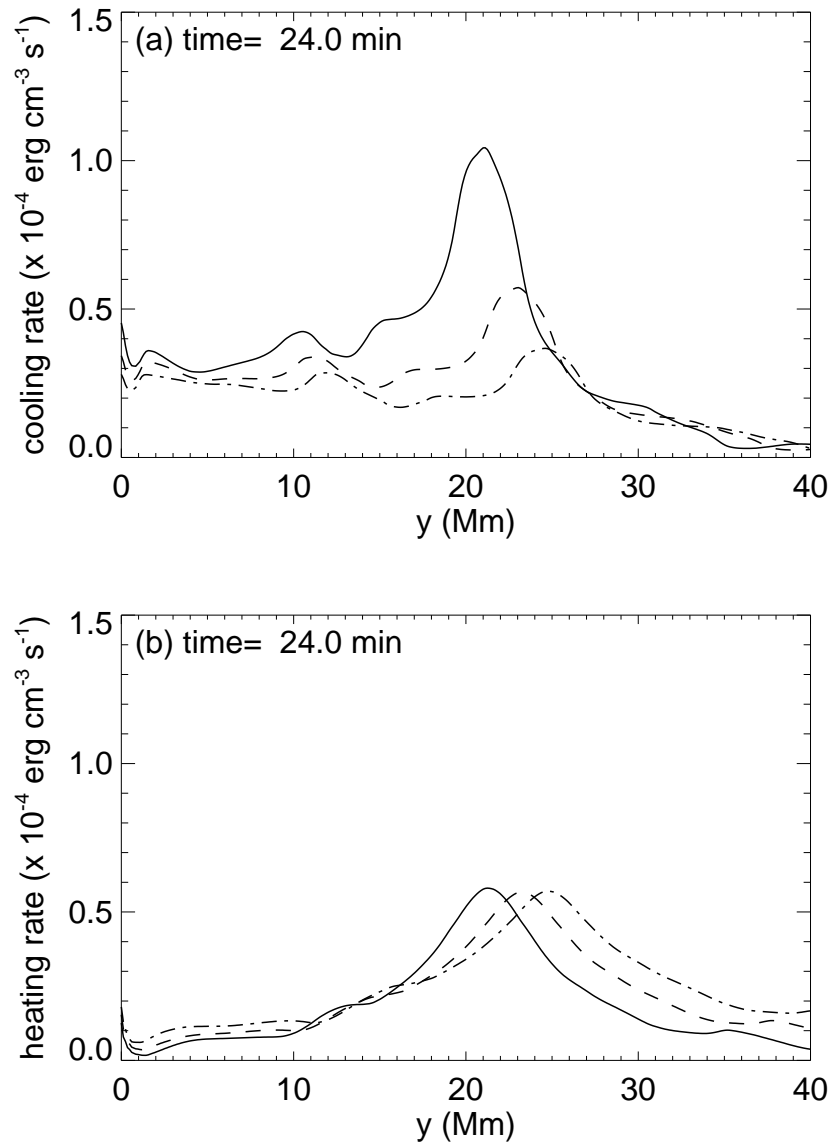


Figure 2.5: Panel (a) and (b) shows cooling rate and heating rate along y -axis at time = 24.0 min. Solid, dashed, and dash-dotted lines represent case M1, M2, and M3, respectively.

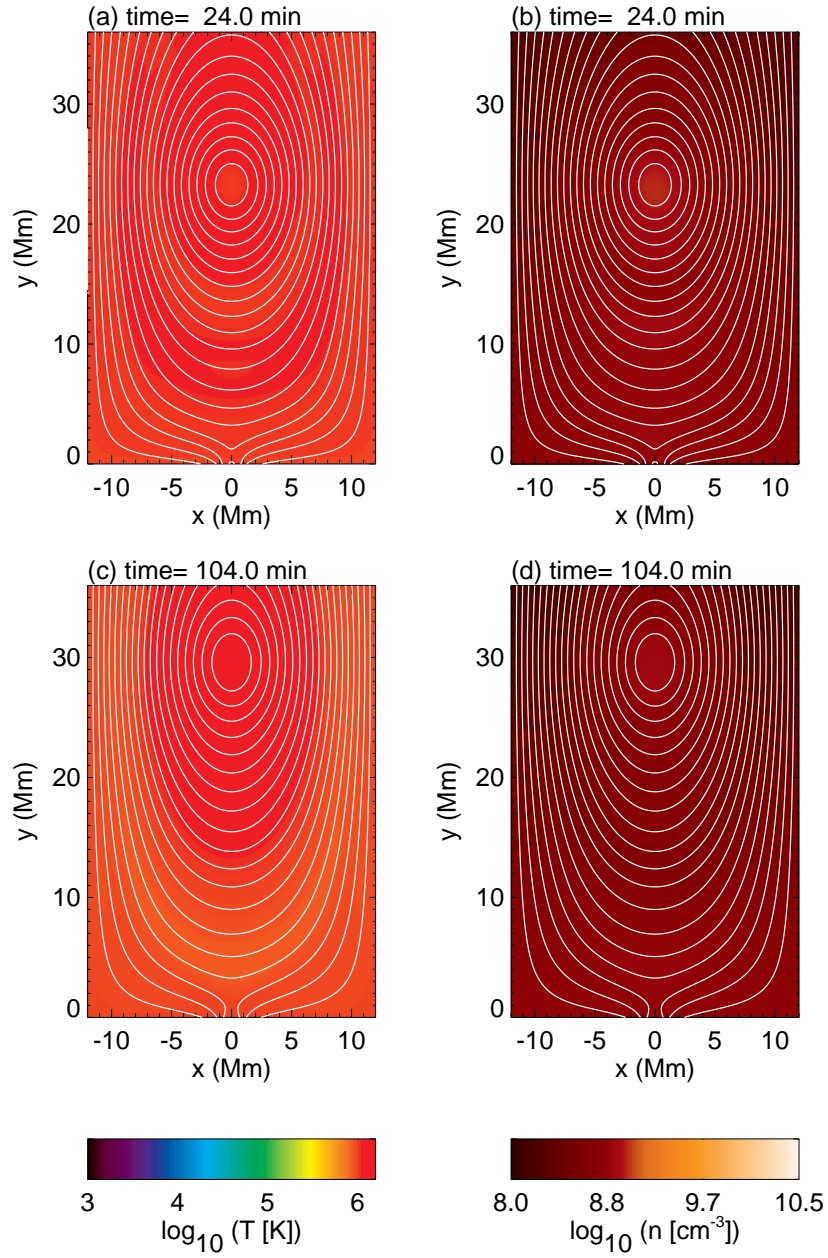


Figure 2.6: Snapshots of time evolution in case M2. Colors and white lines are the same quantities as in Fig. 2.3.

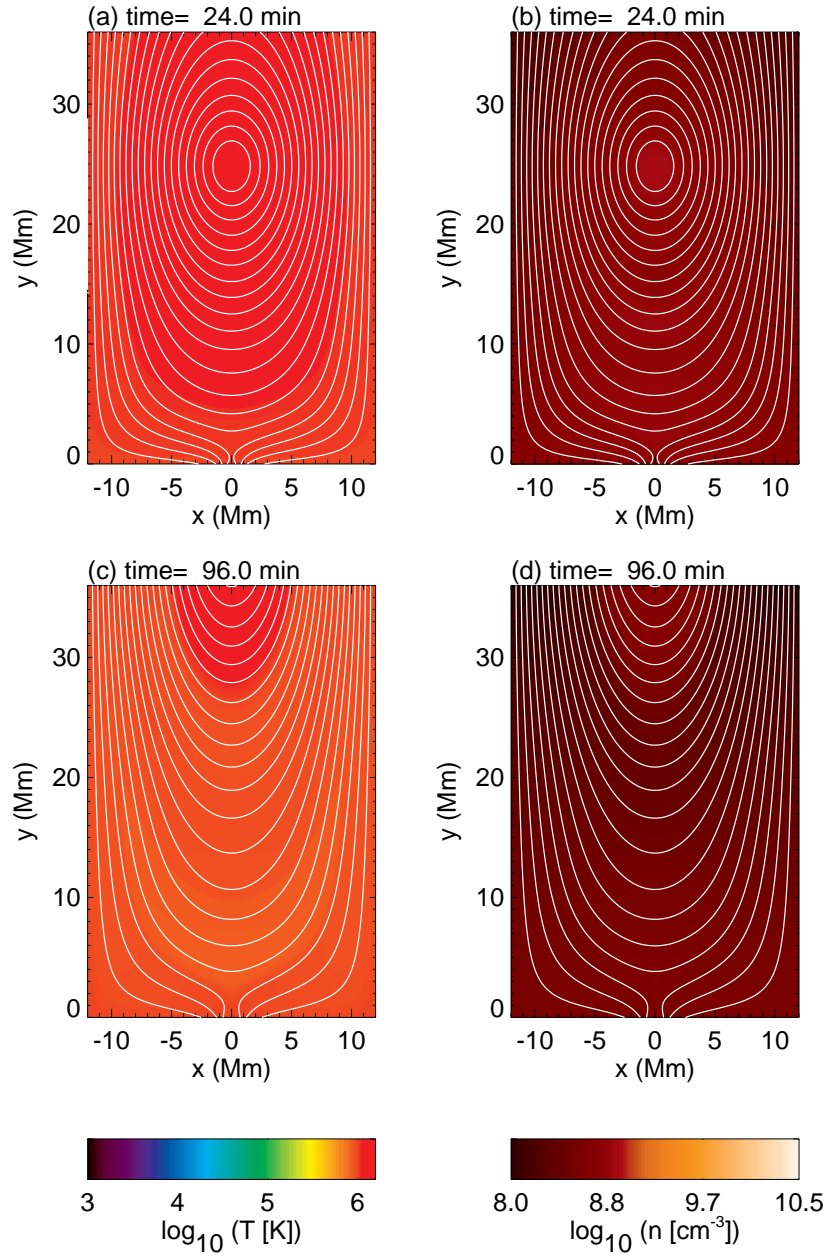


Figure 2.7: Snapshots of time evolution in case M3. Colors and white lines are the same quantities as in Fig. 2.3.

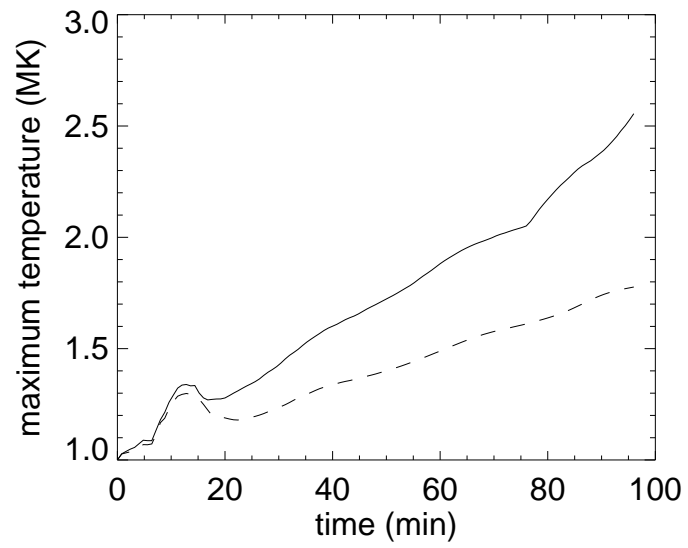


Figure 2.8: Maximum temperature versus time. Solid and dashed lines represent case M2 and M3, respectively.

y -axis. The density of prominence in case N1 is lower than that in case M1, and the temperature of prominence in case N1 is higher than that in case M1. In addition, the temperature of cavity in case N1 is lower than that in observations (Habbal et al., 2010). The evolution of case N2 and N3 is the same as in case M2 and M3.

To validate our formation model, we also investigate the cases of lower coronal density or the smaller speed of footpoint motion compared to case M1. Figure 2.11 shows snapshots of the time evolution of case L in which initial coronal density n_{cor} is lower than that in case M1. The process to radiative condensation is the same as in case M1, however, it takes a longer time to start radiative condensation compared to case M1. The solid and dashed lines in Fig. 2.12 shows time evolution of minimum temperature in cases M1 and L, respectively. The cooling time of case L is approximately twice as long as that of case M1, because time scale of radiative cooling is $\tau_{\text{rad}} = k_B T / (n \Lambda(T))$ and the initial coronal density in case L is a half of that in case M1. Figure 2.11 shows snapshots of the time evolution of case S in which the speed of footpoint motion v_{00} is smaller than that in case S. The process to radiative condensation is the same as in case M1. The dash-dotted line in Fig. 2.12 represents time evolution of minimum temperature in case S. The cooling time of case S is the same as that in case M1. The onset time of radiative condensation is slightly different because formation time of a flux rope is longer in case S than that in case M1.

2.3.3 Effect of footpoint motion

The magnitudes of background heating rate are almost the same among the different cases of the footpoint motions (Fig. 2.5 (b)). The increase of radiative cooling is essential to create the cooling-dominant thermal imbalance for radiative condensation. As shown in Fig. 2.5 (a), the radiative cooling rate is strongly affected by the footpoint shear motions.

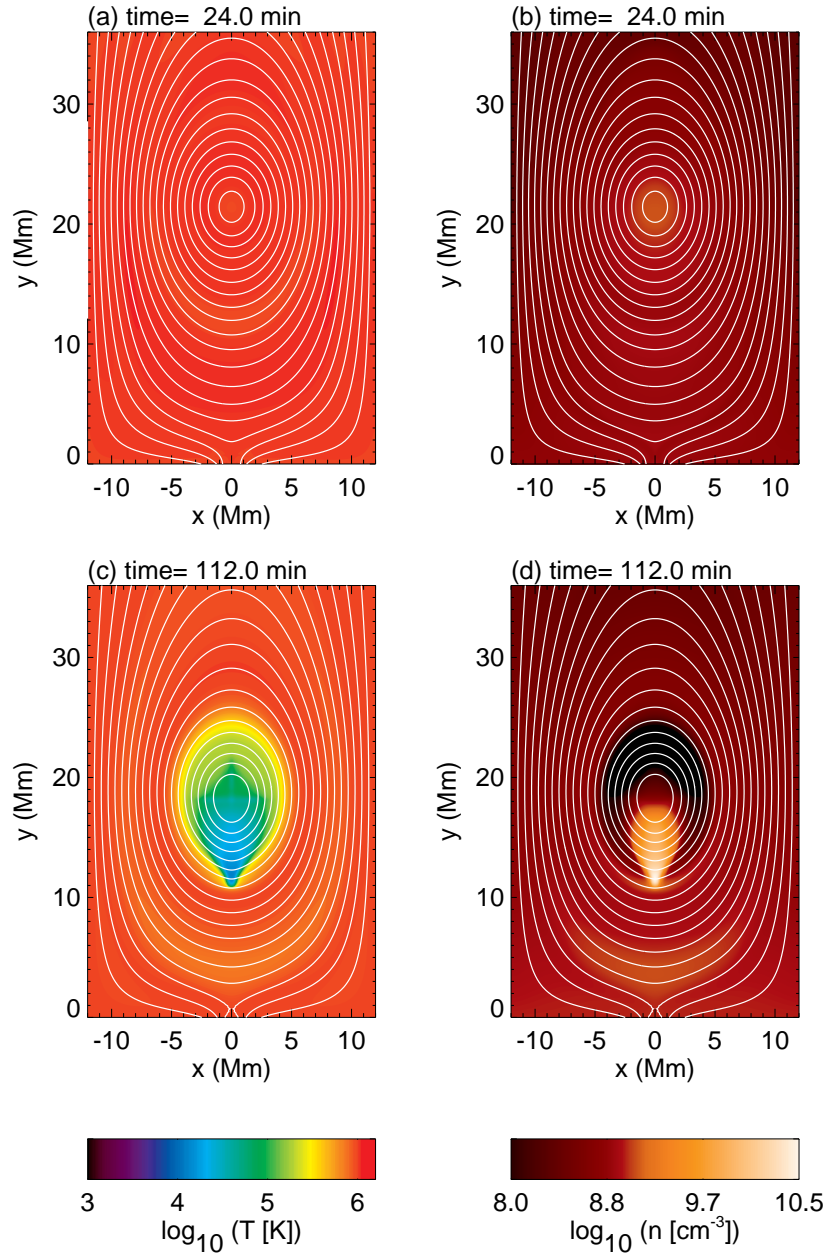


Figure 2.9: Snapshots of time evolution in case N1. Colors and white lines are the same quantities as in Fig. 2.3.

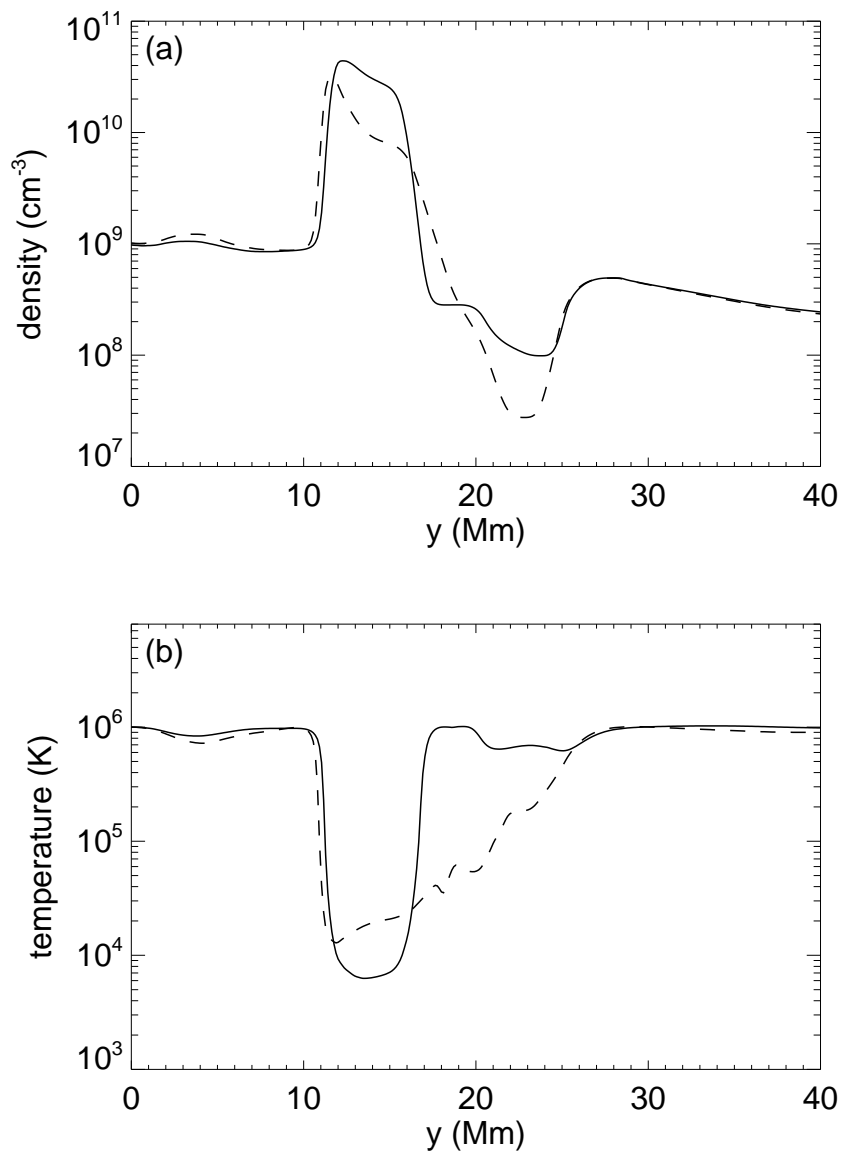


Figure 2.10: Panel (a) and (b) shows density and temperature along y -axis. Solid line represents case M1 at time = 80.0 min, and dashed line represents case N1 at time = 112.0 min. At each time, the prominences in case M1 and N1 locate at the same height.

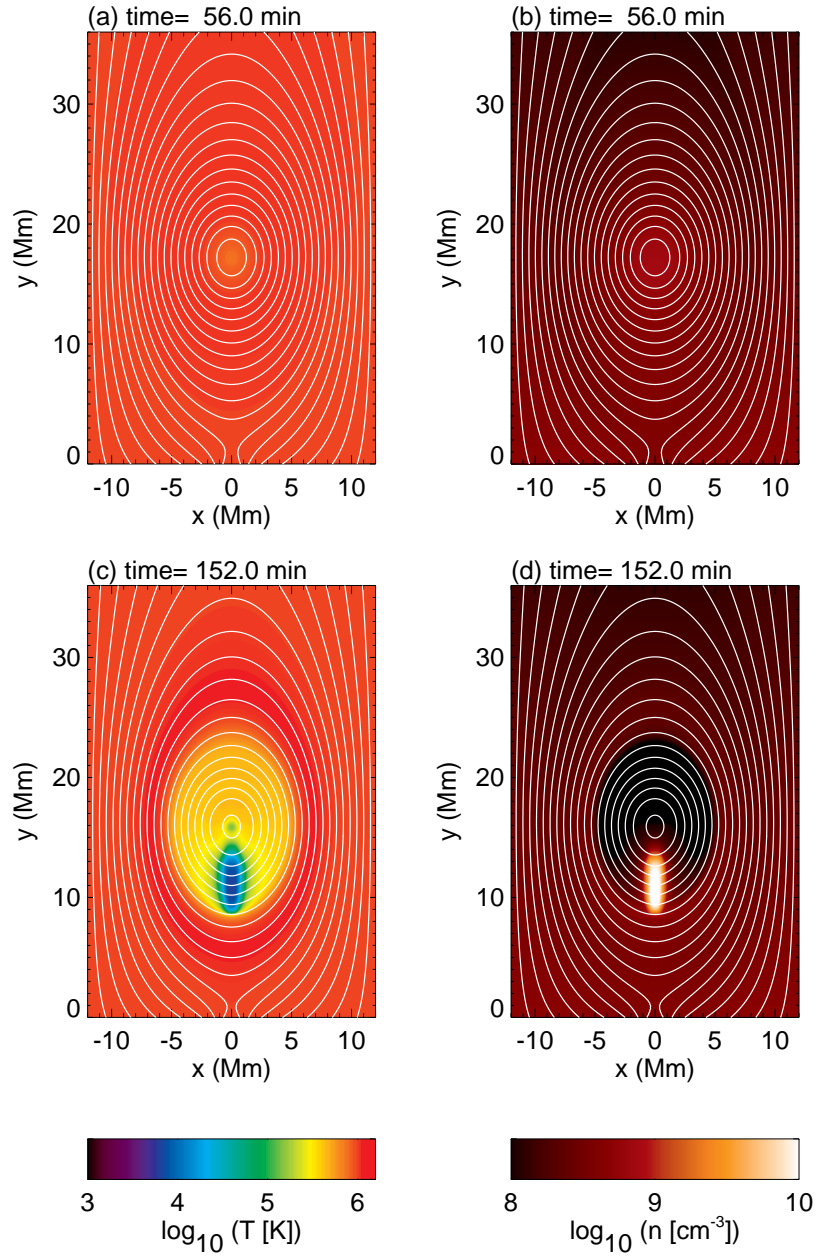


Figure 2.11: Snapshots of time evolution in case L. Colors and white lines are the same quantities as in Fig. 2.3.

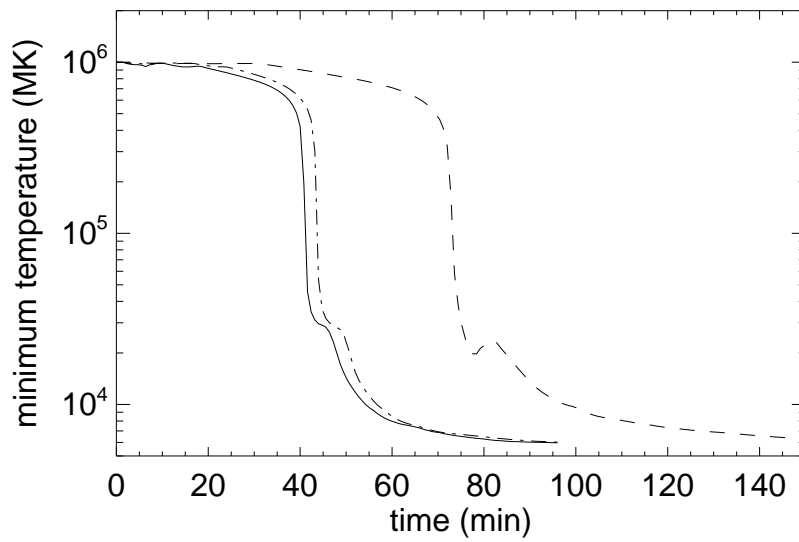


Figure 2.12: Minimum temperature versus time. Solid, dashed, and dash-dotted lines represent case M1, L and S, respectively.

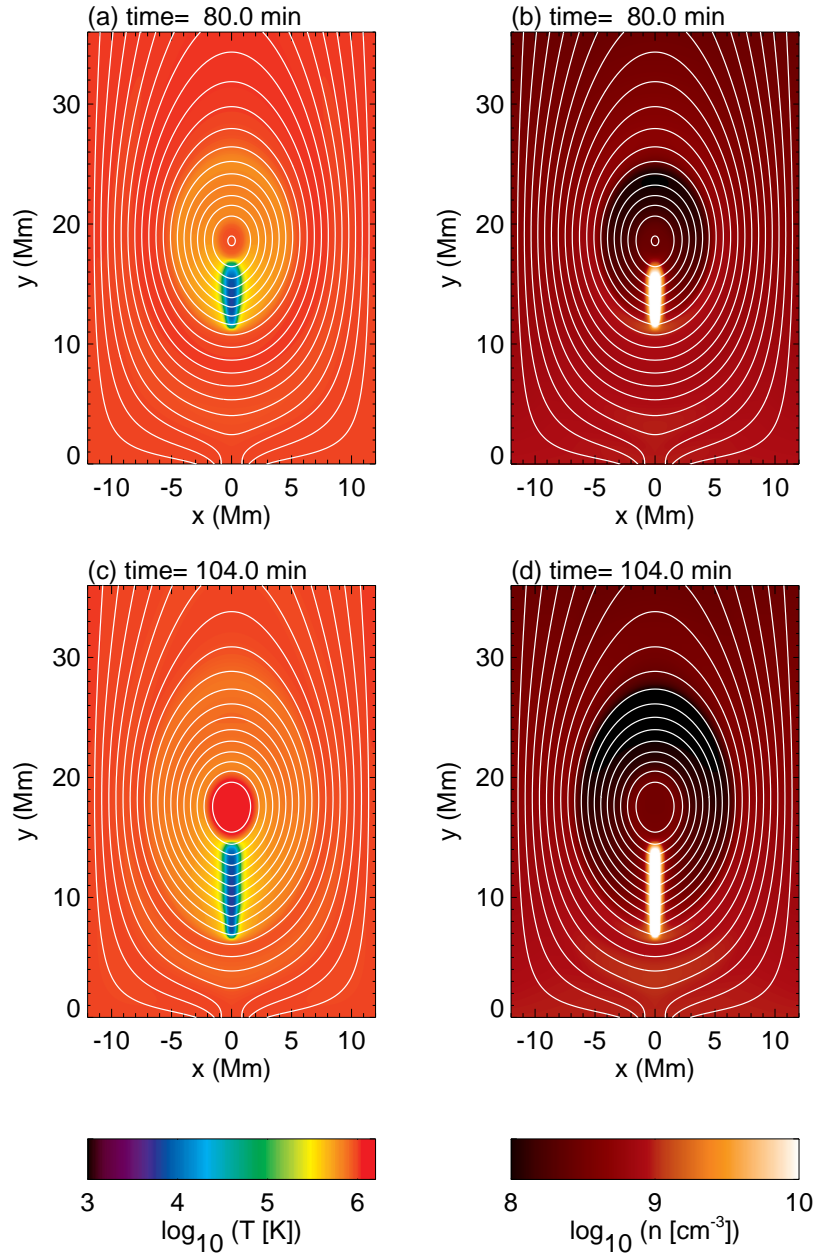


Figure 2.13: Snapshots of time evolution in case S. Colors and white lines are the same quantities as in Fig. 2.3.

The radiative cooling is enhanced by density increase. The density inside the flux rope is increased because the lower half of the flux rope is pushed up by magnetic tension of the reconnected fluxes, whereas the upper half is pressed down by that of the overlying fluxes. Figure 2.14 shows the vertical magnetic tension force along y -axis in each case. The density inside the flux rope in case M1 is larger due to the compression by the strong magnetic tension force. The reason why case M1 has the larger magnetic tension than the other cases is as follows: the shear angle is related to the height of the arcade field as

$$a = \frac{L_a}{\pi \cos \theta}, \quad (2.25)$$

where a is the arcade height, $\theta = \arctan(B_z/B_x)$ is the shear angle against the positive x -axis in xz -plane, L_a is the arcade width, and we assume a linear force-free arcade field for simplicity. Equation (2.25) indicates that the reduction of magnetic shear by anti-shearing motion makes the arcade field shorter. Due to the shrink of the arcade field, the flux rope in the anti-shearing case experiences a larger downward magnetic tension force.

Thus, in the presence of anti-shearing motion, density inside a flux rope is increased by compression of magnetic tension force. The radiative cooling is enhanced by the density increase in the flux rope, resulting in a cooling-dominant thermal imbalance.

2.3.4 Effect of heating model

The properties of prominences are affected by the heating models. As shown in Fig. 2.10 (b), the temperature of prominence in case N1 is higher than that in M1. The cooling rate and heating rate are plotted in Fig. 2.15. As shown in Fig. 2.15 (a) and (b), the profile of cooling rate along y -axis is almost the same, while that of heating rate is different. Because the background heating in case N1 is proportional to density, the heating rate in the prominence ($11 \text{ Mm} < y < 18 \text{ Mm}$) increases as the density of prominence increases. As a result, temperature of prominence in case N1 is higher than that in M1. On the

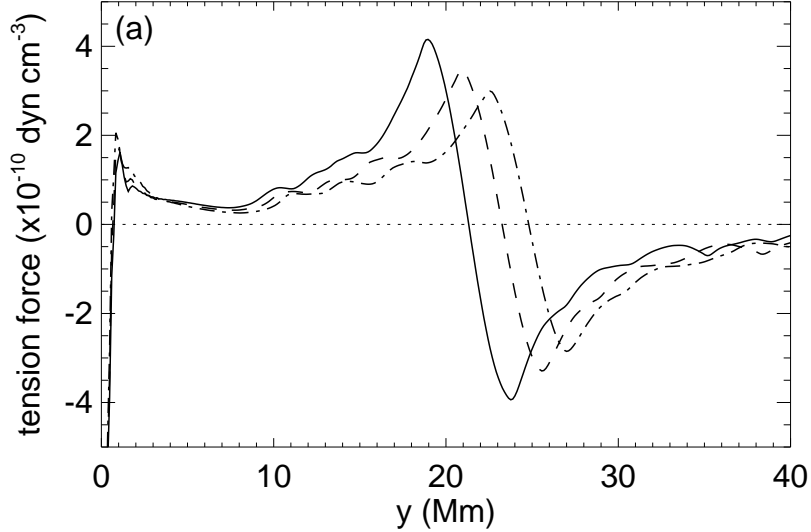


Figure 2.14: Vertical magnetic tension force along y -axis at time = 24.0 min. Solid, dashed, and dash-dotted lines represent case M1, M2, and M3, respectively

other hand, the heating rate in the cavity region ($11 \text{ Mm} < y < 25 \text{ Mm}$) in case N1 decreases as density decreases. Hence, the low temperature cavity is formed in case N1. In observations, the temperature of cavity is the same or higher than that of the ambient corona (Habbal et al., 2010). A heating model proportional to local density is not plausible.

2.4 Three-dimensional simulations

2.4.1 Introduction

The purpose of the study in this section is to validate the reconnection-condensation model with three-dimensionality. In the previous section, we demonstrate the model by

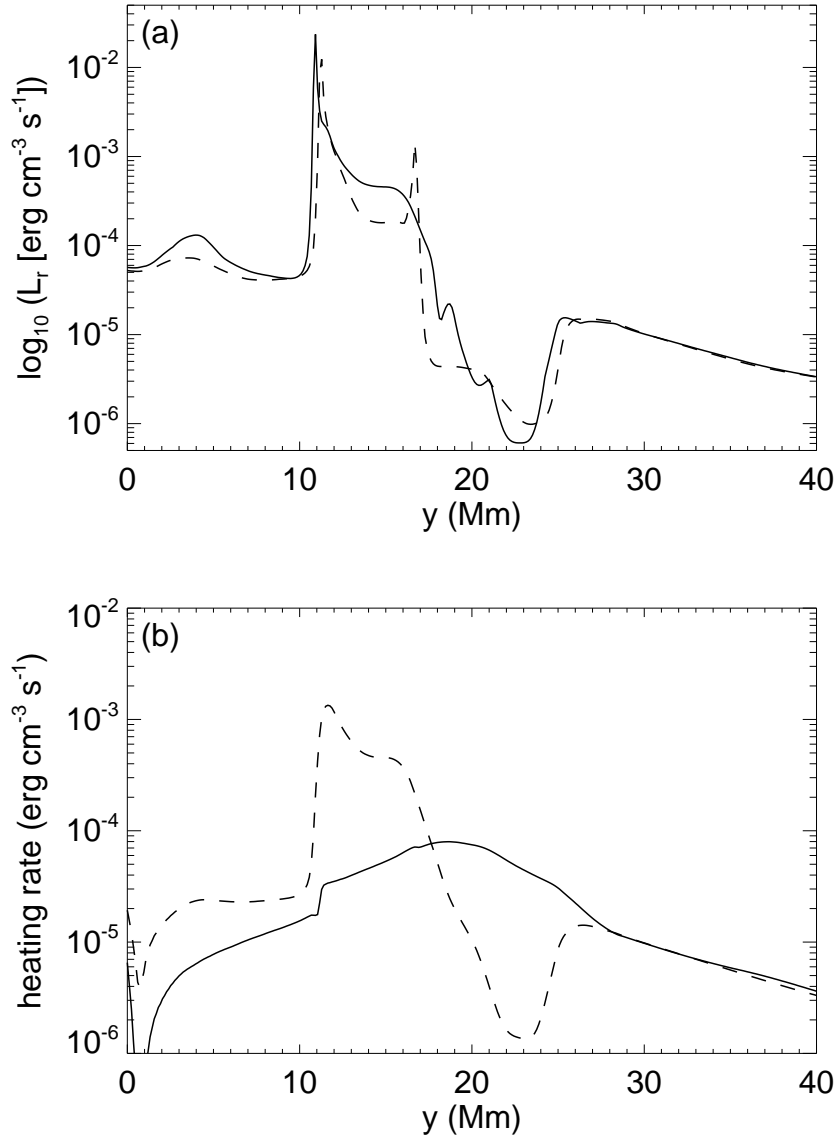
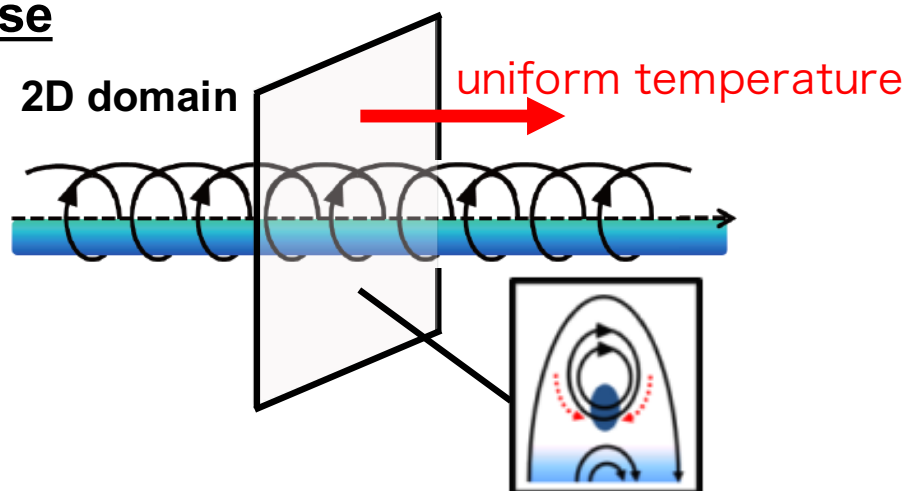


Figure 2.15: Panel (a) and (b) shows cooling rate and heating rate along y -axis. Solid line represents case M1 at time = 80.0 min, and dashed line represents case N1 at time = 112.0 min, corresponding to Fig. 2.10.

two-dimensional simulations. The problem of them is that thermal conduction along toroidal component is neglected because temperature gradient orthogonal to the simulation domain is prohibited by two-dimensional assumption (see Fig. 2.16). In three-dimensional situations, the relaxation by thermal conduction could be more efficient, and there could be a condition for the radiative condensation limited by this effect. To check the validity of the reconnection-condensation model and to obtain such critical condition for prominence formation, we perform three-dimensional MHD simulations including nonlinear anisotropic thermal conduction, optically thin radiative cooling and gravity.

2D case



3D case

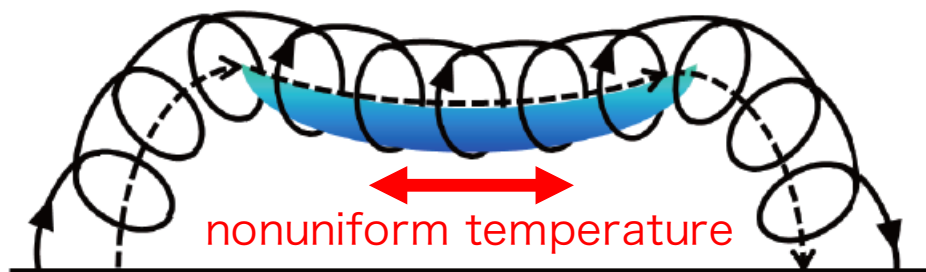


Figure 2.16: Schematic overview of two-dimensional assumption

2.4.2 Numerical Settings

We perform three-dimensional MHD simulation including thermal conduction and optically-thin radiative cooling. The basic equations and numerical scheme is the same as in Section 2.3.

Initial condition

The simulation domain is a rectangular box in Cartesian coordinate (x, y, z) extending in $-12 \text{ Mm} < x < 12 \text{ Mm}$, $-0.4 < y < 40 \text{ Mm}$, and $0 < z < 65 \text{ Mm}$, where y -direction corresponds to height and xz -plane is parallel to a horizontal plane.

The initial corona is under the hydrostatic stratification with a uniform temperature (1 MK) and a uniform gravity (270 m/s^2). The density at $y = 0$ is $1.0 \times 10^9 \text{ cm}^{-3}$, and exponentially decreases with height due to stratification (Eq. (2.2)). The initial magnetic field is a linear force-free arcade given as Eq. (2.5) where $B_a = 6 \text{ G}$, $L_a = 12 \text{ Mm}$, $a = 30 \text{ Mm}$ (see also Fig. 2.17 (a)). The PIL is located at $x = 0$. Three-dimensional MHD equations including nonlinear anisotropic thermal conduction and optically thin radiative cooling are numerically solved. The radiative loss function is the same as that in two-dimensional study (Section 2.3, Fig. 2.2). The background coronal heating proportional to magnetic energy density is set as $H = \alpha_M P_m$ where $\alpha_M = 3.7 \times 10^{-5} \text{ s}^{-1}$ is constant coefficient to achieve the initial thermal equilibrium. The coefficient is determined by Eq. (2.23) where $n_{\text{cor}} = 1.0 \times 10^9 \text{ cm}^{-3}$, $a = k_B T_{\text{cor}} / (m g_{\text{cor}}) = 30 \text{ Mm}$, and $B_a = 6 \text{ G}$.

Boundary condition

To drive the magnetic reconnection at the PIL of the arcade field, the velocities perpendicular and parallel to the PIL given as,

$$v_x = -v_0 \sin\left(\frac{\pi x}{2L_a}\right) \exp\left[-\left(\frac{z}{L_a}\right)^2\right], \quad v_y = 0, \quad v_z = v_x, \quad (2.26)$$

where $v_0 = 6$ km/s, are set in the region below $y = 0$ until $t = 4320$ s. Compared to two-dimensional cases, the region of footpoint motion is localized in z -direction. The magnetic fields below $y = 0$ are computed by the induction equation with these given footpoint velocities. Free boundary condition is applied to the magnetic fields at the bottom boundary. The gas pressure and density below $y = 0$ are assumed to be unchanged in hydrostatic equilibrium at uniform temperature of 1 MK. Free boundary condition is applied to the all variables at the top boundary. Anti-symmetric boundary condition is applied to v_x, v_z, B_x, B_z , and symmetric boundary condition is applied to the other variables at the boundaries in x -direction. We assume symmetry for a rotation of 180 degrees around the y -axis at $(x, z) = 0$ as well as for that around the axis at $(0, 65$ Mm). In the following figures given in this section, plots in the range in -65 Mm $< z < 65$ Mm are shown.

The basic equations and numerical scheme are the same in Section 2.3. The grid spacing size is 120 km everywhere.

2.4.3 Results

Figures 2.17 and 2.18 are the snapshots of simulation result. The initial arcade field (Fig. 2.17 (a)) evolves into a flux rope structure due to reconnection by the footpoint motion (Fig. 2.17 (b)). The flux rope traps dense plasmas at the lower corona, and the radiative cooling inside the flux rope overwhelms the background heating. Due to reconnection,

the length of magnetic loops becomes longer, and the relaxation effect of thermal conduction along the long magnetic loops becomes weaker. The enhanced radiative loss is not fully compensated by the reduced effective thermal conduction along the long reconnected magnetic loops, leading to radiative condensation (Fig. 2.18 (a)). The condensed plasmas are accumulated into the magnetic dips of the flux rope by gravity. Because of the location of the dips, the dense plasmas are concentrated above the PIL to form a filament structure as seen in the top view (Fig. 2.18 (b)). The averaged density and the volume of our simulated prominence is $2 \times 10^{10} \text{ cm}^{-3}$ and $8 \times 10^{26} \text{ cm}^3$, respectively. This results is consistent with the observed lower limit typical prominence densities and volumes (Labrosse et al., 2010).

2.4.4 Critical condition

The relationship between the length and the minimum temperature in each of the individual magnetic field lines is shown in Fig. 2.19. At the initial state, temperature is uniform at 10^6 K (black crosses in Fig. 2.19). The loop length becomes roughly double after reconnection (time = 3120 s, red triangles), and the longer loops suffer from radiative condensation (time = 7200 s, blue squares).

The critical length for radiative condensation can be explained by the Field length (Field, 1965, see also Section 1.6.1) given as,

$$\lambda_F(T, n) \approx \sqrt{\frac{\kappa T^{7/2}}{n^2 \Lambda(T)}}, \quad (2.27)$$

where κ is coefficient of conduction tensor, n is number density, and $\Lambda(T)$ is radiative loss function against temperature. The solid and dashed lines in Fig. 2.19 represent the Field length $\lambda_F(T, n_t)$ and $\lambda_F(T, n_b)$, where $n_t = 5.0 \times 10^8 \text{ cm}^{-3}$ and $n_b = 1.0 \times 10^9 \text{ cm}^{-3}$ are, respectively, the density around the top of the tallest arcades subject to reconnection, and

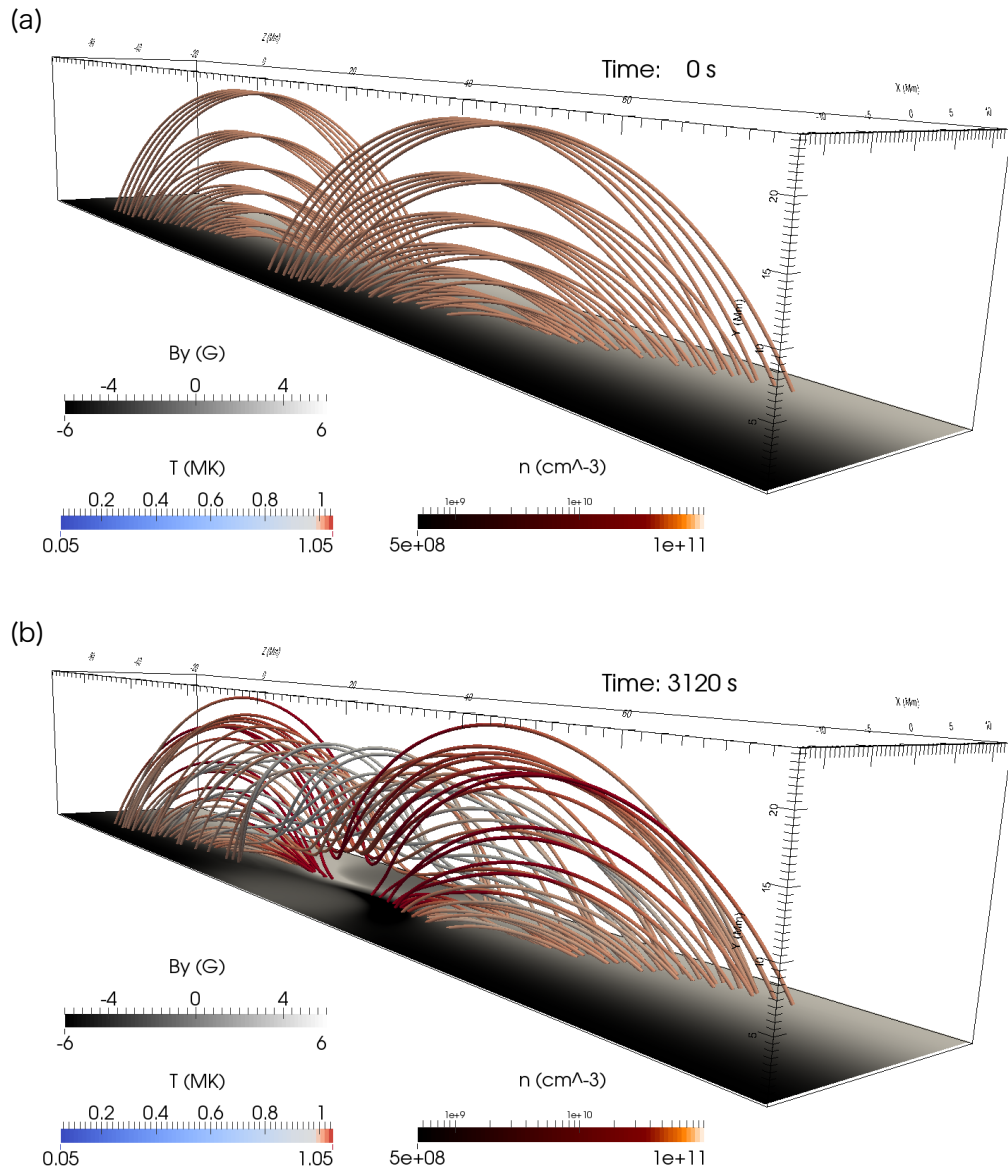


Figure 2.17: Simulation result of model A. Panel (a) is initial condition. Panel (b) is after the formation of flux rope. The lines are magnetic field and the color on them represent temperatures. The grayscale at the bottom boundary represents the signed strength of magnetic field perpendicular to the surface.

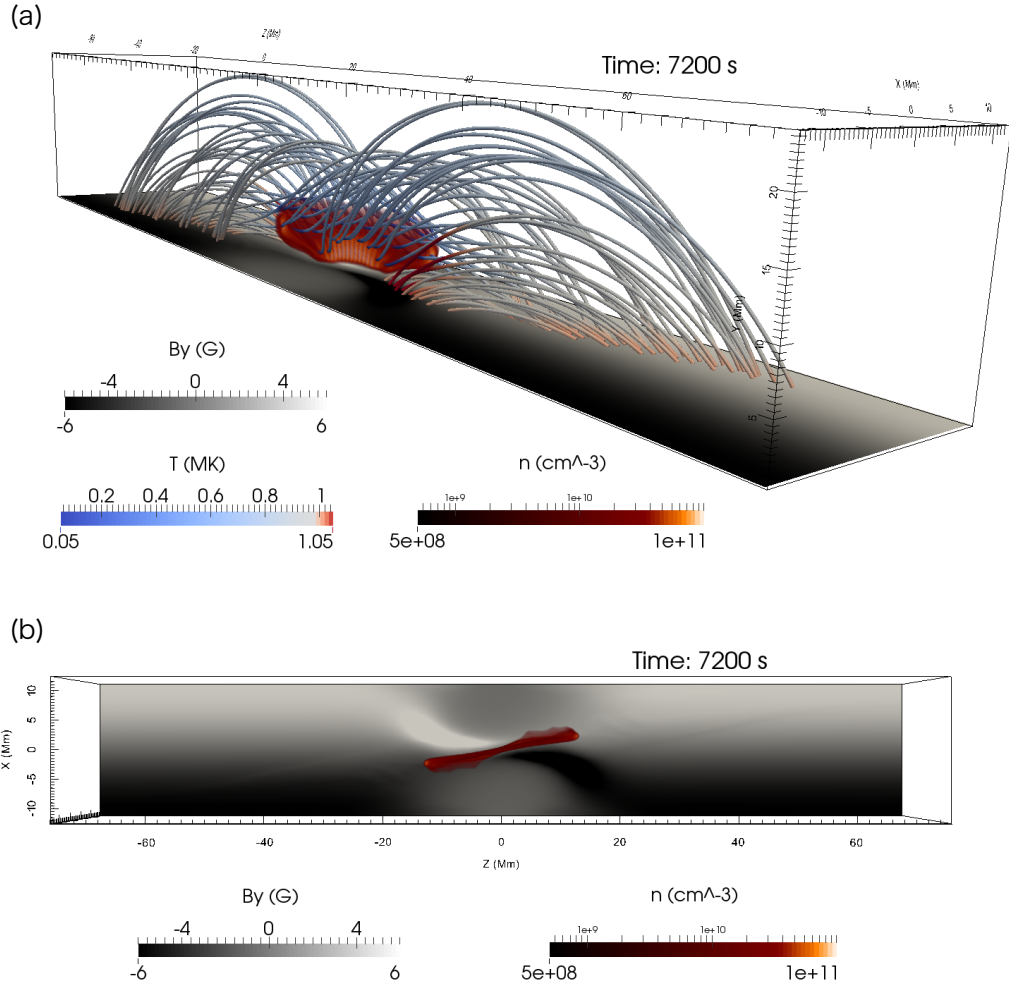


Figure 2.18: Simulation result after radiative condensation is triggered. Panel (a) is the side view with magnetic field lines, and panel (b) is the top view without magnetic field lines. The area of high density ($n > 4.0 \times 10^9 \text{ cm}^{-3}$) is shown by volume rendering. The lines, colors, and grayscale represent the same in Fig. 2.17.

at the bottom boundary. The Field length can roughly explain the condition of radiative condensation in our simulation result.

2.4.5 Comparison with observation

We compare the process of in situ condensation in our simulation results with the observation by Berger et al. (2012) by synthesized emission through the EUV filters of SDO/AIA. The emission of a certain wavelength channel i is expressed as

$$D_i = \int n_e^2 K_i(T) dl, \quad (2.28)$$

where D_i , n_e , $K_i(T)$, and l represent the photon flux, electron number density, temperature response function of AIA filters shown in Fig. 2.20, and distance along the line of site (LOS), respectively. The temperature response functions are obtained from `aia_get_response.pro` in the Solar Software Library (Boerner et al., 2012).

Figure 2.21 shows the synthesized EUV emissions through the filters of SDO/AIA. The dark cavity surrounding the prominence is formed in the emissions of coronal temperatures (193 Å & 171 Å). The low density cavity is formed as a natural consequence of mass conservation in the process of condensation, since, in our model, all of the prominence mass comes from the surrounding corona. The regions surrounded by the blue surfaces in Fig. 2.22 represent a three-dimensional morphology of cavity in our simulation. We find that the shape of cavity is like a seagull wing because the cavity is formed along sheared coronal magnetic field lines.

Figure 2.23 is time evolution of EUV emissions. During the radiative condensation, the intensity peak shows the temporal shift from 171 Å (coronal temperature) to 304 Å (prominence temperature), which is qualitatively consistent with the observation by Berger et al. (2012) (see Fig. 1.11). Note that 211 Å filter image is not synthesized here because the initial coronal temperature is 1MK in our simulation, and a 131 Å

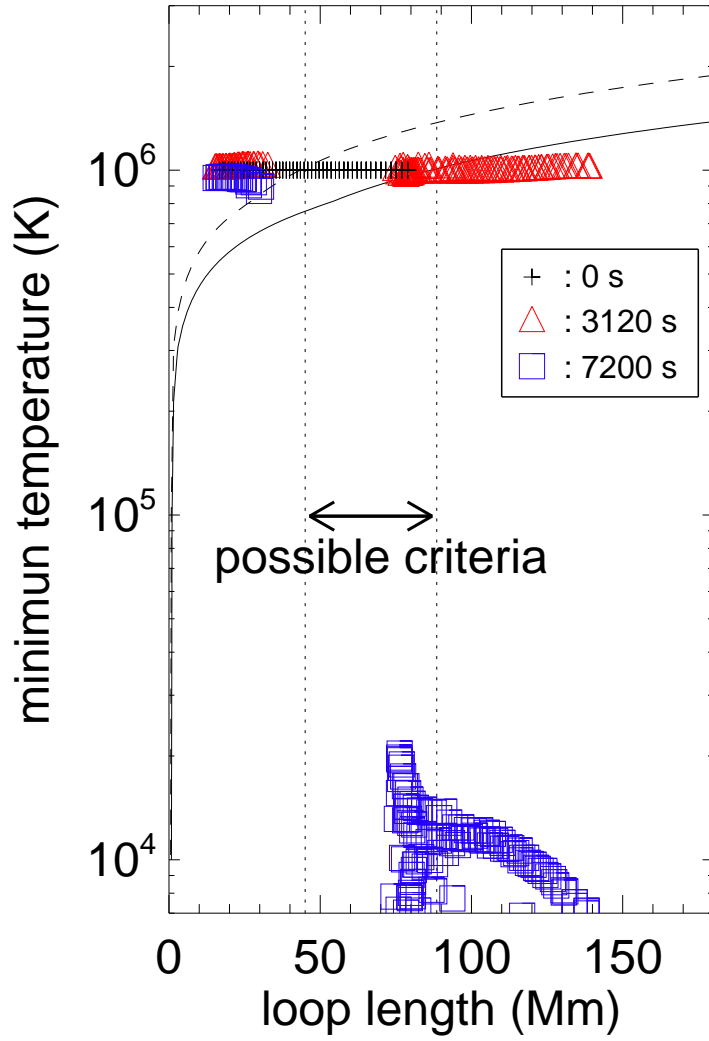


Figure 2.19: Relationship between loop length and minimum temperature of individual magnetic loops at different time. The solid line and dashed line represent $\lambda_F(T, n_t)$ and $\lambda_F(T, n_b)$, respectively. Black crosses, red triangle and blue squares represent the state at the different time shown in the inset.

filtergram is used instead as the signature of transition temperature between corona and prominence. The emission of 193 Å is bright during the reconnection phase ($t = 10 - 20$ min), which reflects the temperature increase from 1MK to 1.2MK inside the flux rope by reconnection heating and density increase by levitation of the lower coronal plasma. In our results, the emissions of coronal temperatures are weak in the height the prominence occupies (after $t = 100$ min in Fig. 2.23). In the observation of Berger et al. (2012), the emissions of 211 Å and 193 Å become dark, while that of 171 Å remains bright even after prominence is formed. This may imply that the prominence interior composes multi-threads and emissions from multiple prominence-corona transition regions are superposed along a line of site. There is also the possibility that the inconsistency between our synthesized emissions and the observed ones is due to the simplified radiative loss function in our simulations.

We also compare differential emission measures (DEM) of our simulation result with observational one. The DEM is computed by the same manner as in Gunár et al. (2011) given as

$$\text{DEM}(T_m) = \sum_i n_{i,m}^2 \frac{\Delta x}{\Delta T_m}, \quad (2.29)$$

where the line of site is in x -direction, Δx is the grid size, $\Delta \log_{10}(T_m) = 0.2$ is a width of temperature bin $\langle T_m, T_m + \Delta T_m \rangle$, and $n_{i,m}$ represents density on i -th grid whose temperature is within $\langle T_m, T_m + \Delta T_m \rangle$. The DEM is averaged in $-12 \text{ Mm} < y < 12 \text{ Mm}$ and $0 < z < 24 \text{ Mm}$. Figure 2.24 shows DEM computed from our simulation results at $t = 7200$ s and an observational DEM (Wiik et al., 1993). The trend of DEM of our simulation results is consistent with the observational one below 10^5 K. Note that the peak at temperature 2.5×10^5 K in the observational DEM is not a common feature for prominences (Parenti & Vial, 2007; Parenti et al., 2012).

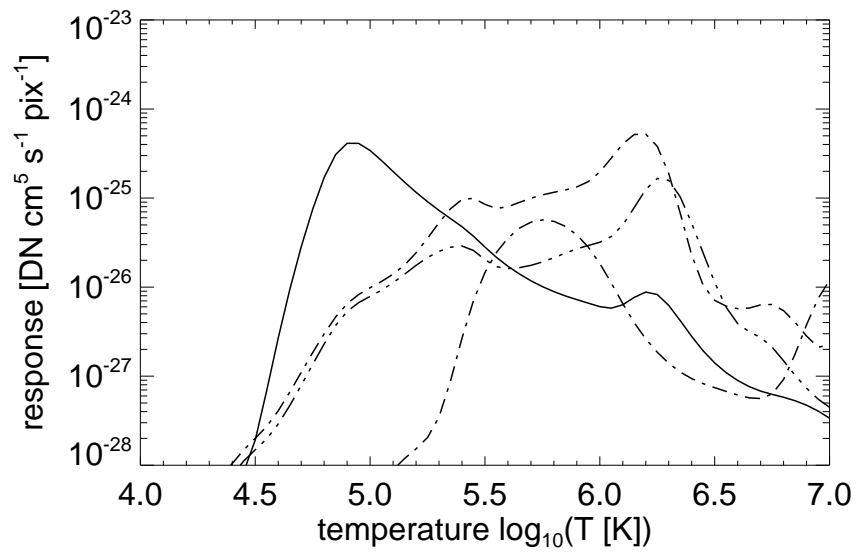


Figure 2.20: Temperature response functions of SDO/AIA filters. Solid, dashed, dot-dashed, three-dot-dashed lines represent response function of 304 Å, 193 Å, 131 Å, 211 Å, respectively (Boerner et al., 2012).

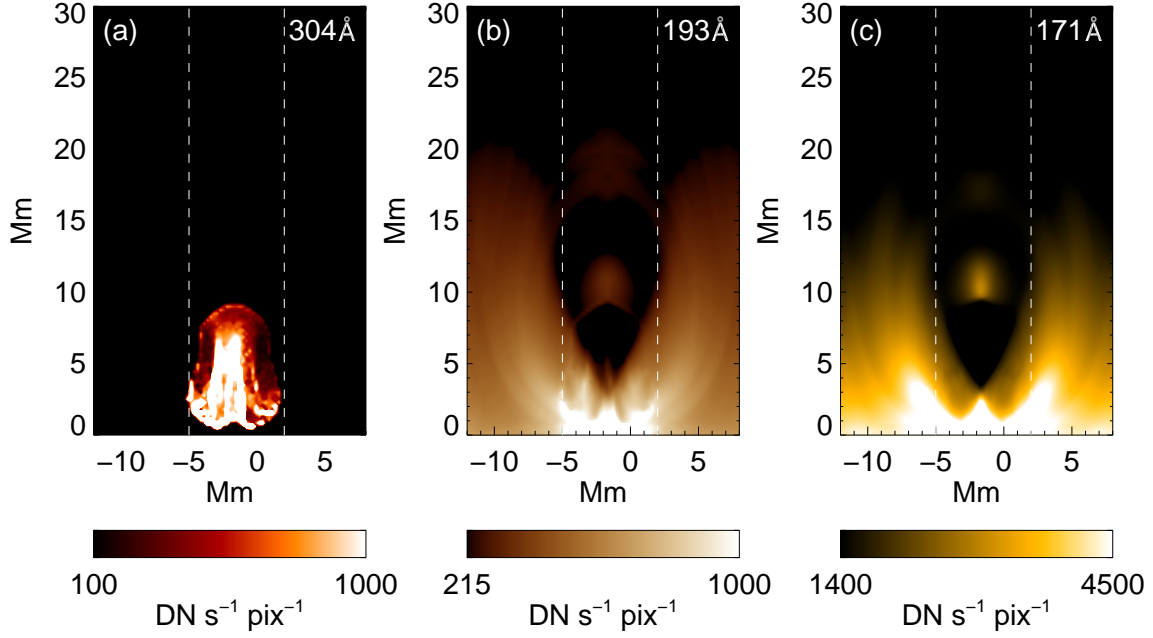


Figure 2.21: Synthesized EUV emission through the AIA filters at time = 7200 s. Panel (a), (b) and (c) represents the image of 304Å, 193Å, and 171Å, respectively. The angle between the line of sight and the z -axis is chosen to be 5 degree for the synthesis.

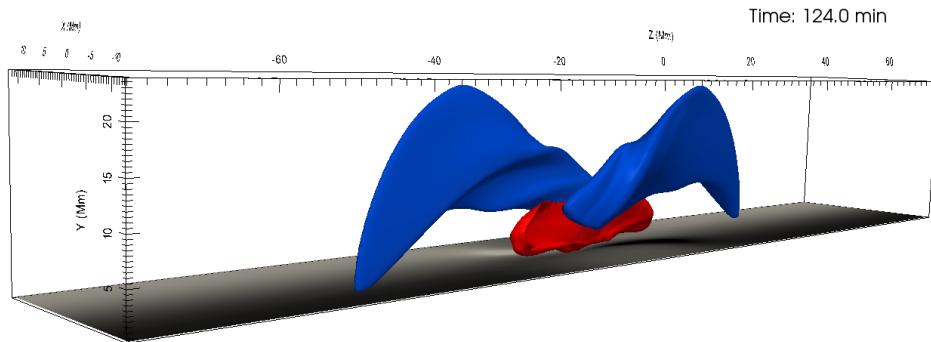


Figure 2.22: Morphology of cavity and prominence. Blue and red contours represent density surfaces of $n = 3.5 \times 10^8 \text{ cm}^{-3}$ and $n = 1.0 \times 10^{10} \text{ cm}^{-3}$, respectively.

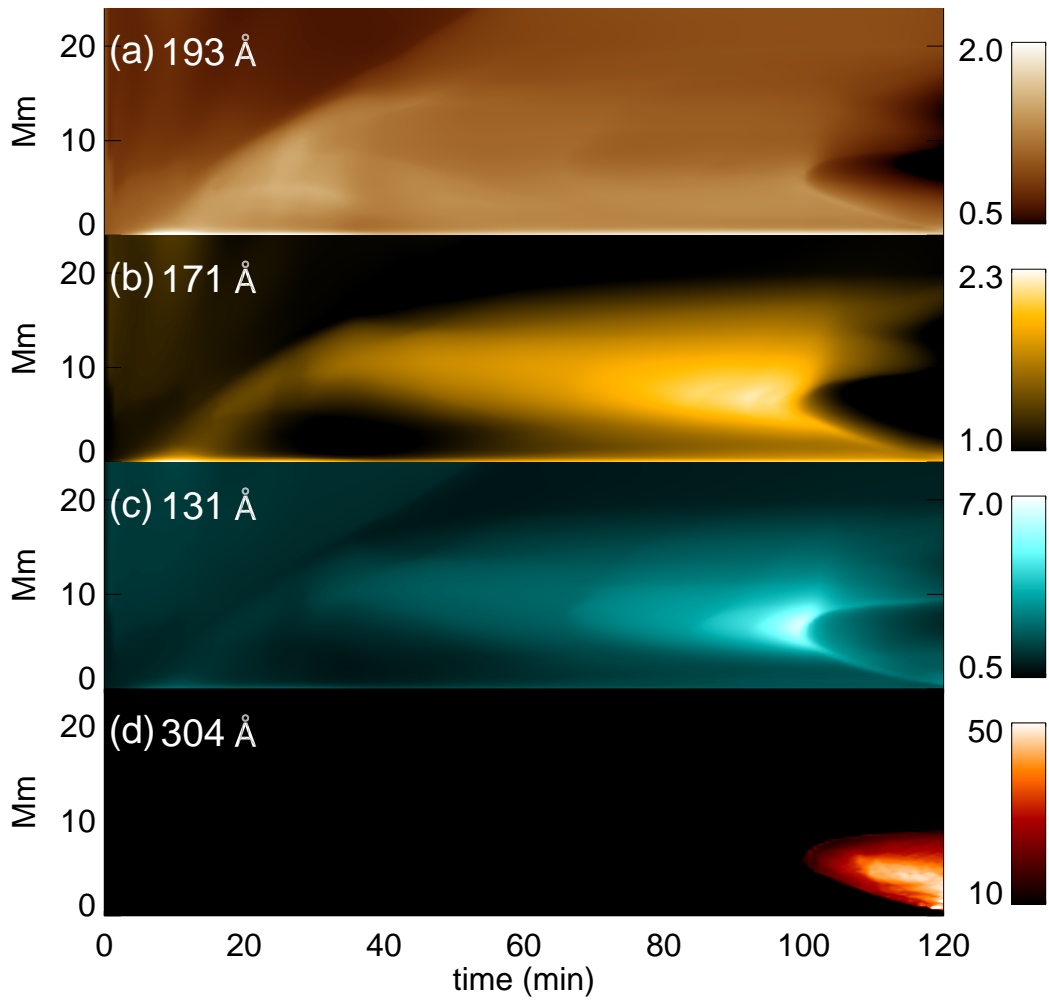


Figure 2.23: Time-height plot of synthesized EUV emission ratios through SDO/AIA filters. The emission inside the white dashed lines in Fig. 2.21 is averaged. Emission at time = 0 s is the reference of ratio for each filter. Panel (a), (b), (c) and (d) represents image of 193 Å, 171 Å, 131 Å and 304 Å, respectively.

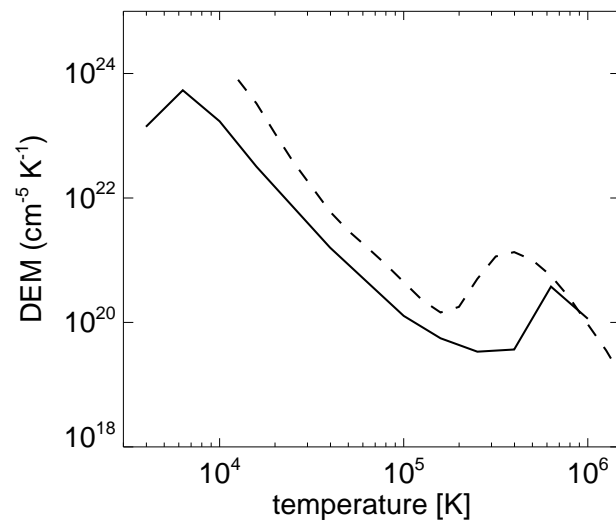


Figure 2.24: DEM obtained from the 3D simulation and observation. Solid and dashed line represents DEM from simulation in the present simulation and the observation by Wiik et al. (1993), respectively

2.4.6 Discussion on three-dimensional simulations

We demonstrated the reconnection-condensation model for solar prominence formation by using three-dimensional MHD simulations including nonlinear anisotropic thermal conduction and optically-thin radiative cooling. In this model, reconnection and the subsequent topological change of magnetic field causes radiative condensation. When the length of the reconnected loops exceeds the Field length, radiative condensation is triggered. The synthesized images of EUV emissions are consistent with the observational findings, i.e., the temporal and spatial emission shift among multiwavelength from coronal temperatures to prominence temperatures and the formation of dark cavity.

To check the dependence on the artificial background heating, we perform an additional simulation with a different type of background heating, $H = \alpha_N n B$, where $\alpha_N = 9.2 \times 10^{-15} \text{ erg}^{-1/2} \text{ cm}^{-3/2} \text{ s}^{-1}$ is set for initial thermal balance. Fig. 2.25 shows the relationship between the length and the minimum temperature in each of the individual magnetic field lines. We found that, even in this heating model, the critical condition of the Field length is valid. The prominence temperature in this heating model is higher than that in the heating model of $H = \alpha_M P_m$ because heating rate in prominence increases with density, as discussed in Section 2.3.4.

In this study, we checked only two heating models. A future work must test more kinds of heating models proposed by the previous studies (Mandrini et al., 2000). The coronal heating was self-consistently solved by MHD simulations based on a wave heating model (e.g. Suzuki & Inutsuka, 2005; Matsumoto & Suzuki, 2012, 2014). A simulation of condensation including self-consistent coronal heating is also one candidate of future works.

Previous studies have proposed a reconnection scenario for the formation of a flux rope sustaining prominence (van Ballegoijen & Martens, 1989; Martens & Zwaan, 2001;

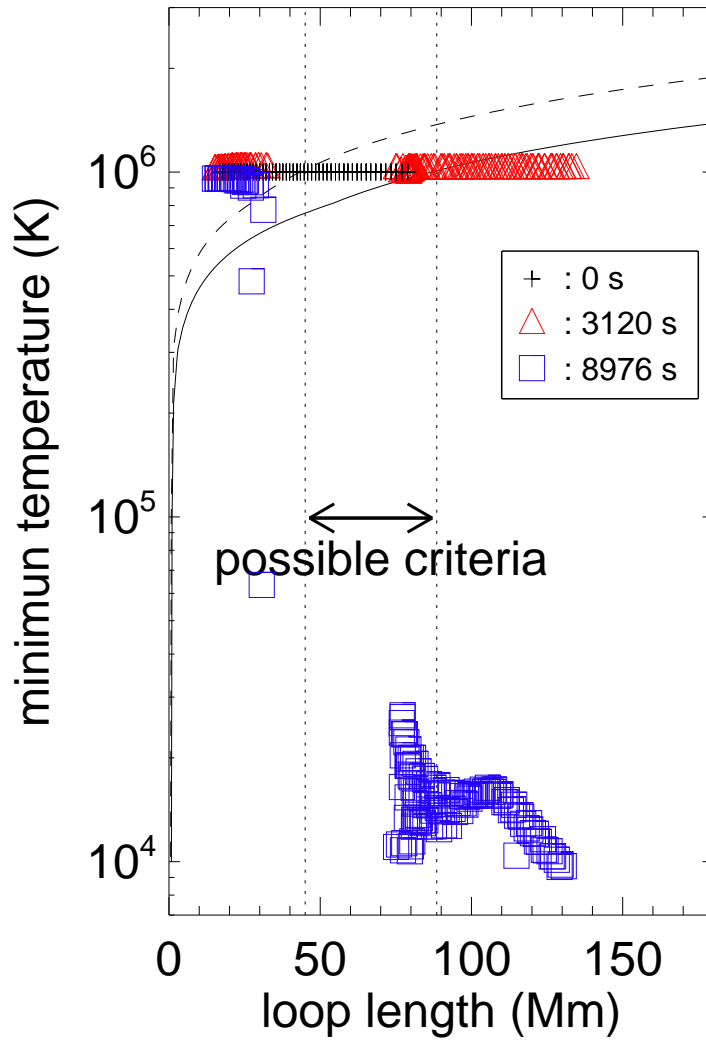


Figure 2.25: Relationship between loop length and minimum temperature of individual magnetic loops in the simulation with heating model $H = \alpha_N n B$. The solid line and dashed line are the same meaning as in Fig. 2.19. Black crosses, red triangle and blue squares represent the state at the different time shown in the inset.

Welsch et al., 2005). The origin of cool dense plasmas has not been explained in this reconnection scenario itself. Our study provides a clear link between reconnection and radiative condensation, and verifies that reconnection leads not only to the flux rope formation but also to the generation of cool dense plasmas of prominence under the condition described by the Field length.

Our model is different from the evaporation-condensation model in how to satisfy the critical condition of thermal instability. The critical conditions in all thermal instability models are based on the Field length, not only in our model. As shown in Xia et al. (2011), evaporation-condensation model also satisfies the criterion of the Field length. In the evaporation model, the length of magnetic field is fixed. The Field length is shortened due to mass supply from evaporation and thermal instability is triggered. In our reconnection-condensation model, the Field length is fixed. Reconnection creates long magnetic field lines. Once the length exceeds the Field length, thermal instability is triggered. Our study points out a new possible process to meet the condition for thermal instability in the magnetized plasma.

The mass of our simulated prominence satisfies only the lower limit of typical prominence mass. The averaged prominence density in our simulation $\sim 10^{10} \text{ cm}^{-3}$ is in the range of typical prominence densities $10^9 - 10^{11} \text{ cm}^{-3}$. The volume of prominence in our simulation is relatively small compared to observational value. To obtain more mass, the construction of longer flux rope by multiple reconnections is one possibility. Since a number of converging points are observed around PIL with mutual interactions of supergranules (Schmieder et al., 2014), multiple reconnection events are plausible. Another possibility is an additional mass supply from chromospheric jets (Chae, 2003) or siphon-like mechanism driven by strong pressure gradient in a condensation (Poland & Mariska, 1986; Choe & Lee, 1992; Karpen et al., 2001; Xia et al., 2011).

The morphology of prominence in our simulation is reverse-S shaped, and chirality of magnetic field is dextral, which is consistent with the observational hemispheric pattern (Martin, 1998b). In observations, barb structures which protrude from one side of a prominence body also have chirality rule: right-bearing barbs in dextral chirality and left-bearing in sinistral chirality. In our simulations, prominences do not have barb structures. Previous theoretical studies claimed that existence of parasitic polarities at footpoints or emergence of bipolar flux is necessary to produce barbs (Aulanier et al., 1998b, 1999; Priest, 1998). Because our simulations do not include such a local bipolar structure in the bottom boundary, barbs are not reproduced. Detailed comparison between observations and numerical simulations on the substructures requires detailed magnetic distributions at the photosphere.

2.5 Summary and Discussion

In this chapter, we proposed a new in-situ formation model of inverse polarity prominence. The model was demonstrated in multi-dimensional MHD simulations, involving thermal conduction and optically thin radiative cooling. Magnetic reconnection by converging and anti-shearing motion is necessary for a prominence formation. A cooling-dominant thermal imbalance inside a flux rope is created from density enhancement by anti-shearing motion. Once the length of a magnetic loop exceeds the Field length, the thermal imbalance can not be compensated by thermal conduction, leading to radiative condensation. In two-dimensional cases, the critical condition described by the Field length is always satisfied because the length of flux rope is assumed to be infinite.

Three-dimensional simulation of the in situ condensation inside the flux rope was also carried out in Xia et al. (2014a). The flux rope system in Xia et al. (2014a) was created by the converging and shearing motion in the isothermal simulation of Xia et al. (2014b).

Because the strategy used to establish cooling-dominant thermal imbalance in Xia et al. (2014a) was the parameterized artificial heating, it was still unclear why the thermal imbalance was created inside the flux rope. We find that the cooling-dominant thermal imbalance can be created inside the flux rope by the anti-shearing motion.

The EUV emissions synthesized from our simulation results reproduced the observed temporal and spatial intensity shift from coronal temperatures to prominence temperatures. We ensure that the emission shift among multiwavelength is the evidence of in situ condensation.

A possible origin of converging and shearing motions is the diverging flows of supergranules crossing a PIL (Rondi et al., 2007; Schmieder et al., 2014). They reported that the mean speed is 0.3 km/s. Since the typical lifetime of supergranules is one day, the migration distance of a magnetic element is approximately 20 Mm. In the present study, we adopt the footpoint motion with the speed of 6 km/s for 4000 s. Because the migration distance is consistent with the observational value, the amount of reconnected fluxes in our simulations is plausible. The time scale of thermal conduction in our simulation is $\tau_{\text{cond}} = nk_B L^2 / (\kappa T^{5/2}) \approx 10^2$ s, where $n = 10^9$ cm⁻³, $T = 10^6$ K and, $L = 20$ Mm. The time scale of radiative cooling is $\tau_{\text{rad}} = k_B T / (n\Lambda) \approx 10^3$ s and that of footpoint motion is $\tau_{\text{foot}} = L/v_{00} \approx 10^3$ s. Because conduction time scale is much faster than that of footpoint motion, perturbations by footpoint motion are immediately relaxed. This situation is not changed even with smaller footpoint speed comparable to the typical supergranular speed. The time scale of footpoint motion is comparable to the radiation time scale in our simulation. In the present simulation results, condensation starts after the flux rope stops rising. In case of a smaller footpoint speed, it is possible that condensation starts during a rise of a flux rope. Note that if we adopt $n = 10^8$ cm⁻³, radiation time scale is 10 times larger and comparable to the supergranular time scale. It is conjectured that

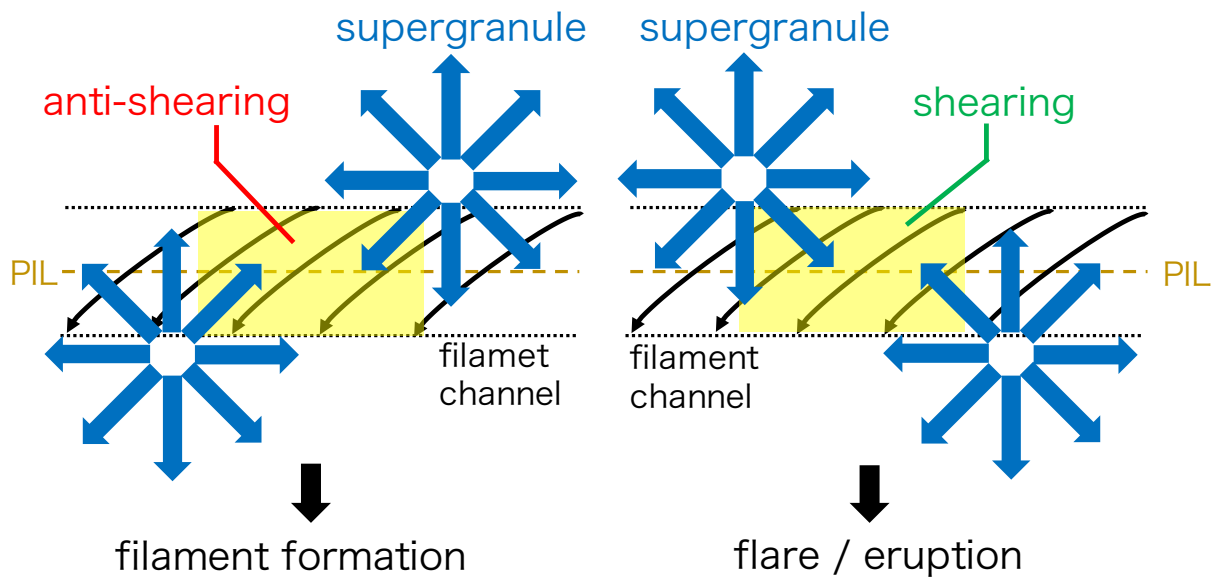


Figure 2.26: Possible relationship between the relative position of supergranules and the direction of footpoint motion.

our simulation results are plausible even with a smaller footpoint speed. We speculate that both anti-shearing motion and shearing motion are created depending on the relative position of supergranules. Figure 2.26 shows the relationship between the relative position and the direction of footpoint motion. In the case of Fig. 2.26 (a), the arcade field of filament channel experienced converging and anti-shearing motion, leading to prominence formation. In the case of Fig. 2.26 (b), the converging and shearing motion leads to flare or eruption.

Chapter 3

Modeling of Prominence Interior Dynamics

3.1 Introduction

The purpose of the study in this chapter is to reproduce dynamic interior of prominences.

In observations at the limb, quiescent prominences are apparently composed of vertical threads (Engvold, 1976; Zirker et al., 1994; Berger et al., 2008; Chae et al., 2008). Typical width of vertical threads is 600 km (Chae, 2010). The vertical upflows and donwflows are also found in the interior of quiescent prominences (Zirker et al., 1998). Recent high-resolution observations by Hinode/SOT found rising dark plumes and descending pillars in prominences (Chae, 2010; Hillier et al., 2012b; Berger et al., 2008, 2010). The vertical threads and flows are not manifestation of vertical magnetic field, because direct measurements of magnetic field based on the Hanle effect indicate that horizontal magnetic field is dominant in a quiescent prominence (Leroy et al., 1983, 1984; Casini et al., 2003; Orozco Suárez et al., 2014). Accordingly, relationship between vertical flows and local magnetic fields are still unclear.

The downflows and upflows are important since they are related to mass budget of prominences. Prominences drain their mass through descending pillars, and obtain mass through rising plumes as well as condensation (Berger et al., 2011; Liu et al., 2012). It was suggested that condensation rate and mass drainage rate were comparable and temporally correlated in an in-situ prominence formation event without rising plumes (Liu et al., 2012) . Despite these efforts, the physical mechanism to drive upflows and downflows, and the physical relationship to condensation process are unclear.

Because heavy plasmas of prominence locate above coronal light plasmas, the Rayleigh-Taylor instability is plausible to explain the upflows and downflows (Ryutova et al., 2010) and is demonstrated by MHD simulations (Hillier et al., 2011, 2012a,b; Keppens et al., 2015; Xia & Keppens, 2016b). In these simulations, Kippenhahn-Schulüter type or straight magnetic field was adopted by taking a local area of flux rope. Terradas et al. (2016) adopted a helical flux rope and found that perturbations were not amplified due to suppression by tension force of the horizontal magnetic field in the flux rope. The relationship to condensation was not discussed because these simulations included neither radiative cooling nor thermal conduction.

Recent three-dimensional MHD simulation including radiative cooling and thermal conduction by Xia & Keppens (2016a) reproduces internal flows with fine threads in evaporation-condensation model. They found that continuous evaporation led to fragmented condensations in a flux rope. The vertical threads and downflows were produced by descending clusters of condensations. They confirmed that the mass of prominence in their simulation was in dynamical equilibrium. The mass maintenance was achieved by mass input from chromospheric evaporation and mass drainage from prominence. The direct influence of the Rayleigh-Taylor instability on radiative condensation is still unclear.

To reveal the mechanism of temporal correlation between mass drainage rate and con-

condensation rate in observational study (Liu et al., 2012), we investigate nonlinear coupling of downflows and radiative condensation numerically. In the earlier part of this thesis in chapter 2, we proposed a new prominence formation model. The simulated prominence did not have vertical threads and flows in its interior. In this chapter, we show that footpoint motion with spatially random speeds leads to the Rayleigh-Taylor instability and formation of vertical threads and internal flows in our reconnection-condensation model. We also discuss the influence of the Rayleigh-Taylor instability on the growth of radiative condensation.

3.2 Numerical settings

The simulation domain is a rectangular box in the Cartesian coordinate (x, y, z) extending in $-12 \text{ Mm} < x < 12 \text{ Mm}$, $0 < y < 50 \text{ Mm}$, and $0 < z < 24 \text{ Mm}$, where y -direction corresponds to height and xz -plane is parallel to horizontal plane. The narrower simulation domain in z -direction than that in Section 2.4 with periodic boundary condition at the boundaries in z -direction is set under the assumption that a flux rope sustaining a prominence is sufficiently long. Basic equations, numerical scheme and initial condition are the same as case M1 in Section 2.3.

In the previous section, we adopted footpoint motions with spatial scale of 24 Mm corresponding to the size of supergranulation. Collisions of multiple supergranules create complex flow patterns along PIL (Rondi et al., 2007; Schmieder et al., 2014), and each supergranular cell contains multiple granular cells with a small spatial scale ($< 1000 \text{ km}$). To investigate the effect of small-scale spatial variation of footpoint motion, we set random speed of footpoint motion along a PIL as follows,

$$v_x = -v_0(t) \sin\left(\frac{\pi x}{2L_a}\right) (1 + \text{RAND}(z_k)), \quad v_y = 0, \quad v_z = v_x \quad (3.1)$$

$$v_0(t) = \begin{cases} v_{00}, & (0 < t < t_1) \\ v_{00} \frac{t_2 - t}{t_2 - t_1}, & (t_1 \leq t \leq t_2) \\ 0, & (t \geq t_2) \end{cases} \quad (3.2)$$

$$v_0(t) = \begin{cases} v_{00} \frac{t_2 - t}{t_2 - t_1}, & (t_1 \leq t \leq t_2) \end{cases} \quad (3.3)$$

$$v_0(t) = \begin{cases} 0, & (t \geq t_2) \end{cases} \quad (3.4)$$

where $v_{00} = 12$ km/s, $\text{RAND}(z_k)$ represents random number at grid point z_k with amplitude of $|\text{RAND}(z_k)| < 0.5$, t represents time, $t_1 = 1200$ s and $t_2 = 1440$ s. Without the random variation in z -direction, this footpoint motion corresponds to that of case M1 in Section 2.3. The magnetic fields below $y = 0$ are computed by the induction equation with these given footpoint velocities. Free boundary condition is applied to the magnetic field at the bottom boundary. The gas pressure and density below $y = 0$ are assumed to be unchanged in hydrostatic equilibrium at uniform temperature of 1 MK. Free boundary condition is applied to all variables at the top boundary. Anti-symmetric boundary condition is applied to v_x, v_z, B_x, B_z , and symmetric boundary condition is applied to the other variables at the boundaries in x -direction. Periodic boundary condition is applied to all variables at the boundaries in z -direction.

3.3 Results

Figure 3.1 shows time evolution of emission measure along x -axis $\text{EM}(y, z) = \int n^2 dx$ in our simulation results. The process to trigger radiative condensation is the same as discussed in Section 2.3. Density of condensation is nonuniform along the PIL due to the random variation of the footpoint speed (Fig. 3.1 (a)). As mass of prominence increases by radiative condensation, multiple spikes appear (Fig. 3.1 (b) and (c)). Thin vertical threads are formed after the spikes touch the bottom boundary (Fig. 3.1 (d)). The width of the threads in our simulation is around 1000 km, which is comparable to that in observations (600 km). Figures 3.2 and 3.3 represent three-dimensional snapshots of the simulation result with different angles. The prominence material locates at dips of the

flux rope. The global magnetic fields maintain a coherent flux rope structure even though local density and velocities evolve in highly nonuniform manner. As shown in Fig. 3.2, the vertical threads are penetrated by horizontal magnetic fields, and they are not the manifestation of vertical magnetic fields.

For comparison, simulation results without random variation of footpoint speed along a PIL are shown in Fig. 3.4. Since, in this case, the setup is translationally symmetric in z -direction, a two-dimensional simulation is carried out and its result is displayed in a three-dimensional manner. Hereafter we call the case with random variation of footpoint speed as case P, and the case without it as case M1.

In order to validate the presence of the Rayleigh-Taylor instability, we investigate gravitational potential energy in these cases. The Rayleigh-Taylor instability leads to a drop of potential energy by exchanging positions of heavy and light plasmas. Radiative condensation also leads to decrease of potential energy because condensed mass goes down to a dip and low density cavity appears in upper half of a flux rope. To distinguish these two effects, we compare the result of case P with that of case M1, while in case M1 only radiative condensation occurs. Figure 3.5 shows time evolution of potential energy in the simulation domain. Compared to case M1, the drop of potential energy in case P becomes larger after $t = 80$ min when the spikes appear. This result indicates the presence of the Rayleigh-Taylor instability.

Figures 3.6 shows velocity field inside the prominence given as

$$V_y^p(y, z) = \frac{\int_{T < 10^5 \text{K}} \rho v_y dx}{\int_{T < 10^5 \text{K}} \rho dx}, \quad (3.5)$$

$$V_z^p(y, z) = \frac{\int_{T < 10^5 \text{K}} \rho v_z dx}{\int_{T < 10^5 \text{K}} \rho dx}. \quad (3.6)$$

Downward flows exist in the spikes. Figure 3.7 shows time evolution of maximum downward speed (panel (a)) and acceleration (panel (b)) in a spike. The downward speed in our simulation is around 12 km/s which is consistent with observational values of

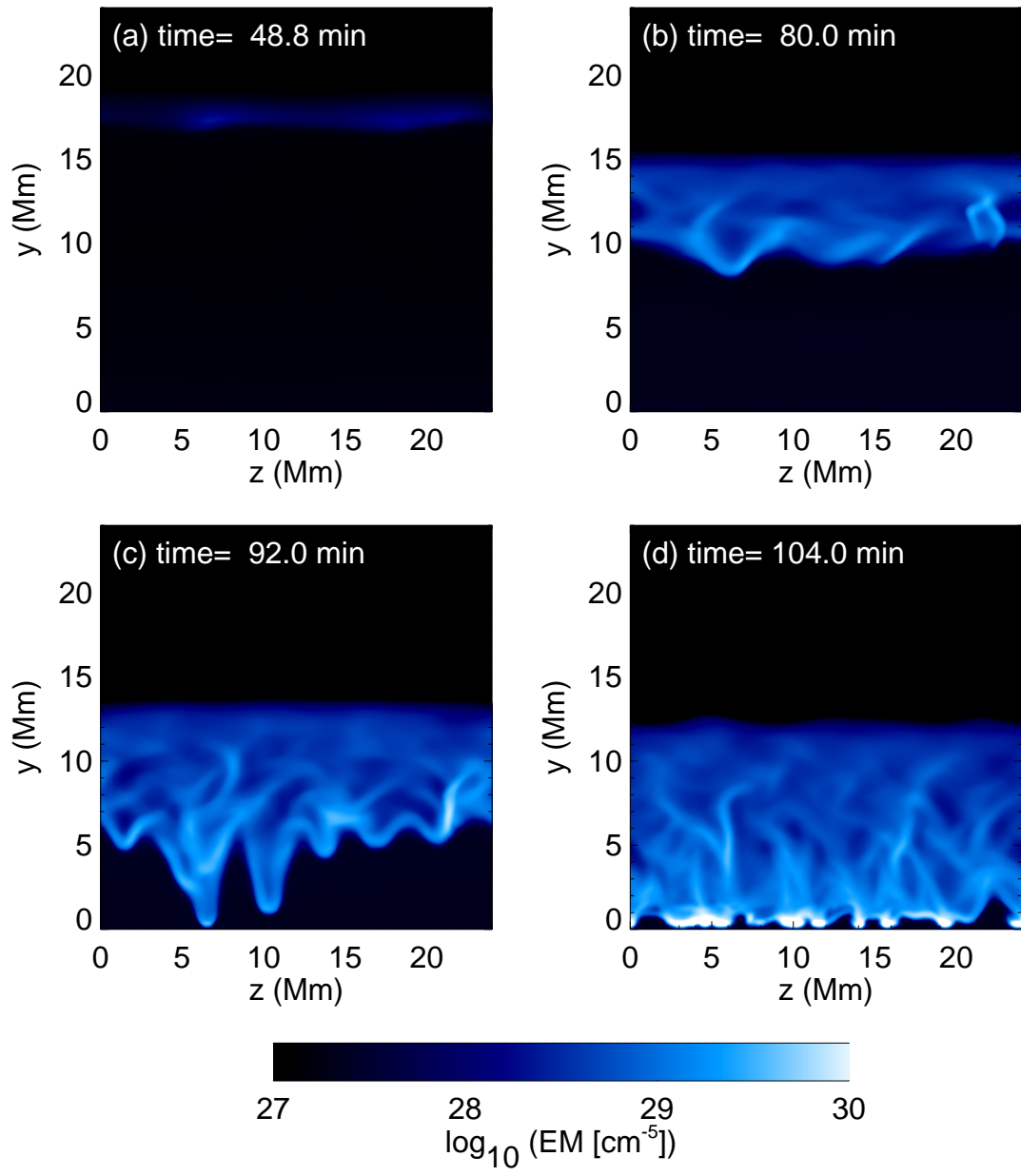


Figure 3.1: Time evolution of emission measure along x -axis.

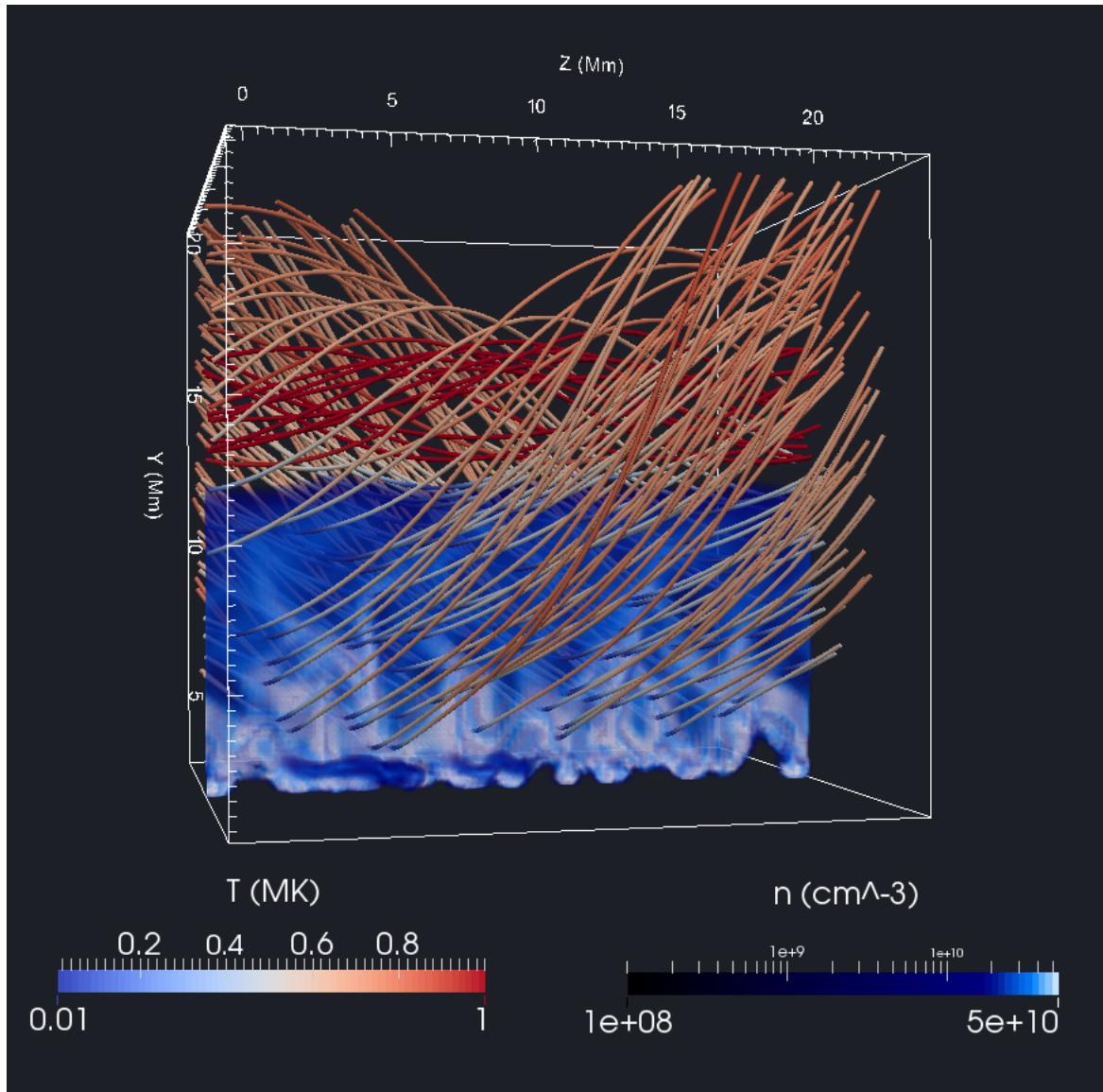


Figure 3.2: Side view of simulation result at $t = 104.4$ min. Density is represented by volume rendering. Lines represent magnetic field lines. Colors on the lines represent temperature.

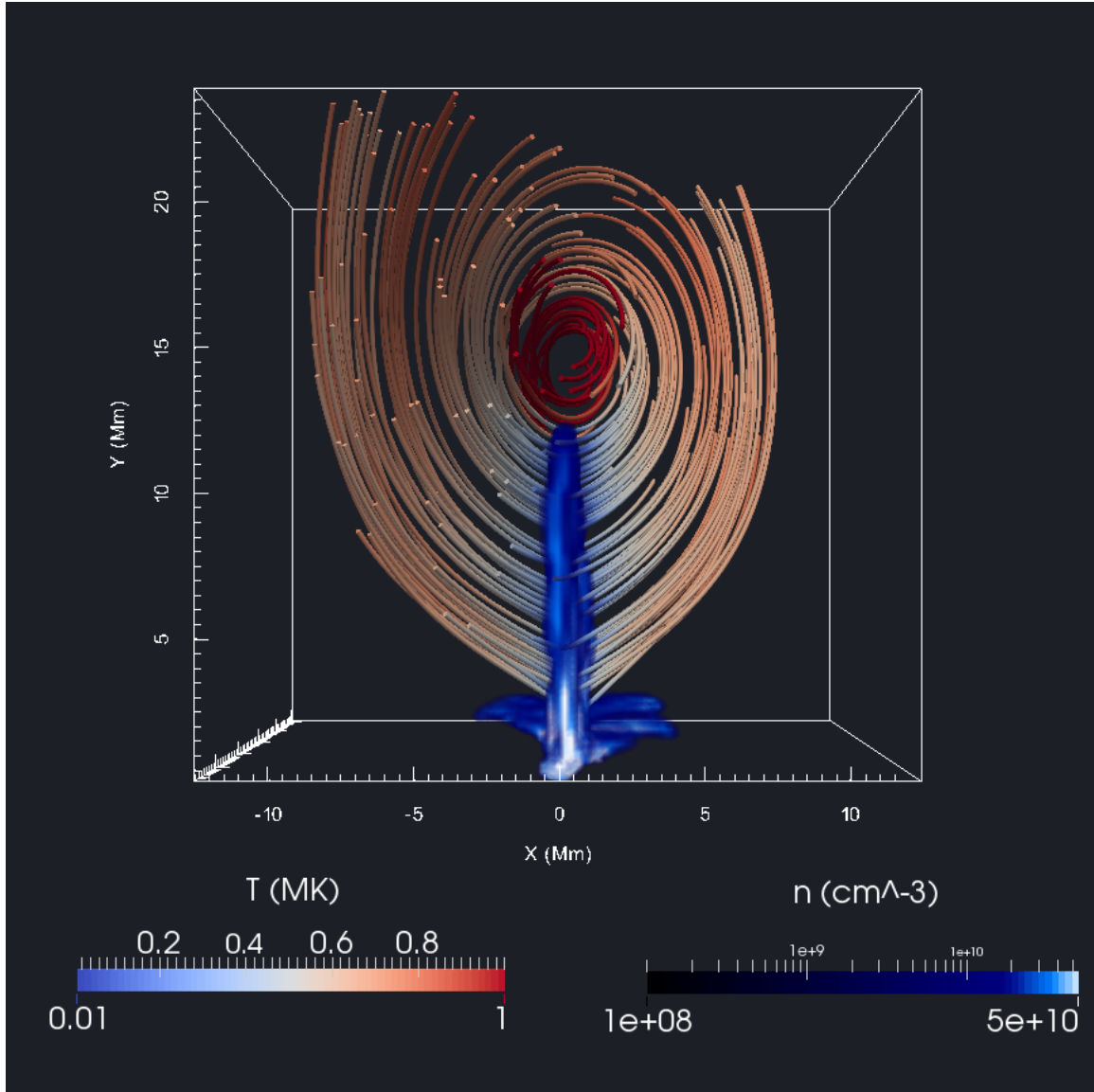


Figure 3.3: Front view of simulation result at $t = 104.4$.

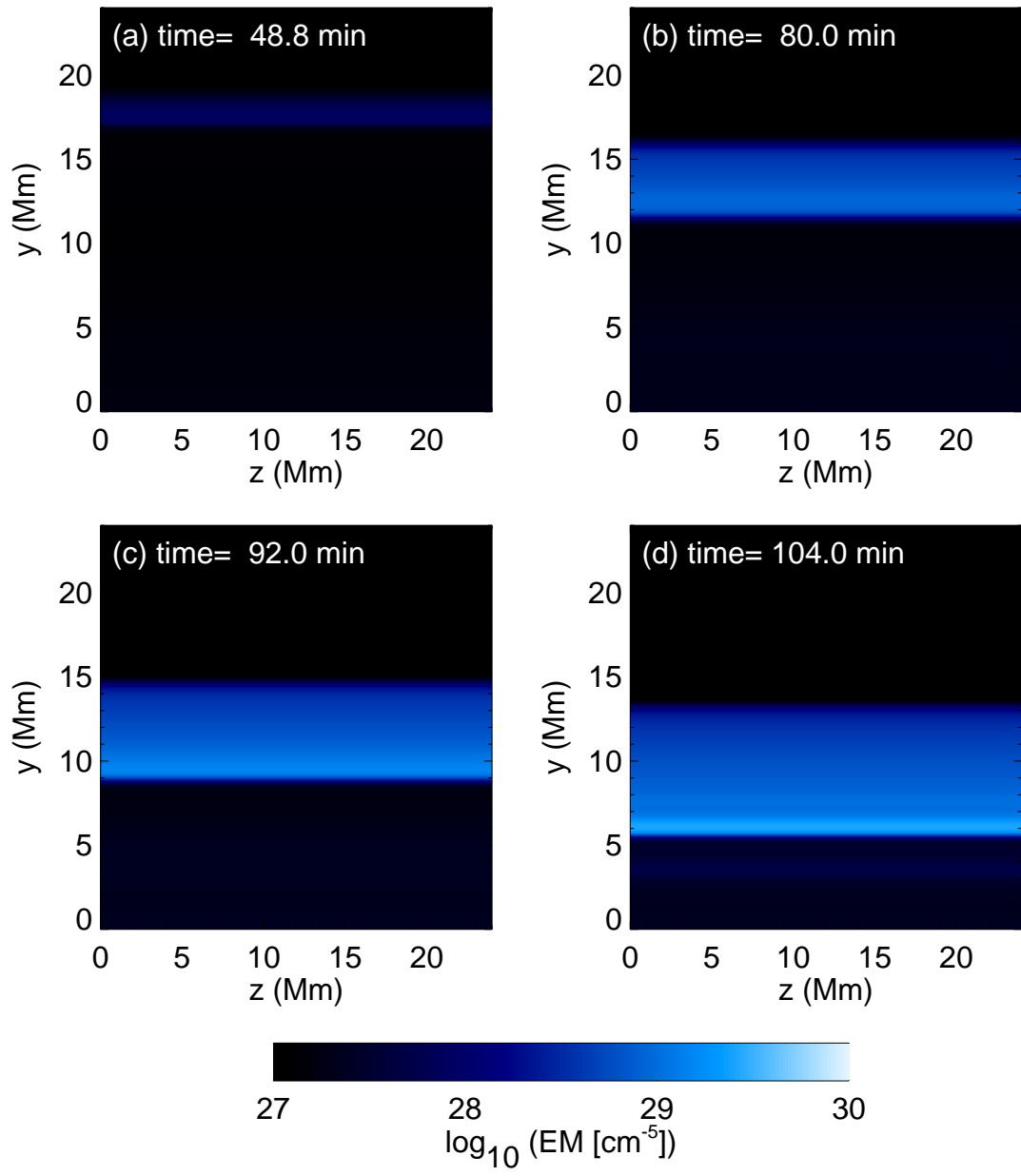


Figure 3.4: Time evolution of emission measure along x -axis without perturbation.

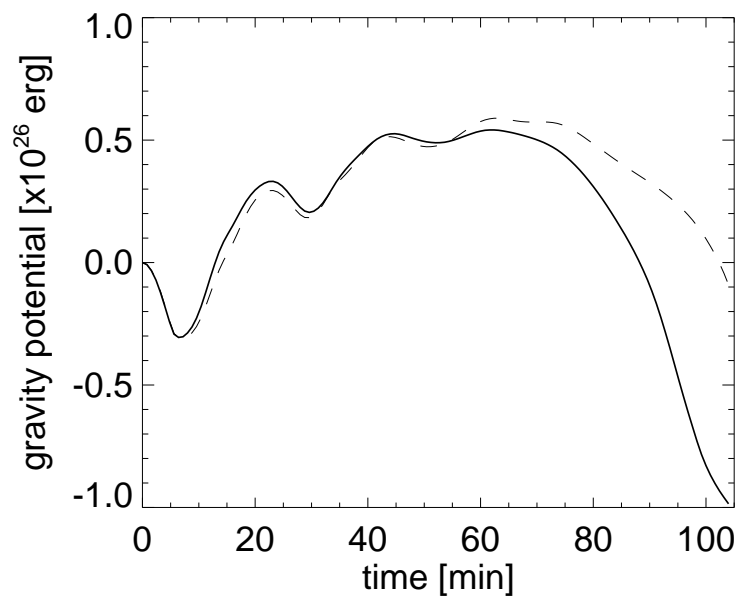


Figure 3.5: Time evolution of gravitational potential energy. Solid and dashed lines represent case P and M1.

10 – 15 km/s (Berger et al., 2008; Chae, 2010; Hillier et al., 2012b). The strongest downward acceleration is -0.02 km s^{-2} , which is much smaller than gravitational acceleration (-0.27 km s^{-2}) and consistent with observational results (Chae, 2010). Figure 3.8 shows forces working on the spike. Downward gravity force is almost canceled by upward magnetic tension force. This force balance in a spike was also reported in a MHD simulation of the Rayleigh-Taylor instability (Hillier et al., 2012b). We conclude that the spikes are produced by the Rayleigh-Taylor instability, while the growth of the spikes are suppressed by upward magnetic tension force of horizontal magnetic field in the flux rope.

After the spikes touch the bottom boundary, vertical threads are formed along the paths of the spikes. Figure 3.9 shows velocity field after the spikes touch the bottom boundary. The descending spikes are reflected at the bottom boundary and create upflows or vortex motions (see around $(y, z) = (4 \text{ Mm}, 5 \text{ Mm})$ in Fig. 3.9). The interaction of flows squeezes the spikes and eventually forms the thin vertical threads.

The observational study by Liu et al. (2012) suggested that condensation rate and mass drainage rate are comparable and temporally correlated. By comparing cases P and M1, we can investigate the influence of mass drainage by the Rayleigh-Taylor instability on radiative condensation. Figure 3.10 shows time evolution of prominence mass (panel (a)) and mass growth rate (panel (b)) in cases P and M1. The mass of prominence is computed as

$$M_{\text{pro}} = \int_{T < 10^5 \text{ K}} \rho(x, y, z) dx dy dz \quad (3.7)$$

and mass growth rate is time derivative of M_{pro} . Until $t = 50 \text{ min}$, mass growth rates are the same between two cases. After $t = 50 \text{ min}$, mass growth rate in case P becomes larger than that in case M1. As shown in Fig. 3.10 (b), growth rate in case P is enhanced after the spikes appear (see also Fig. 3.1 (b)). Figure 3.11 shows mass drainage rate at a

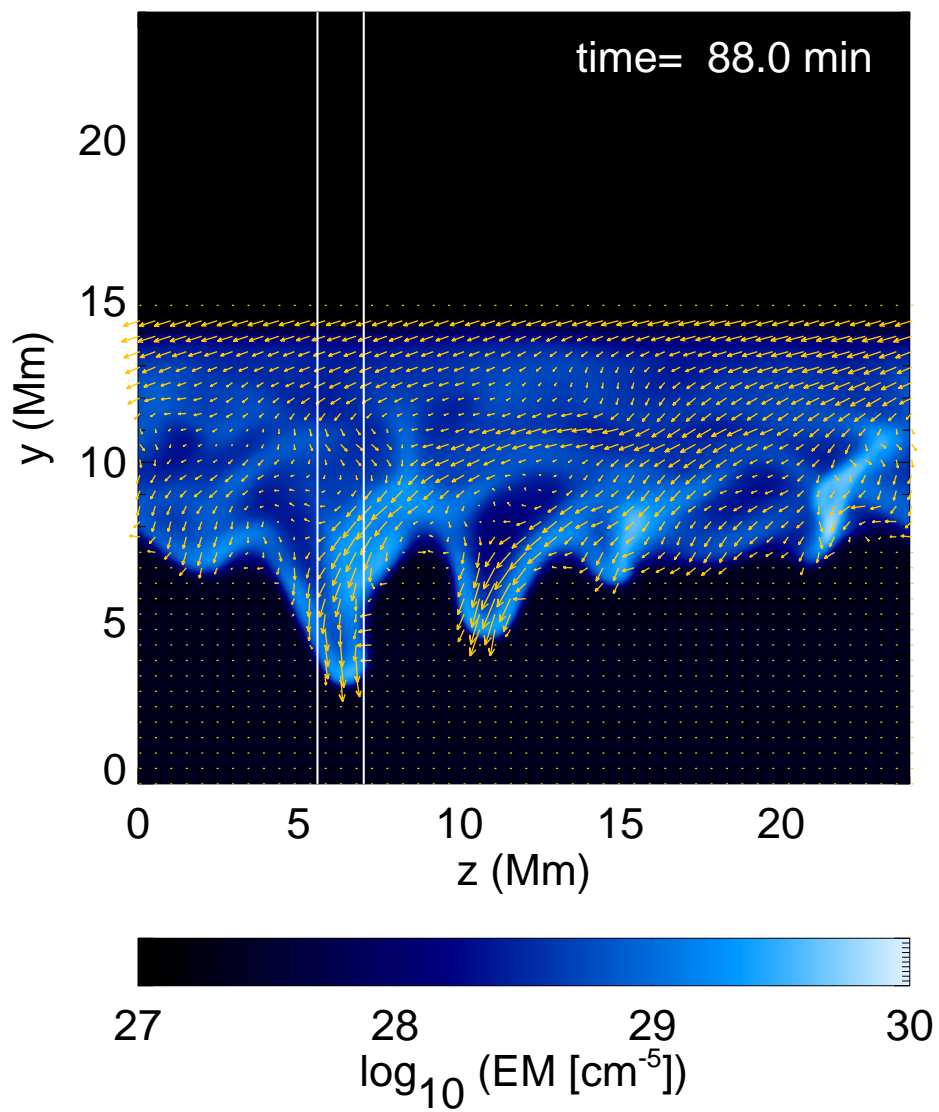


Figure 3.6: Flows inside prominence. Arrows represents velocities (V_y^p, V_z^p) defined as Eqs. (3.5) and (3.6).

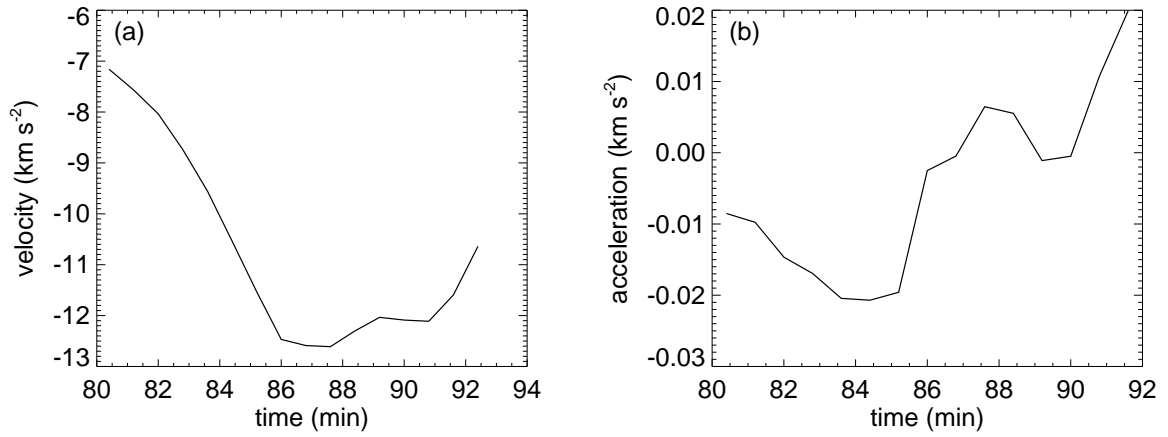


Figure 3.7: Panels (a) and (b) show maximum downward speed and acceleration of in the spike within dashed lines in Fig. 3.6 against time.

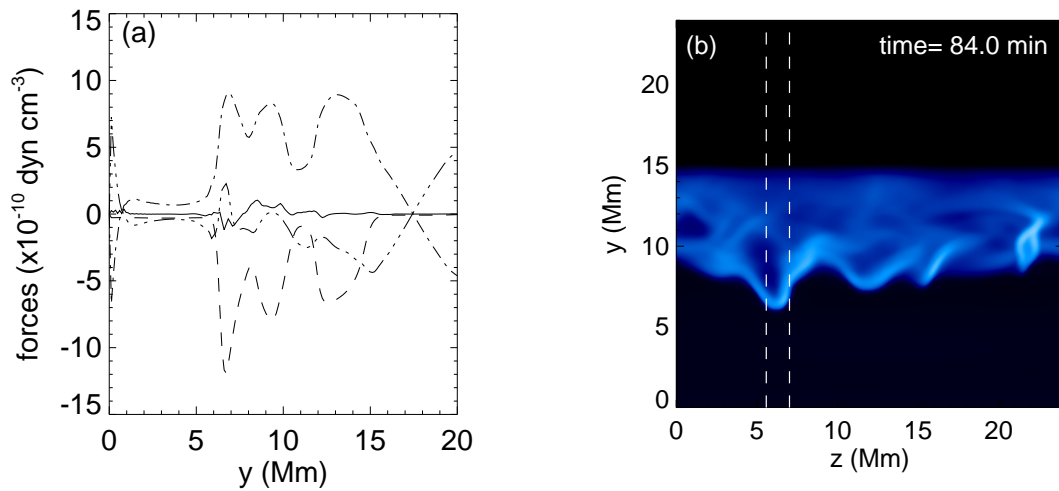


Figure 3.8: Vertical forces in a spike. In panel (a), solid line, dashed line, dash-dotted line, and dash-triple-dotted lines represent total force, gravity force, magnetic tension force, and pressure gradient force (sum of gas and magnetic pressure gradient), respectively. The forces at $x = 0$ in the area within two dashed lines in panel (b) are averaged.

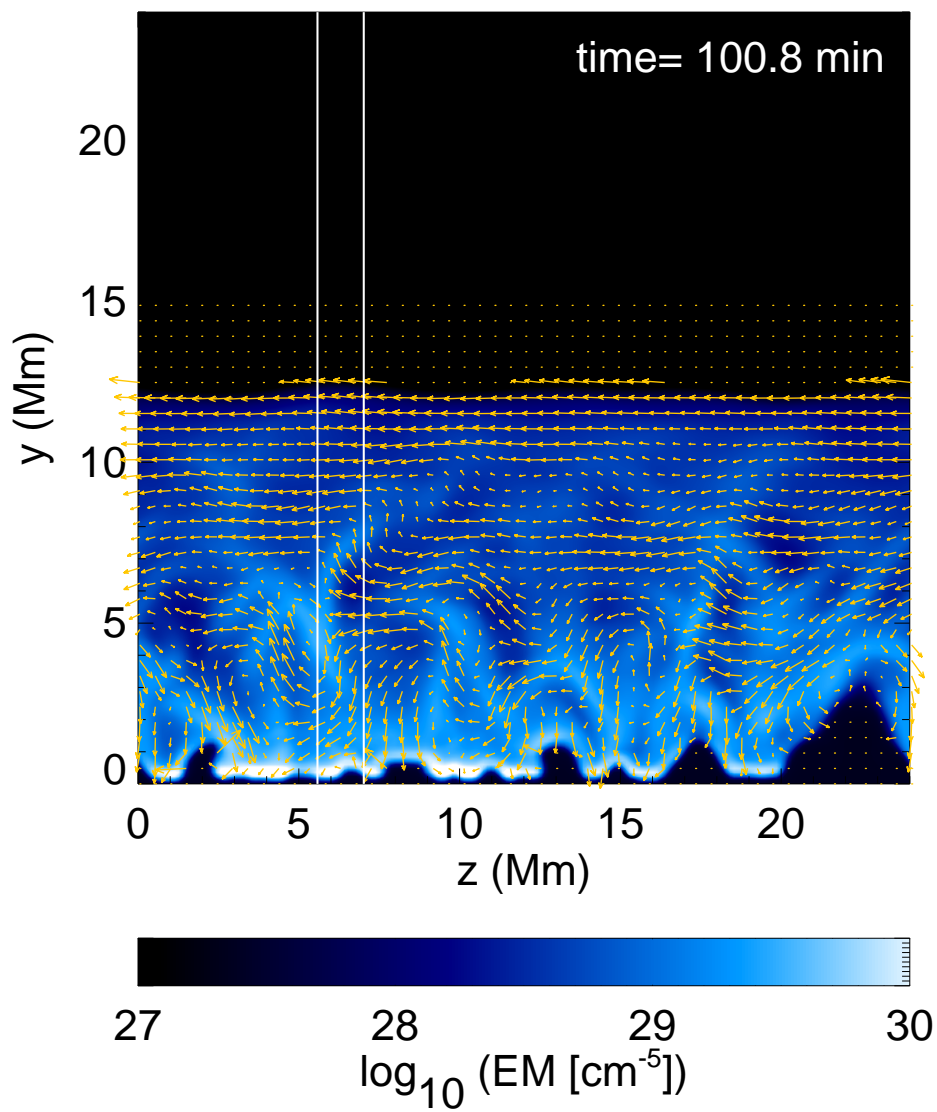


Figure 3.9: Flows inside prominence. Arrows represents velocities (V_y^p, V_z^p) defined as Eqs. (3.5) and (3.6).

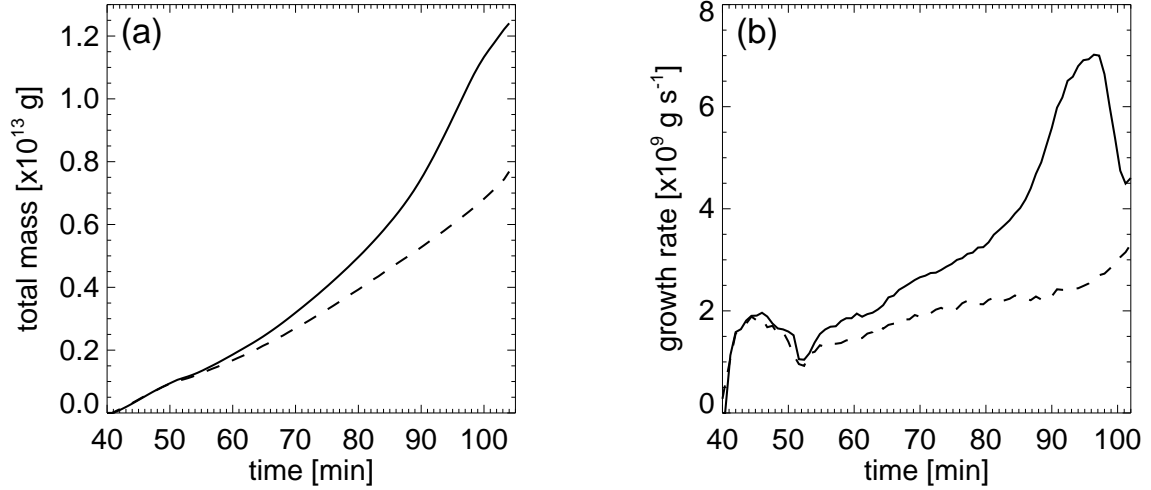


Figure 3.10: Panels (a) and (b) show total mass and mass growth rate of cool plasmas ($T < 10^5$ K) against time, respectively. Solid and dashed lines represent cases P1 and M1, respectively.

certain height y_c given as

$$\dot{M}_{\text{drain}}(y_c) = \int_{T < 10^5 \text{K}} \rho(x, y_c, z) v_y(x, y_c, z) dx dz, \quad (3.8)$$

where $y_c = 5$ Mm. The mass drainage rate is comparable and temporally correlated with condensation rate, which is consistent with observational results. Figure 3.12 shows time evolution of average density and volume. The volume in case P increases faster than that in case M1 after $t = 60$ min, whereas the time evolution of average density is not different between two cases until $t = 90$ min. This means that the rapid volume increase by extending spikes accelerates condensation rate. Our results give an insight of self mass maintenance mechanisms by the coupling of radiative condensation and the Rayleigh-Taylor instability.

Figure 3.13 shows the DEM averaged in y - and z -direction in our simulation. The DEM of our simulated prominence is consistent with the observational DEM, hence the

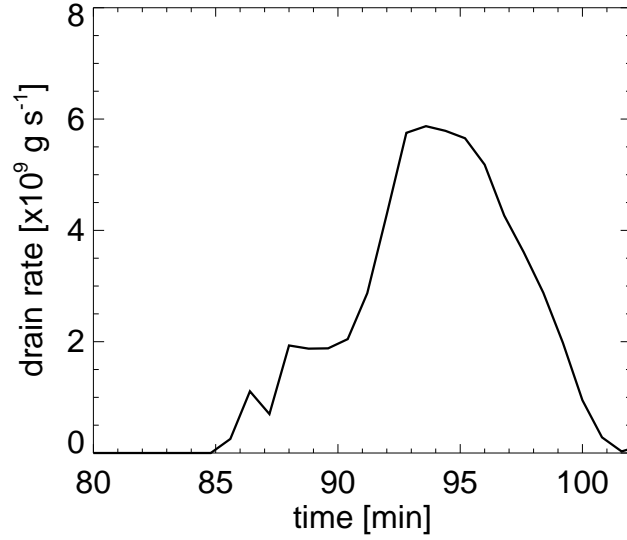


Figure 3.11: Mass drainage rate defined as Eq. (3.8).

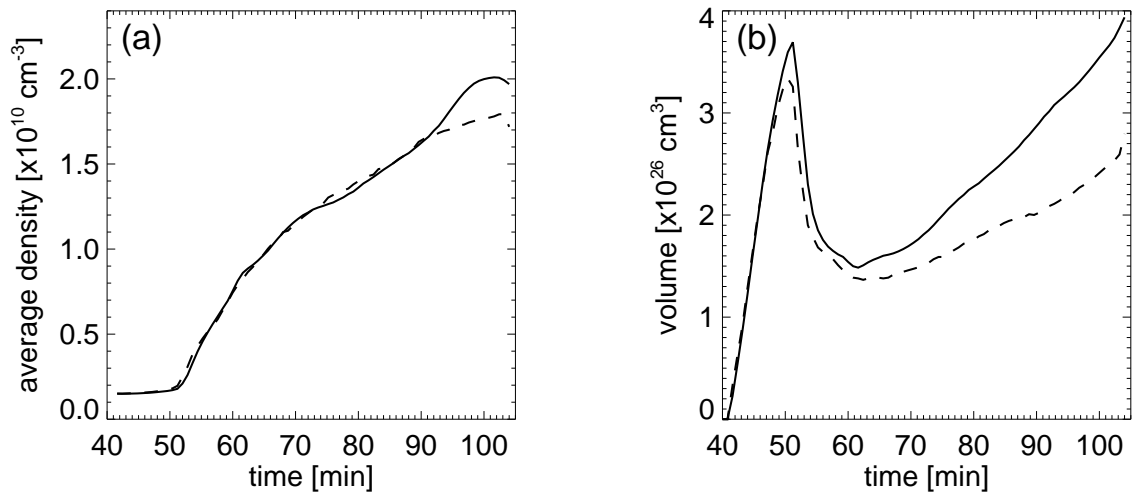


Figure 3.12: Panels (a) and (b) show average density and volume of cool plasmas ($T < 10^5$ K) against time, respectively. Solid and dashed line represents cases P1 and M1, respectively.

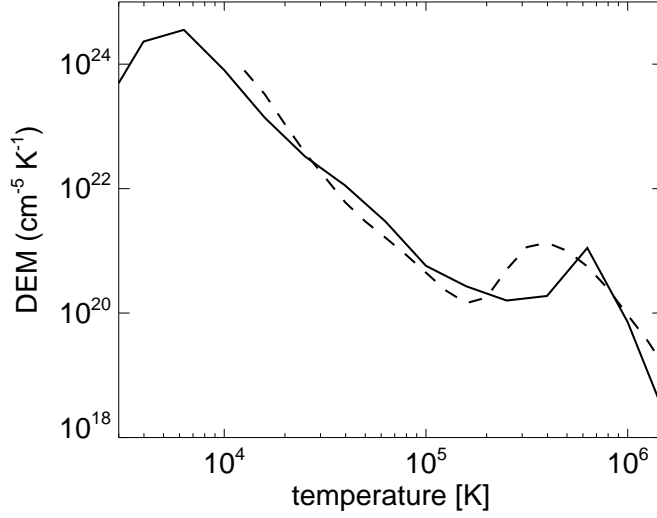


Figure 3.13: DEM obtained from our 3D simulation and observation. Solid and dashed line represents DEM from simulation in the present simulation and the observation by Wiik et al. (1993), respectively

mass distribution against temperature of our model is plausible.

3.4 Summary and Discussion

We reproduced vertical threads and flows by imposing the footpoint motion with random speed along a PIL in our reconnection-condensation model. As prominence mass increases, upward magnetic tension force can not sustain the gravity of prominence mass, leading to the Rayleigh-Taylor instability. As the spike extends, magnetic tension force increases and cancels the gravity force. As a result, the speed of downflows is much smaller than free-fall speed, and consistent with the typical downward speed in observations. The paths of spikes eventually become vertical threads in a prominence. We ensure that the vertical threads can be formed even in a flux rope. Our simulation result suggests that the

vertical threads do not represent vertical magnetic field, while supports the existence of horizontal magnetic fields. In our simulation results, it is found that condensation rate is enhanced by Rayleigh-Taylor instability. Moreover, mass drainage rate is comparable to the condensation rate. Our results suggest the self mass maintenance mechanism through the coupling of radiative condensation and Rayleigh-Taylor instability.

In our simulation, the thin vertical threads are formed after the spikes touch the bottom boundary where velocities are fixed to zero. The materials in spikes are reflected at the bottom boundary, and create upflows. The bottom boundary in our simulation is artificial, while the reflection of the spikes is a possible process if we regard the bottom boundary as the interface between the corona and the chromosphere. Numerical simulations of Rayleigh-Taylor instability of prominence including the chromosphere shows that materials in spikes are reflected at the top of the chromosphere, and returned back to the coronal height (Keppens et al., 2015).

We performed additional simulations with much smaller amplitudes of velocity fluctuations in the footpoint motion and confirmed that the Rayleigh-Taylor instability grow even in these cases. Recent observations with high spatial resolution and time cadence revealed that the corona and the chromosphere are full of wave perturbations (e.g. Tomczyk et al., 2007; Okamoto et al., 2007; De Pontieu et al., 2007). Prominences are likely to suffer from perturbations, hence, mass drainage by the Rayleigh-Taylor instability inevitably happens in quiescent prominences.

The observed dark plumes are not reproduced in our simulation. The upward buoyant force may not overcome the gravity force which is continuously increased during condensation. After touching the bottom boundary, no coronal region is left beneath the prominence in our simulation. In observations (Berger et al., 2011; Dudík et al., 2012), plumes are originated from a bubble beneath the prominence. The bubbles were specu-

lated to be emerging fluxes containing coronal temperature plasmas. It might be necessary to introduce an emerging bipole at the bottom boundary for reproducing dark plumes.

Recent studies reported the properties of turbulence in a quiescent prominence by analyzing observational data of intensity or velocities (Leonardis et al., 2012; Freed et al., 2016; Hillier et al., 2016). They found that a break of scaling exponent exists in power spectrum or structure function, and the break point was around 2000 km in spatial scale. Our simulation can not reproduce such a turbulent nature at this moment probably due to numerical viscosity. Higher resolution simulation may contribute to understand the change of turbulent nature of prominences at a certain scale.

Chapter 4

General Discussion

4.1 Summary of the results

In this thesis, we investigate the formation mechanism and interior dynamics of solar prominences by developing a new prominence formation model. The thesis consists of demonstration of reconnection-condensation model (Chapter 2) and modeling of interior dynamics of prominence (Chapter 3).

In Chapter 2, we propose a new prominence formation model (Fig. 4.1). In our model, reconnection at a PIL changes the topology of magnetic field, leading to the formation of a flux rope. The flux rope traps the dense plasmas inside it. Radiative cooling inside the flux rope is enhanced by the trapped dense plasmas, leading to a cooling-dominant thermal nonequilibrium state. The magnetic field lines become longer after reconnection. Once the length of magnetic field exceeds the Field length, thermal nonequilibrium inside the flux rope can not be compensated by thermal conduction, leading to radiative condensation. From the parameter survey on footpoint motions, we find that the anti-shearing motion, which reduces magnetic shear of an arcade field, causes radiative condensation, whereas the shearing motion, which increases magnetic shear, leads to eruption of a hot flux

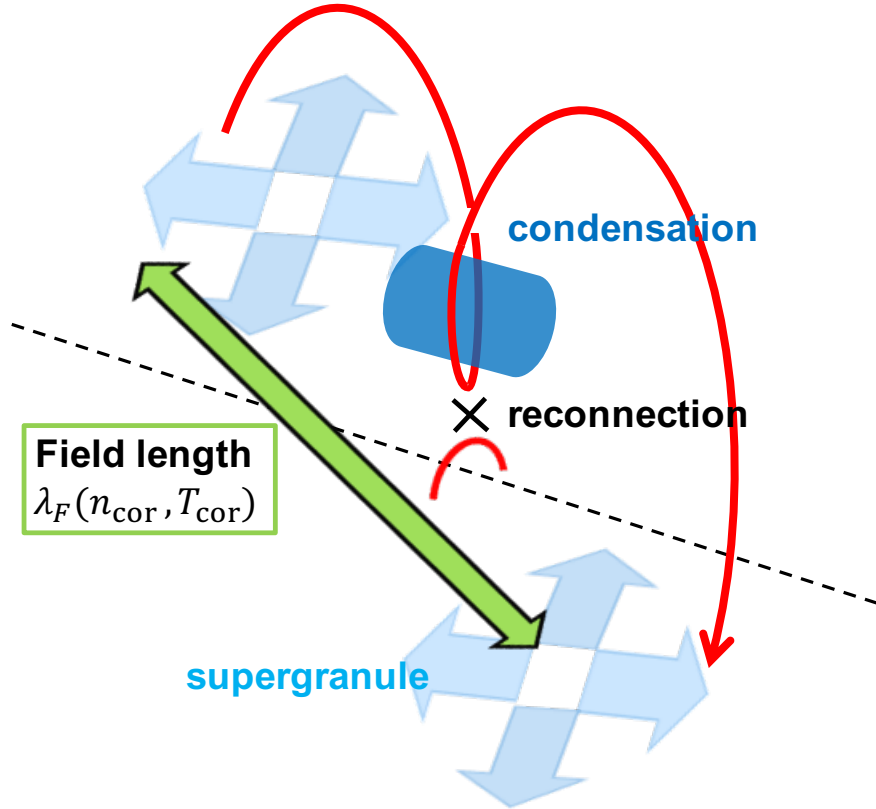


Figure 4.1: Summary of reconnection-condensation model.

rope. The direction of the motion parallel to the PIL can be determined by relative position of supergranules. By testing different types of heating models, we conclude that the background coronal heating model does not affect the triggering process of radiative condensation, whereas it can affect the properties of prominences.

In Chapter 3, we reproduce a dynamic interior of a prominence in the framework of our proposed model. The footpoint motion with random speed along the PIL gives a fluctuation of density in a flux rope. As mass increases by radiative condensation, upward magnetic tension can not sustain the gravity of prominence, leading to the Rayleigh-Taylor instability. Because upward magnetic tension force increases by extension of spikes and

cancels downward gravity force, the descending speeds of the spikes are much smaller than free-fall speed, and consistent with the observed descending speed. The reflection of the spikes at the bottom boundary creates upflows or vortex motions. By the interaction of the downflows and the reflected flows, the spikes are squeezed, resulting in formation of thin vertical threads. We ensure that the vertical threads can be formed even with horizontal magnetic field in a flux rope. We also found the Rayleigh-Taylor instability enhances the mass growth rate of radiative condensation. Our results suggest the presence of self mass maintenance mechanism of a prominence due to the coupling of radiative condensation and the Rayleigh Taylor instability.

4.2 Discussion

Our proposed model self-consistently explains in-situ condensation triggered by reconnection. Previous observational studies reported the prominence formation events associated with reconnection at PILs (Gaizauskas et al., 1997; Wang & Muglach, 2007; Yang et al., 2016), while the physical mechanism to trigger radiative condensation by reconnection was unclear. In-situ prominence formations were also found in observations (Berger et al., 2012; Liu et al., 2012). The model of Choe & Lee (1992) did not include reconnection. The model of Linker et al. (2001) included reconnection, while it was not in-situ condensation because chromospheric plasmas are directly injected in their model. In evaporation-condensation model, reconnection is only for a flux rope formation, and it is not directly related to radiative condensation (Xia & Keppens, 2016a). Our model self-consistently demonstrated that reconnection can be a trigger of in-situ radiative condensation.

Our model is appropriate to explain prominence formation at high altitudes. In observations, active region prominences are in lower altitudes (~ 10 Mm), while quiescent prominences are in higher altitudes (~ 100 Mm). In evaporation-condensation model,

radiative condensation can be triggered in a low-lying coronal arcade field because chromospheric evaporation driven by pressure gradient can inject relatively dense plasmas (the cooling source for radiative condensation) to the altitude comparable to the coronal scale height (60 Mm) at most. In our reconnection-condensation model, the formation height is not restricted by the coronal scale height, only dependent on the height of flux rope. The previous observational studies confirmed that inverse polarity prominences were likely to locate at higher altitudes, indicating the existence of flux ropes in high altitude (Leroy et al., 1983, 1984). Thus our model can explain prominence formations at higher altitudes than coronal scale height.

Future observational studies should check the length of reconnected magnetic field against the Field length. The cancellation or reconnection at a PIL was observed during the prominence formation (Gaizauskas et al., 1997; Wang & Muglach, 2007; Yang et al., 2016). The existence of reconnection-condensation process is promising. Typically, quiescent prominences are longer (~ 100 Mm) and active region prominences are shorter (~ 10 Mm). The difference of typical length between quiescent prominences and active region prominences may be explained by the Field length.

Our model can also be applied to a formation of polar crown prominences. Polar crown prominences are giant prominences (over 100 Mm in length and height) which surround the solar poles between $60^\circ - 70^\circ$ latitudes. Around the solar poles, remnant magnetic fluxes of decaying active regions come from lower latitudes and cancels the original magnetic fluxes, leading to magnetic polarity reversal with the period of 11 years (e.g. Shiota et al., 2012). During this process, reconnection events can happen between original magnetic fluxes around the poles and migrated magnetic fluxes. Our reconnection-condensation model can work in the site of magnetic reversal, resulting in formation of a polar crown prominence. Because polar crown prominences are extraordinary long, their magnetic

fields are likely to be longer than the Field length.

The significant mass drainage by downflows was found in a prominence (Liu et al., 2012). Condensation rate comparable to mass drainage rate is required to maintain a total prominence mass. We find that, in our model, condensation rate is enhanced by coupling with the Rayleigh-Taylor instability, and self-consistently becomes comparable to mass drainage rate. Our results suggest the self mass maintenance mechanism in a prominence. Xia & Keppens (2016a) also reproduced the mass maintenance mechanism in evaporation-condensation model by adopting a continuous mass supply of the chromospheric evaporation, while the presence of the Rayleigh-Taylor instability was unclear in their model. Future study must reveal the mass maintenance is driven by evaporation or self-induced by coupling of the Rayleigh-Taylor instability. Since bright cores of CMEs are composed of prominence plasmas, it is also important in solar-terrestrial physics.

Magnetic reconnection is usually regarded as a mechanism to heat up a system by releasing magnetic energy. We point out that magnetic reconnection can also lead to the catastrophic cooling and condensation if the system is potentially thermally unstable. In our study, thermal instability is triggered by redistribution of density and suppression of thermal conduction effect by a formation of a flux rope through reconnection. This process might be feasible in interstellar hot ionized medium. Magnetic reconnection driven by supernova shock in this region was studied by using resistive MHD simulations in Tanuma et al. (2001a,b). They suggested that magnetic reconnection is a possible heating mechanism in the interstellar medium to emit X-ray. The magnetic islands are formed by tearing mode instability inside a current sheet in their simulations. The magnetic island has closed geometry, hence, our reconnection-condensation mechanism can work depending on cooling and heating mechanism. Our reconnection-condensation model may explain phase transition from hot ionized medium to warm neutral medium in interstellar

space. Thus our model is applicable to the other astrophysical objects.

4.3 Future prospect

Understanding the mass circulation among the corona, prominences and the chromosphere is an important issue for discussing mass budget of prominences and coronal mass ejections (CMEs). This issue may also be related to the mechanism of recurrent prominence formation and homologous CMEs. Numerical modeling by Xia & Keppens (2016a) showed that the continuous mass supply by evaporation can sustain the mass cycle between the chromosphere and the corona through prominences, although such a steady strong evaporation has not been found in observations. Currently our model excludes the chromosphere, and the mass transport is only from the corona to prominence. In order to discuss the mass circulation, our model must be developed to include chromosphere.

The inclusion of self-consistent coronal heating is also one candidate for a future work. So far all prominence formation models including ours have assumed ad hoc coronal heating models to maintain an initial thermal equilibrium. In general, the coronal heating directly affect the mechanism of prominence formation and properties of prominence (Karpen et al., 2006; Karpen & Antiochos, 2008). The theory of prominence formation will be strongly improved by including self-consistent coronal heating. One way to reproduce self-consistent coronal heating is to introduce a wave input from the photosphere. The coronal heating by waves has been self-consistently modeled by recent numerical studies (Suzuki & Inutsuka, 2005; Matsumoto & Suzuki, 2012, 2014). In their model, waves propagating from the photosphere are dissipated in the corona by shock or phase-mixing, and heat up the corona to one million kelvin. They did not concern the influence of topological change of magnetic field on the coronal heating. Numerical simulation of reconnection-condensation model including self-consistent coronal heating will contribute

to understand both coronal heating mechanism and prominence formation.

Our prominence formation model is applicable to the modeling of prominence eruptions or coronal mass ejections. Some prominences disappear by mass drainage to the chromosphere, and other prominences disappear by sudden eruptions. The mechanism of prominence eruption is still unclear. In our proposed model, formation and eruption of a prominence can be explained in a unified manner in terms of the footpoint motion. In Section 2.3, we found that formation of a prominence is achieved in case of anti-shearing motion, while eruption occur in case of shearing. Coupling with mechanical instabilities is also possible. These include instability models such as kink and torus instability (Kliem et al., 2004; Török & Kliem, 2005; Kliem & Török, 2006; Fan & Gibson, 2007). The kink instability is likely triggered because the anti-shearing motion increase the twist of the flux rope. The torus instability also fit because the reduction of shear can alleviate the critical height of torus instability. The other model that fit with our mechanism is the reversed shear model of Kusano et al. (2004). We stopped the anti-shearing motion before the shear reversal. If we continued to impose the anti-shearing motion, the flux rope formation, condensation, and eruption would have successively occurred. Eruptions of quiescent prominences or polar crown prominences are important factor to affect the the solar-terrestrial plasma environment as well as flares in sunspots. Compared to sunspot regions, these eruptions occur in a region of weak magnetic field ($3 - 10$ G). In such a region, the gravity of prominence is comparable to Lorentz force, hence, prominence mass should be included to account for the mechanism of eruptions. Our study has succeeded to model a prominence with realistic density profiles and a plausible magnetic configuration. The next issue is how the prominence erupt. In our simulation, the prominence did not erupt, rather descended by gravity as radiative condensation proceeds. Further numerical study must consider how such a weak magnetic forces can erupt heavy promi-

nence materials. It is crucial issue for not only solar physics but also space weather and solar-terrestrial physics.

Chapter 5

Concluding remarks

Solar prominences are cool dense plasma clouds in the hot tenuous corona. Since prominences suddenly erupt and evolve into CMEs, they have potential to give an impact on the plasma environment in the interplanetary space. The origin of cool dense plasma and mass maintenance mechanism of prominences are still unclear. In this thesis, we investigate the formation mechanism of a prominence by using magnetohydrodynamic simulations.

Through the studies in this thesis, we succeeded to propose a self-consistent model for a long-standing issue of solar prominence formation. Our model resolves several issues in the previous models: a previous theoretical model requires a strong steady footpoint heating and subsequent chromospheric evaporation to trigger radiative condensation, while such a footpoint heating and evaporated flows have not been detected in observations. In observations, it was found that magnetic reconnection at a PIL caused prominence formations, while the mechanism to trigger radiative condensation by reconnection was unclear. In addition to these, we revealed that a flux rope formation by reconnection drives radiative condensation when the length of reconnected loops exceeds the Field length. We found that anti-shearing motion is necessary to create cooling-dominant thermal imbalance in

a flux rope. This suggests that relative position of supergranules along a PIL is an important factor for prominence formation. We also found that radiative condensation rate is enhanced by coupling with the Rayleigh-Taylor instability and becomes comparable to the mass drainage rate of downflows. This result indicates the presence of self mass maintenance mechanism of a prominence.

Appendix A

Numerical implementation for footpoint motion

Footpoint motions are introduced in the region below $y = 0$ by 5 grids. The velocity field is given as Eqs. (2.7) - (2.11), Eq. (2.26), or Eq. (3.1). To calculate advection of magnetic fluxes by the given velocities, the induction equation is solved numerically. The scheme is 4-stage Runge-Kutta method (Vögler et al., 2005) and 4th-order central finite difference method with artificial viscosity (Rempel, 2014). Free boundary condition is applied to magnetic fields at the bottom boundary. In every sub-step of the Runge-Kutta method, the artificial diffusive flux introduced by Rempel (2014) is applied to the magnetic fields as follows,

$$f_{i+1/2} = -\frac{1}{2}c_{i+1/2}\Phi_{i+1/2}(u_r - u_l) \quad (\text{A.1})$$

$$u_r = u_{i+1} - 0.5\Delta u_{i+1} \quad (\text{A.2})$$

$$u_l = u_i + 0.5\Delta u_i \quad (\text{A.3})$$

$$\Delta u_i = \text{minmod} [(u_{i+1} - u_{i-1})/2, 2(u_{i+1} - u_i), 2(u_i - u_{i-1})], \quad (\text{A.4})$$

$$c_{i+1/2} = \sqrt{v_{i+1/2}^2 + C_{s,i+1/2}^2 + C_{A,i+1/2}^2}, \quad (\text{A.5})$$

where notation of $i + 1/2$ denotes values at cell interfaces, and v , C_s and, C_A represent footpoint speed, sound speed and, Alfvén speed, respectively. $\Phi_{i+1/2}$ is given in regions with $(u_r - u_l) \cdot (u_{i+1} - u_i) > 0$ as

$$\Phi_{i+1/2} = \max \left[0, 1 + h \left(\frac{u_r - u_l}{u_{i+1} - u_i} - 1 \right) \right] \quad (\text{A.6})$$

where $h = 2$, and $\Phi_{i+1/2} = 0$ in regions with $(u_r - u_l) \cdot (u_{i+1} - u_i) \leq 0$.

The pressure and density below $y = 0$ by 5 grids are determined by

$$p_j = \frac{2H_{\text{cor}} + \Delta y}{2H_{\text{cor}} - \Delta y} p_{j+1}, \quad (\text{A.7})$$

$$\rho_j = \frac{m}{k_B T_{\text{cor}}} p_j, \quad (\text{A.8})$$

where j represents grid number in y -direction, Δy is grid spacing size, $H_{\text{cor}} = k_B T_{\text{cor}} / (m g_{\text{cor}})$ is coronal scale height, and $T_{\text{cor}} = 1$ MK is constant coronal temperature. Equations (A.7) and (A.8) correspond to the equation of hydrostatic equilibrium as

$$\frac{p_{j+1} - p_j}{\Delta y} = -\rho_{j+1/2} g_{\text{cor}}, \quad (\text{A.9})$$

where

$$\rho_{j+1/2} = \frac{\rho_{j+1} + \rho_j}{2}. \quad (\text{A.10})$$

References

- Amari, T., Luciani, J. F., Mikic, Z., & Linker, J. 2000, *ApJ*, 529, L49
- Antiochos, S. K., & Klimchuk, J. A. 1991, *ApJ*, 378, 372
- Antiochos, S. K., MacNeice, P. J., Spicer, D. S., & Klimchuk, J. A. 1999, *ApJ*, 512, 985
- Aschwanden, M. J., Nightingale, R. W., & Alexander, D. 2000, *ApJ*, 541, 1059
- Aulanier, G., Démoulin, P., Mein, N., et al. 1999, *A&A*, 342, 867
- Aulanier, G., Demoulin, P., van Driel-Gesztelyi, L., Mein, P., & Deforest, C. 1998a, *A&A*, 335, 309
- . 1998b, *A&A*, 335, 309
- Berger, T. 2012, in *Astronomical Society of the Pacific Conference Series*, Vol. 463, Second ATST-EAST Meeting: Magnetic Fields from the Photosphere to the Corona., 147
- Berger, T., Testa, P., Hillier, A., et al. 2011, *Nature*, 472, 197
- Berger, T. E., Liu, W., & Low, B. C. 2012, *ApJ*, 758, L37
- Berger, T. E., Shine, R. A., Slater, G. L., et al. 2008, *ApJ*, 676, L89
- Berger, T. E., Slater, G., Hurlburt, N., et al. 2010, *ApJ*, 716, 1288

- Bobra, M. G., van Ballegooijen, A. A., & DeLuca, E. E. 2008, *ApJ*, 672, 1209
- Boerner, P., Edwards, C., Lemen, J., et al. 2012, *Sol. Phys.*, 275, 41
- Bommier, V., Landi Degl’Innocenti, E., Leroy, J.-L., & Sahal-Brechot, S. 1994, *Sol. Phys.*, 154, 231
- Casini, R., López Ariste, A., Tomczyk, S., & Lites, B. W. 2003, *ApJ*, 598, L67
- Chae, J. 2003, *ApJ*, 584, 1084
- . 2010, *ApJ*, 714, 618
- Chae, J., Ahn, K., Lim, E.-K., Choe, G. S., & Sakurai, T. 2008, *ApJ*, 689, L73
- Choe, G. S., & Lee, L. C. 1992, *Sol. Phys.*, 138, 291
- Cirigliano, D., Vial, J.-C., & Rovira, M. 2004, *Sol. Phys.*, 223, 95
- De Pontieu, B., McIntosh, S. W., Carlsson, M., et al. 2007, *Science*, 318, 1574
- Díaz, A. J., Khomenko, E., & Collados, M. 2014, *A&A*, 564, A97
- Dudík, J., Aulanier, G., Schmieder, B., Zapiór, M., & Heinzel, P. 2012, *ApJ*, 761, 9
- Engvold, O. 1976, *Sol. Phys.*, 49, 283
- . 1981, *Sol. Phys.*, 70, 315
- Fan, Y. 2001, *ApJ*, 554, L111
- Fan, Y., & Gibson, S. E. 2007, *ApJ*, 668, 1232
- Field, G. B. 1965, *ApJ*, 142, 531
- Freed, M. S., McKenzie, D. E., Longcope, D. W., & Wilburn, M. 2016, *ApJ*, 818, 57

- Fuller, J., & Gibson, S. E. 2009, *ApJ*, 700, 1205
- Fuller, J., Gibson, S. E., de Toma, G., & Fan, Y. 2008, *ApJ*, 678, 515
- Gaizauskas, V., Zirker, J. B., Sweetland, C., & Kovacs, A. 1997, *ApJ*, 479, 448
- Gibson, S. E., Kucera, T. A., Rastawicki, D., et al. 2010, *ApJ*, 724, 1133
- Gopalswamy, N., Shimojo, M., Lu, W., et al. 2003, *ApJ*, 586, 562
- Gunár, S., Parenti, S., Anzer, U., Heinzl, P., & Vial, J.-C. 2011, *A&A*, 535, A122
- Habbal, S. R., Druckmüller, M., Morgan, H., et al. 2010, *ApJ*, 719, 1362
- Habbal, S. R., Morgan, H., & Druckmüller, M. 2014, *ApJ*, 793, 119
- Hildner, E. 1974, *Sol. Phys.*, 35, 123
- Hillier, A., Berger, T., Isobe, H., & Shibata, K. 2012a, *ApJ*, 746, 120
- Hillier, A., Isobe, H., Shibata, K., & Berger, T. 2011, *ApJ*, 736, L1
- . 2012b, *ApJ*, 756, 110
- Hillier, A., Matsumoto, T., & Ichimoto, K. 2016, *ArXiv e-prints* 1610.08281
- Karpen, J. T., & Antiochos, S. K. 2008, *ApJ*, 676, 658
- Karpen, J. T., Antiochos, S. K., Hohensee, M., Klimchuk, J. A., & MacNeice, P. J. 2001, *ApJ*, 553, L85
- Karpen, J. T., Antiochos, S. K., & Klimchuk, J. A. 2006, *ApJ*, 637, 531
- Karpen, J. T., Antiochos, S. K., Klimchuk, J. A., & MacNeice, P. J. 2003, *ApJ*, 593, 1187
- Karpen, J. T., Tanner, S. E. M., Antiochos, S. K., & DeVore, C. R. 2005, *ApJ*, 635, 1319

- Keppens, R., & Xia, C. 2014, *ApJ*, 789, 22
- Keppens, R., Xia, C., & Porth, O. 2015, *ApJ*, 806, L13
- Khomenko, E., Díaz, A., de Vicente, A., Collados, M., & Luna, M. 2014, *A&A*, 565, A45
- Kippenhahn, R., & Schlüter, A. 1957, *ZAp*, 43, 36
- Kliem, B., Titov, V. S., & Török, T. 2004, *A&A*, 413, L23
- Kliem, B., & Török, T. 2006, *Physical Review Letters*, 96, 255002
- Kuckein, C., Centeno, R., Martínez Pillet, V., et al. 2009, *A&A*, 501, 1113
- Kuperus, M., & Raadu, M. A. 1974, *A&A*, 31, 189
- Kusano, K., Maeshiro, T., Yokoyama, T., & Sakurai, T. 2004, *ApJ*, 610, 537
- Labrosse, N., Heinzel, P., Vial, J.-C., et al. 2010, *Space Sci. Rev.*, 151, 243
- Leonardis, E., Chapman, S. C., & Foullon, C. 2012, *ApJ*, 745, 185
- Leroy, J. L., Bommier, V., & Sahal-Brechot, S. 1983, *Sol. Phys.*, 83, 135
- . 1984, *A&A*, 131, 33
- Lin, Y., Engvold, O., Rouppe van der Voort, L., Wiik, J. E., & Berger, T. E. 2005, *Sol. Phys.*, 226, 239
- Linker, J. A., Lionello, R., Mikić, Z., & Amari, T. 2001, *J. Geophys. Res.*, 106, 25165
- Lites, B. W., Kubo, M., Berger, T., et al. 2010, *ApJ*, 718, 474
- Liu, W., Berger, T. E., & Low, B. C. 2012, *ApJ*, 745, L21

- López Ariste, A., & Aulanier, G. 2007, in *Astronomical Society of the Pacific Conference Series*, Vol. 368, *The Physics of Chromospheric Plasmas*, ed. P. Heinzel, I. Dorotovič, & R. J. Rutten, Heinzel
- Luna, M., Karpen, J. T., & DeVore, C. R. 2012, *ApJ*, 746, 30
- Mackay, D. H., Gaizauskas, V., & Yeates, A. R. 2008, *Sol. Phys.*, 248, 51
- Mackay, D. H., Karpen, J. T., Ballester, J. L., Schmieder, B., & Aulanier, G. 2010, *Space Sci. Rev.*, 151, 333
- Magara, T. 2006, *ApJ*, 653, 1499
- Manchester, IV, W., Gombosi, T., DeZeeuw, D., & Fan, Y. 2004, *ApJ*, 610, 588
- Mandrini, C. H., Démoulin, P., & Klimchuk, J. A. 2000, *ApJ*, 530, 999
- Martens, P. C., & Zwaan, C. 2001, *ApJ*, 558, 872
- Martin, S. F. 1998a, *Sol. Phys.*, 182, 107
- Martin, S. F. 1998b, in *Astronomical Society of the Pacific Conference Series*, Vol. 150, *IAU Colloq. 167: New Perspectives on Solar Prominences*, ed. D. F. Webb, B. Schmieder, & D. M. Rust, 419
- Matsumoto, T., & Suzuki, T. K. 2012, *ApJ*, 749, 8
- . 2014, *MNRAS*, 440, 971
- Meyer, C. D., Balsara, D. S., & Aslam, T. D. 2012, *MNRAS*, 422, 2102
- Meyer, C. D., Balsara, D. S., & Aslam, T. D. 2014, *Journal of Computational Physics*, 257, 594

- Mok, Y., Drake, J. F., Schnack, D. D., & van Hoven, G. 1990, *ApJ*, 359, 228
- Okamoto, T. J., Tsuneta, S., Berger, T. E., et al. 2007, *Science*, 318, 1577
- Okamoto, T. J., Tsuneta, S., Lites, B. W., et al. 2008, *ApJ*, 673, L215
- Orozco Suárez, D., Asensio Ramos, A., & Trujillo Bueno, J. 2014, *A&A*, 566, A46
- Paletou, F., López Ariste, A., Bommier, V., & Semel, M. 2001, *A&A*, 375, L39
- Parenti, S., Schmieder, B., Heinzl, P., & Golub, L. 2012, *ApJ*, 754, 66
- Parenti, S., & Vial, J.-C. 2007, *A&A*, 469, 1109
- Parker, E. N. 1953, *ApJ*, 117, 431
- Poland, A. I., & Mariska, J. T. 1986, *Sol. Phys.*, 104, 303
- Priest, E. R. 1998, in *Astronomical Society of the Pacific Conference Series*, Vol. 150, IAU Colloq. 167: *New Perspectives on Solar Prominences*, ed. D. F. Webb, B. Schmieder, & D. M. Rust, 453
- Priest, E. R., Foley, C. R., Heyvaerts, J., et al. 2000, *ApJ*, 539, 1002
- Rempel, M. 2014, *ApJ*, 789, 132
- Rondi, S., Roudier, T., Molodij, G., et al. 2007, *A&A*, 467, 1289
- Ryutova, M., Berger, T., Frank, Z., Tarbell, T., & Title, A. 2010, *Sol. Phys.*, 267, 75
- Saito, K., & Hyder, C. L. 1968, *Sol. Phys.*, 5, 61
- Saito, K., & Tandberg-Hanssen, E. 1973, *Sol. Phys.*, 31, 105
- Schmelz, J. T., Reames, D. V., von Steiger, R., & Basu, S. 2012, *ApJ*, 755, 33

- Schmieder, B., Kucera, T. A., Knizhnik, K., et al. 2013, *ApJ*, 777, 108
- Schmieder, B., Roudier, T., Mein, N., et al. 2014, *A&A*, 564, A104
- Schmit, D. J., & Gibson, S. 2013, *ApJ*, 770, 35
- Schmit, D. J., Gibson, S., Luna, M., Karpen, J., & Innes, D. 2013, *ApJ*, 779, 156
- Shiota, D., Tsuneta, S., Shimojo, M., et al. 2012, *ApJ*, 753, 157
- Spitzer, L. 1962, *Physics of Fully Ionized Gases*
- Su, Y., & van Ballegoijen, A. 2012, *ApJ*, 757, 168
- Suzuki, T. K., & Inutsuka, S.-i. 2005, *ApJ*, 632, L49
- Tanuma, S., Yokoyama, T., Kudoh, T., & Shibata, K. 2001a, *Journal of Korean Astronomical Society*, 34, 309
- . 2001b, *ApJ*, 551, 312
- Terradas, J., Soler, R., Luna, M., et al. 2016, *ApJ*, 820, 125
- Tomczyk, S., McIntosh, S. W., Keil, S. L., et al. 2007, *Science*, 317, 1192
- Török, T., & Kliem, B. 2005, *ApJ*, 630, L97
- van Ballegoijen, A. A. 2004, *ApJ*, 612, 519
- van Ballegoijen, A. A., & Martens, P. C. H. 1989, *ApJ*, 343, 971
- Vögler, A., Shelyag, S., Schüssler, M., et al. 2005, *A&A*, 429, 335
- Wang, Y.-M., & Muglach, K. 2007, *ApJ*, 666, 1284
- Welsch, B. T., DeVore, C. R., & Antiochos, S. K. 2005, *ApJ*, 634, 1395

- Wiik, J. E., Dere, K., & Schmieder, B. 1993, *A&A*, 273, 267
- Xia, C., Chen, P. F., & Keppens, R. 2012, *ApJ*, 748, L26
- Xia, C., Chen, P. F., Keppens, R., & van Marle, A. J. 2011, *ApJ*, 737, 27
- Xia, C., & Keppens, R. 2016a, *ApJ*, 823, 22
- . 2016b, *ApJ*, 825, L29
- Xia, C., Keppens, R., Antolin, P., & Porth, O. 2014a, *ApJ*, 792, L38
- Xia, C., Keppens, R., & Guo, Y. 2014b, *ApJ*, 780, 130
- Yang, B., Jiang, Y., Yang, J., Yu, S., & Xu, Z. 2016, *ApJ*, 816, 41
- Yokoyama, T., & Shibata, K. 1994, *ApJ*, 436, L197
- Zirker, J. B., Engvold, O., & Martin, S. F. 1998, *Nature*, 396, 440
- Zirker, J. B., Engvold, O., & Yi, Z. 1994, *Sol. Phys.*, 150, 81